

AN ACCELERATED AERODYNAMIC OPTIMIZATION APPROACH FOR A
SMALL TURBOJET ENGINE CENTRIFUGAL COMPRESSOR

A THESIS SUBMITTED TO
THE GRADUATE SCHOOL OF NATURAL AND APPLIED SCIENCES
OF
MIDDLE EAST TECHNICAL UNIVERSITY

BY

ARDA CEYLANOĞLU

IN PARTIAL FULLFILLMENT OF THE REQUIREMENTS
FOR
THE DEGREE OF MASTER OF SCIENCE
IN
MECHANICAL ENGINEERING

DECEMBER 2009

Approval of the thesis:

**AN ACCELERATED AERODYNAMIC OPTIMIZATION APPROACH FOR
A SMALL TURBOJET ENGINE CENTRIFUGAL COMPRESSOR**

submitted by **ARDA CEYLANOĞLU** in partial fulfilment of the requirements for
the degree of **Master of Science in Mechanical Engineering Department, Middle
East Technical University** by,

Prof. Dr. Canan Özgen
Dean, Graduate School of **Natural and Applied Sciences**

Prof. Dr. Süha Oral
Head of Department, **Mechanical Engineering**

Assoc. Prof. Dr. Abdullah Ulaş
Supervisor, **Mechanical Engineering Dept., METU**

Dr. Mehmet Ali Ak
Co-Supervisor, **TÜBİTAK-SAGE**

Examining Committee Members:

Prof. Dr. Hafit Yüncü
Mechanical Engineering Dept., METU

Assoc. Prof. Dr. Abdullah Ulaş
Mechanical Engineering Dept., METU

Dr. Mehmet Ali Ak
TÜBİTAK-SAGE

Prof. Dr. Hüseyin Vural
Mechanical Engineering Dept., METU

Prof. Dr. Yusuf Özyörük
Aerospace Engineering Dept., METU

Date: 11.12.2009

I hereby declare that all information in this document has been obtained and presented in accordance with academic rules and ethical conduct. I also declare that, as required by these rules and conduct, I have fully cited and referenced all material and results that are not original to this work.

Name, Last name : Arda CEYLANOĞLU

Signature :

ABSTRACT

AN ACCELERATED AERODYNAMIC OPTIMIZATION APPROACH FOR A SMALL TURBOJET ENGINE CENTRIFUGAL COMPRESSOR

Ceylanoğlu, Arda

M.S., Department of Mechanical Engineering

Supervisor : Assoc. Prof. Dr. Abdullah ULAŞ

Co-Supervisor: Dr. Mehmet Ali AK

December 2009, 146 pages

Centrifugal compressors are widely used in propulsion technology. As an important part of turbo-engines, centrifugal compressors increase the pressure of the air and let the pressurized air flow into the combustion chamber. The developed pressure and the flow characteristics mainly affect the thrust generated by the engine.

The design of centrifugal compressors is a challenging and time consuming process including several tests, computational fluid dynamics (CFD) analyses and optimization studies. In this study, a methodology on the geometry optimization and CFD analyses of the centrifugal compressor of an existing small turbojet engine are introduced as increased pressure ratio being the objective. The purpose is to optimize the impeller geometry of a centrifugal compressor such that the pressure ratio at the maximum speed of the engine is maximized. The methodology introduced provides a guidance on the geometry optimization of centrifugal impellers supported with CFD analysis outputs.

The original geometry of the centrifugal compressor is obtained by means of optical scanning. Then, the parametric model of the 3-D geometry is created by using a CAD software. A design of experiments (DOE) procedure is applied through geometrical parameters in order to decrease the computation effort and guide through the optimization process. All the designs gathered through DOE study are modelled in the CAD software and meshed for CFD analyses. CFD analyses are carried out to investigate the resulting pressure ratio and flow characteristics.

The results of the CFD studies are used within the Artificial Neural Network methodology to create a fit between geometric parameters (inputs) and the pressure ratio (output). Then, the resulting fit is used in the optimization study and a centrifugal compressor with higher pressure ratio is obtained by following a single objective optimization process supported by design of experiments methodology.

Keywords: Centrifugal Compressor, Design of Experiments, Optimization, Computational Fluid Dynamics (CFD), Reverse Engineering

ÖZ

KÜÇÜK TURBOJET MOTORU SANTRİFÜJ KOMPRESÖRÜ İÇİN HIZLANDIRILMIŞ AERODİNAMİK OPTİMİZASYON YAKLAŞIMI

Ceylanoğlu, Arda

Yüksek Lisans, Makina Mühendisliği Bölümü

Tez Yöneticisi : Doç. Dr. Abdullah ULAŞ

Ortak Tez Yöneticisi : Dr. Mehmet Ali AK

Aralık 2009, 146 sayfa

Santrifüj kompresörler itki sistemlerinde yaygın olarak kullanılmaktadır. Motora giren havanın basıncını artırarak ve basınçlı havanın yanma odasına ulaşmasını sağlayarak, turbo-motorlarda önemli bir rol oynamaktadır. Ortaya çıkan basınç ve akış karakteristiği motor tarafından üretilen itki üzerinde önemli etki yapmaktadır.

Santrifüj kompresör tasarımı bir çok testi, sayısal akışkanlar dinamiği analizlerini ve optimizasyon çalışmalarını kapsayan uzun soluklu bir prosestir. Bu çalışmada, varolan küçük bir turbojet motoruna ait santrifüj kompresörün basınç oranını artırmaya yönelik geometri optimizasyonu ve sayısal analizlerine ait yöntemler üzerinde durulmuştur. Turbojet motorunun maksimum açısız hızında ortaya çıkan basınç oranının maksimize edilmesi ve böylece bu koşulda elde edilen itkinin artırılması amaçlanmaktadır. Yapılan çalışma ile sayısal akışkanlar dinamiği destekli geometri optimizasyonu üzerine bir yöntem sunulmuştur.

İlk olarak eldeki turbojet motorunun orjinal kompresör geometrisi optik tarama metodu ile elde edilmiştir. Elde edilen modelin bir CAD yazılımı aracılığıyla üç boyutlu parametrik modeli hazırlanmıştır. Oluşturulan parametre (değişken) listesi kullanılarak, sayısal analiz sayısını azaltmak, dolayısıyla analiz süresini kısaltmak ve optimizasyon çalışmasına yol göstermesi amacıyla deney tasarımı metodu kullanılmıştır. Deney tasarımı sonucunda oluşan tasarımların önce üç boyutlu modeli oluşturulmuş ve oluşturulan modelde CFD analizlerinde kullanılmak üzere ağ yapısı kurulmuştur. Tüm modeller için CFD analizleri yapılmış ve kompresör basınç katsayıları ve akış karakteristikleri incelenmiştir.

Çalışmanın girdileri olan geometri değişkenleri ile CFD çalışmalarında elde edilen çıktılar arasındaki ilişki yapay sinir ağı yöntemi kullanılarak oluşturulmuş ve bu çalışma sonucunda, deney tasarımı metodu ile desteklenmiş bir optimizasyon çalışması ile daha yüksek basınç katsayısına sahip yeni bir santrifüj kompresör geometrisi elde edilmiştir.

Anahtar Kelimeler: Santrifüj Kompresör, Deney Tasarımı, Optimizasyon, Sayısal Akışkanlar Dinamiği, Tersine Mühendislik

To my parents, with love & respect...

ACKNOWLEDGEMENTS

I would like to express my gratitude to all people who provided me the chance of completing this thesis. My special thanks and appreciation goes to my supervisor Assoc. Prof. Dr. Abdullah ULAŞ and co-supervisor Dr. Mehmet Ali AK for their guidance, criticism, encouragements and insight throughout the research.

Also, I want to thank my colleagues Kenan BOZKAYA and Mehmet Sinan HASANOĞLU for their indisputable support throughout my thesis. Many thanks to Bora YAZICI, who has helped me through challenging CFD studies.

TÜBİTAK-SAGE, who suggested this thesis work and provided necessary support, is also acknowledged.

Finally, I would like to express my great love to my family who never give up encouraging me not only during this thesis study but also through my life. Their valuable support and determination is greatly acknowledged.

TABLE OF CONTENTS

ABSTRACT	iv
ÖZ	vi
ACKNOWLEDGEMENTS	ix
TABLE OF CONTENTS	x
LIST OF TABLES	xii
LIST OF FIGURES	xiii
LIST OF SYMBOLS	xviii
CHAPTERS	
1. INTRODUCTION.....	1
1.1 General	1
1.2 Objectives of the Thesis	5
1.3 Outline of the Thesis	7
2. LITERATURE SURVEY	9
2.1 Reverse Engineering	9
2.2 Geometric Modeling	12
2.2.1 General Definitions	12
2.2.2 Impeller Geometry Generation	15
2.2.2.1 Meridional Channel.....	16
2.2.2.2 Blade Angle Definition	18
2.2.2.3 Camber Line Generation	19
2.2.2.4 Camber Surface Generation	22
2.3 Computational Fluid Dynamics	23
2.3.1 General	23
2.3.2 Application to Turbomachinery	26
2.4 Design of Experiments & Optimization.....	30

2.4.1	Design of Experiments (DOE)	34
2.4.1.1	Orthogonal Arrays	35
2.4.1.2	Face Centered Cubic Design	36
2.4.1.3	I-optimal and D-optimal Designs	37
2.4.2	Response Surface Method	38
2.4.3	Artificial Neural-Network Method	40
3.	COMPRESSOR GEOMETRY MODEL	42
3.1	Engine Disassembly	42
3.2	Optical Scanning	44
3.3	Geometry Generation	48
3.4	Parameters and Dimensions	51
4.	PARAMETERIZATION & DESIGN OF EXPERIMENTS METHODOLOGY	56
4.1	Design Parameters	56
4.2	Design of Experiments	59
5.	COMPUTATIONAL FLUID DYNAMICS ANALYSES	64
5.1	CFD Analysis Assumptions	65
5.2	CFD Solutions	68
6.	ARTIFICIAL NEURAL NETWORK FIT & OPTIMIZATION	76
6.1	Artificial Neural Network	76
7.	CONCLUSION and FUTURE WORK	84
7.1	General	84
7.2	Discussion and Recommendations for Future Work	86
	REFERENCES	88
	APPENDIX A	93
	APPENDIX B	99

LIST OF TABLES

Table 1 Important Terms & Definitions.....	14
Table 2 Parameters and Values	54
Table 3 Bezier Control Point Coordinates (mm)	54
Table 4 Continuous Parameters List	58
Table 5 Grid Convergence	73
Table 6 Iterative Neural Network Studies.....	83
 Table A.1 I-optimal Design Space	 93

LIST OF FIGURES

Figure 1 Shapes of Centrifugal Impeller Blades [3].	3
Figure 2 Pressure Ratio (Head) vs Mass Flow Rate for Three Blade Shapes.....	3
Figure 3 General Centrifugal Compressor Performance Diagram [2]	4
Figure 4 Flowchart of the Thesis Study	6
Figure 5 Traditional vs. Reverse Engineering Process [8].....	10
Figure 6 Entities of an Impeller	13
Figure 7 Coordinates, Meridional Section and the Camber.....	13
Figure 8 Meridional Channel	17
Figure 9 Blade Angle vs. m' [20]	19
Figure 10 Ruled Surface by Two Curves.....	23
Figure 11 Ruled Surface by Straight Line Elements [24]	23
Figure 12 Flow Surfaces S1 and S2 for a Centrifugal Impeller [2]	27
Figure 13 Genetic Algorithm with Artificial Neural Network (ANN) [21]	33
Figure 14 Orthogonal vs. Non-Orthogonal Design Space [36]	36
Figure 15 Face Centered Cubic Design	37
Figure 16 Artificial Neurons [42]	40
Figure 17 Disassembly Sequence.....	43
Figure 18 Disassembly of the Engine	44
Figure 19 optoTOP-HE 3-D Optical Scanner	45
Figure 20 Working Principle of an Optical Scanner [26]	45
Figure 21 Original Compressor Geometry.....	47
Figure 22 Optic Scanner Output	47
Figure 23 Hub & Shroud Curve Formation	48
Figure 24 Splitter, Main Blade Camber Surfaces and Meridional Section.....	49
Figure 25 3-D Model of the Impellers and the Shroud Casing.....	50
Figure 26 Impeller-Diffuser Assembly (Casing removed)	51
Figure 27 Bezier Control Points for Original Geometry Meridional Section.....	52
Figure 28 Constraints on Meridional Section	56

Figure 29 Design Space for H2Z, H3R and S2Z	62
Figure 30 Design Space for β_{ih} , β_{is} , β_{eh}	62
Figure 31 Design Space for S1R, S3R and N	63
Figure 32 Coarse Grid with 10,000 Elements.....	70
Figure 33 Fine Grid with 600,000 Elements.....	70
Figure 34 Total Pressure Distribution (in Pa) (10,000 elements)	72
Figure 35 Total Pressure Distribution (in Pa) (600,000 elements)	72
Figure 36 Total Pressure Distribution (in Pa) for Case #4.....	74
Figure 37 Total Pressure Distribution (in Pa) for Case #6.....	75
Figure 38 Sample Neural Network with 3 Hidden Nodes	77
Figure 39 Triangular Simplex	79
Figure 40 Neural Network Structure with 4 Hidden Nodes.....	80
Figure 41 Actual Pressure Ratio vs Predicted Pressure Ratio.....	80
Figure 42 Optimum Geometry Pressure Distribution (in Pa) (10,000 elements)	81
Figure 43 Optimum Geometry Pressure Distribution (in Pa) (600,000 elements) ...	82
Figure B.1 Total Pressure Distribution (in Pa) for Original Case, PR=3.68.....	99
Figure B.2 Total Pressure Distribution (in Pa) for Case #1, PR=3.32.....	100
Figure B.3 Total Pressure Distribution (in Pa) for Case #2, PR=2.86.....	100
Figure B.4 Total Pressure Distribution (in Pa) for Case #3, PR=3.69.....	101
Figure B.5 Total Pressure Distribution (in Pa) for Case #4, PR=4.16.....	101
Figure B.6 Total Pressure Distribution (in Pa) for Case #5, PR=3.46.....	102
Figure B.7 Total Pressure Distribution (in Pa) for Case #6, Choked.....	102
Figure B.8 Total Pressure Distribution (in Pa) for Case #7, Choked.....	103
Figure B.9 Total Pressure Distribution (in Pa) for Case #8, PR=2.83.....	103
Figure B.10 Total Pressure Distribution (in Pa) for Case #9, PR=3.35.....	104
Figure B.11 Total Pressure Distribution (in Pa) for Case #10, PR=3.39.....	104
Figure B.12 Total Pressure Distribution (in Pa) for Case #11, PR=2.69.....	105
Figure B.13 Total Pressure Distribution (in Pa) for Case #12, PR=2.89.....	105
Figure B.14 Total Pressure Distribution (in Pa) for Case #13, PR=2.01	106
Figure B.15 Total Pressure Distribution (in Pa) for Case #14, PR=3.22	106

Figure B.16 Total Pressure Distribution (in Pa) for Case #15, PR=3.68	107
Figure B.17 Total Pressure Distribution (in Pa) for Case #16, PR=2.24	107
Figure B.18 Total Pressure Distribution (in Pa) for Case #17, PR=3.84	108
Figure B.19 Total Pressure Distribution (in Pa) for Case #18, PR=2.91	108
Figure B.20 Total Pressure Distribution (in Pa) for Case #19, PR=2.22	109
Figure B.21 Total Pressure Distribution (in Pa) for Case #20, PR=2.80	109
Figure B.22 Total Pressure Distribution (in Pa) for Case #21, PR=3.94	110
Figure B.23 Total Pressure Distribution (in Pa) for Case #22, PR=3.18	110
Figure B.24 Total Pressure Distribution (in Pa) for Case #23, PR=2.78	111
Figure B.25 Total Pressure Distribution (in Pa) for Case #24, PR=3.02	111
Figure B.26 Total Pressure Distribution (in Pa) for Case #25, PR=2.71	112
Figure B.27 Total Pressure Distribution (in Pa) for Case #26, PR=3.07	112
Figure B.28 Total Pressure Distribution (in Pa) for Case #27, PR=2.39	113
Figure B.29 Total Pressure Distribution (in Pa) for Case #28, PR=3.19	113
Figure B.30 Total Pressure Distribution (in Pa) for Case #29, PR=2.75	114
Figure B.31 Total Pressure Distribution (in Pa) for Case #30, PR=1.95	114
Figure B.32 Total Pressure Distribution (in Pa) for Case #31, Choked.....	115
Figure B.33 Total Pressure Distribution (in Pa) for Case #32, PR=3.34	115
Figure B.34 Total Pressure Distribution (in Pa) for Case #33, PR=3.65	116
Figure B.35 Total Pressure Distribution (in Pa) for Case #34, PR=3.48	116
Figure B.36 Total Pressure Distribution (in Pa) for Case #35, PR=3.54	117
Figure B.37 Total Pressure Distribution (in Pa) for Case #36, PR=2.87	117
Figure B.38 Total Pressure Distribution (in Pa) for Case #37, PR=3.26	118
Figure B.39 Total Pressure Distribution (in Pa) for Case #38, PR=3.71	118
Figure B.40 Total Pressure Distribution (in Pa) for Case #39, PR=2.85	119
Figure B.41 Total Pressure Distribution (in Pa) for Case #40, PR=2.95	119
Figure B.42 Total Pressure Distribution (in Pa) for Case #41, PR=3.04	120
Figure B.43 Total Pressure Distribution (in Pa) for Case #42, Choked.....	120
Figure B.44 Total Pressure Distribution (in Pa) for Case #43, Choked.....	121
Figure B.45 Total Pressure Distribution (in Pa) for Case #44, PR=3.57	121
Figure B.46 Total Pressure Distribution (in Pa) for Case #45, PR=3.66	122

Figure B.47 Total Pressure Distribution (in Pa) for Case #46, PR=3.41	122
Figure B.48 Total Pressure Distribution (in Pa) for Case #47, PR=1.92	123
Figure B.49 Total Pressure Distribution (in Pa) for Case #48, PR=3.19	123
Figure B.50 Total Pressure Distribution (in Pa) for Case #49, PR=3.57	124
Figure B.51 Total Pressure Distribution (in Pa) for Case #50, PR=3.24	124
Figure B.52 Total Pressure Distribution (in Pa) for Case #51, PR=3.54	125
Figure B.53 Total Pressure Distribution (in Pa) for Case #52, PR=2.48	125
Figure B.54 Total Pressure Distribution (in Pa) for Case #53, PR=3.24	126
Figure B.55 Total Pressure Distribution (in Pa) for Case #54, PR=3.11	126
Figure B.56 Total Pressure Distribution (in Pa) for Case #55, PR=2.67	127
Figure B.57 Total Pressure Distribution (in Pa) for Case #56, PR=3.86	127
Figure B.58 Total Pressure Distribution (in Pa) for Case #57, PR=3.59	128
Figure B.59 Total Pressure Distribution (in Pa) for Case #58, PR=3.40	128
Figure B.60 Total Pressure Distribution (in Pa) for Case #59, PR=2.37	129
Figure B.61 Total Pressure Distribution (in Pa) for Case #60, PR=3.79	129
Figure B.62 Total Pressure Distribution (in Pa) for Case #61, PR=3.46	130
Figure B.63 Total Pressure Distribution (in Pa) for Case #62, Choked	130
Figure B.64 Total Pressure Distribution (in Pa) for Case #63, PR=2.18	131
Figure B.65 Total Pressure Distribution (in Pa) for Case #64, PR=3.68	131
Figure B.66 Total Pressure Distribution (in Pa) for Case #65, PR=3.36	132
Figure B.67 Total Pressure Distribution (in Pa) for Case #66, PR=2.86	132
Figure B.68 Total Pressure Distribution (in Pa) for Case #67, PR=2.70	133
Figure B.69 Total Pressure Distribution (in Pa) for Case #68, PR=2.23	133
Figure B.70 Total Pressure Distribution (in Pa) for Case #69, Choked	134
Figure B.71 Total Pressure Distribution (in Pa) for Case #70, PR=3.67	134
Figure B.72 Total Pressure Distribution (in Pa) for Case #71, PR=3.06	135
Figure B.73 Total Pressure Distribution (in Pa) for Case #72, PR=3.91	135
Figure B.74 Total Pressure Distribution (in Pa) for Case #73, PR=3.59	136
Figure B.75 Total Pressure Distribution (in Pa) for Case #74, PR=2.41	136
Figure B.76 Total Pressure Distribution (in Pa) for Case #75, PR=3.41	137
Figure B.77 Total Pressure Distribution (in Pa) for Case #76, PR=2.82	137

Figure B.78 Total Pressure Distribution (in Pa) for Case #77, PR=2.40	138
Figure B.79 Total Pressure Distribution (in Pa) for Case #78, PR=3.82	138
Figure B.80 Total Pressure Distribution (in Pa) for Case #79, PR=3.51	139
Figure B.81 Total Pressure Distribution (in Pa) for Case #80, PR=3.28	139
Figure B.82 Total Pressure Distribution (in Pa) for Case #81, Choked.....	140
Figure B.83 Total Pressure Distribution (in Pa) for Iteration #1, PR=3.56	140
Figure B.84 Total Pressure Distribution (in Pa) for Iteration #2, PR=3.90	141
Figure B.85 Total Pressure Distribution (in Pa) for Iteration #3, PR=4.05	141
Figure B.86 Total Pressure Distribution (in Pa) for Iteration #4, PR=4.10	142
Figure B.87 Total Pressure Distribution (in Pa) for Iteration #5, PR=2.99	142
Figure B.88 Total Pressure Distribution (in Pa) for Iteration #6, PR=4.12	143
Figure B.89 Total Pressure Distribution (in Pa) for Iteration #7, PR=3.24	143
Figure B.90 Total Pressure Distribution (in Pa) for Iteration #8, PR=4.20	144
Figure B.91 Total Pressure Distribution (in Pa) for Iteration #9, PR=3.99	144
Figure B.92 Total Pressure Distribution (in Pa) for Iteration #10, PR=4.18	145
Figure B.93 Total Pressure Distribution (in Pa) for Iteration #11, PR=4.18	145
Figure B.94 Total Pressure Distribution (in Pa) for Optimum Case, PR=4.21	146

LIST OF SYMBOLS

COR	:	Cut-off ratio at the hub
N	:	Number of blades
P	:	Bezier control point
PR	:	Pressure ratio
T	:	Temperature
\vec{f}_c	:	Centrifugal force per unit mass
\vec{f}_{cor}	:	Coriolis force per unit mass
\vec{f}_e	:	External forces per unit mass
\vec{v}	:	Velocity vector
\vec{w}	:	Velocity relative to the rotating system
$\vec{\omega}$:	Angular velocity
c_p	:	Specific heat for constant pressure
h	:	Enthalpy
m	:	Meridional length
m'	:	Radius normalized meridional length
\dot{m}	:	Mass flow rate
n	:	Degree of Bezier curve
p	:	Pressure
t	:	Blade thickness
u,v	:	Non-dimensional Bezier parameters

r, θ, z	:	Cylindrical coordinates
β	:	Blade angle
δr	:	Infinitesimal radial distance
δz	:	Infinitesimal axial distance
θ	:	Theta angle
μ	:	Dynamic viscosity coefficient
γ	:	Specific heat ratio
ρ	:	Density

Subscripts

cl	:	Camber line
eh	:	Hub side exit
es	:	Shroud side exit
h	:	Hub
ih	:	Hub side inlet
is	:	Shroud side inlet
s	:	Shroud
ts	:	Total to static
tt	:	Total to total
$h1,2,3,4z$:	z-coordinates of hub side control points
$h1,2,3,4r$:	r-coordinates of hub side control points
$s1,2,3,4z$:	z-coordinates of shroud side control points
$s1,2,3,4r$:	r-coordinates of shroud side control points

CHAPTER 1

INTRODUCTION

1.1 General

Centrifugal compressors are widely used in industrial applications where highly pressurized gas is needed. They are especially used in gas turbine industry, while examples are seen in process plants, too. The small turbojet engines and the turbochargers are the most common examples. Among all examples, the small gas turbines have experienced a growing interest lately. Their large energy capacity with respect to their total weight makes them attractive for use in small propulsion vehicles like model airplanes, UAVs and missiles.

Axial and centrifugal compressors are the most common members of rotary turbomachines. Centrifugal compressors provide higher pressure ratios than axial compressors. The pressure ratio generated by a centrifugal compressor ranges from 1 to 1.3 per stage for process industries, 3 to 7 for small gas turbines and mostly 13 for the experimental models [1]. For a desired pressure increase, fewer stages can be used with respect to axial compressors. Moreover, the operating speed of the centrifugal compressors are higher than other types of compressors. The geometry of the impellers of a centrifugal compressor is simpler with respect to axial compressor impellers. Therefore, manufacturing costs of a centrifugal compressor is much lower than an axial compressor. For compact systems which require low cost, low stages, large operating ranges and high pressure ratios, centrifugal compressors provide the best choice. For bigger designs, axial compressors can be used which have higher efficiency and higher mass flow rates.

A centrifugal compressor of a gas turbine mainly composes of impellers (blades), diffuser and a volute or collecting chamber that surrounds the impellers and the diffuser. Usually splitters can be separated between the impellers in order to decrease the blockage at impeller inlet.

The impeller is the most important part of a centrifugal compressor. The fluid flow is forced through the impeller by rotating impeller blades. Work is continuously transferred to the flow as it passes through the impellers. One of the functions of the impeller is to create low pressure at the inlet such that the fluid flow can easily proceed through the entrance of the impeller [2]. The air enters the impeller in axial direction and exits in a radial direction into a diffuser. As the flow is bent through the impellers, complex forces start to occur on the fluid flow like centrifugal and Coriolis forces which can create complicated flow fields throughout the flow volume. Due to complex flow fields and force distributions, the impeller design is still a very challenging process.

Splitter blades are another important part of impellers. They are some forms of main blades which are used to decrease the flow blockage at the inlet of the impeller. Splitters mostly use main blade's angular and thickness definition and they are formed by cutting the main blade at a specified fraction of its meridional length at hub and shroud sides. Splitters are placed circumferentially between the main blades and they have been used for decades in compressors and improved overall performance in terms of efficiency and pressure ratio. Splitters reduce the load on the main blades and may introduce additional losses that depend upon their geometry [44].

The blades of a centrifugal compressor is categorized according to the exit angle formation. These are backward-curved or back-swept blades, radial blades and

forward-curved or forward-swept blades. The three types of the blades and the corresponding velocity triangles are shown in Figure 1.

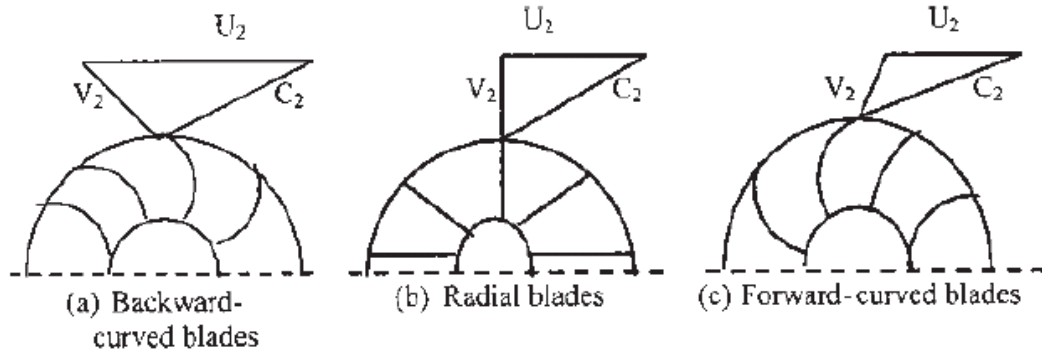


Figure 1 Shapes of Centrifugal Impeller Blades [3].

According to Bloch [4], the head or pressure do not vary with load (mass flow rate) for radial blades. If the backward-curved blade is used, the head or pressure decreases with increasing load. For forward-curved blades, the head or pressure increases with increasing load as shown in Figure 2. Bloch [4] also states that forward-curved blades are not practical on compressors. They are rather chosen for blowers or fans.

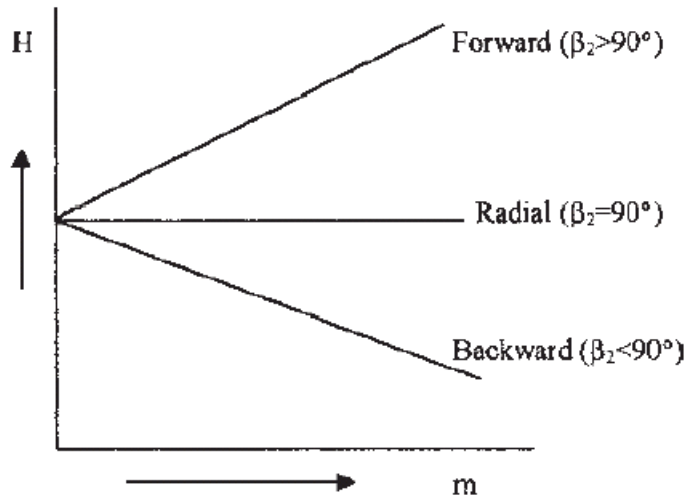


Figure 2 Pressure Ratio (Head) vs Mass Flow Rate for Three Blade Shapes

The 30% or 40% of the energy leaving the impeller is the kinetic energy [2]. Therefore, this energy should be converted into static pressure rise in the diffuser. There are two types of diffusers: vaneless and vaned diffusers. Vaneless diffuser is in fact a free space without vanes which extends up to the discharge of the compressor or it can be a free space between the impeller tip and the beginning of a vaned diffuser. Vaneless diffusers provide large ranges with low costs. Vaned diffusers are selected for higher efficiencies. Vaned diffusers are categorized as cascade and channel diffusers. Cascade diffusers have airfoil shaped vanes, while channel diffusers have vaned slots which forces to flow into linear motion along the path of the diffuser. Vaned diffusers are more common with respect to vaneless diffusers.

The general performance of a centrifugal compressor can be summarized as in Figure 3. For a fixed mass flow rate, if the pressure ratio is desired to be increased, then the efficiency falls.

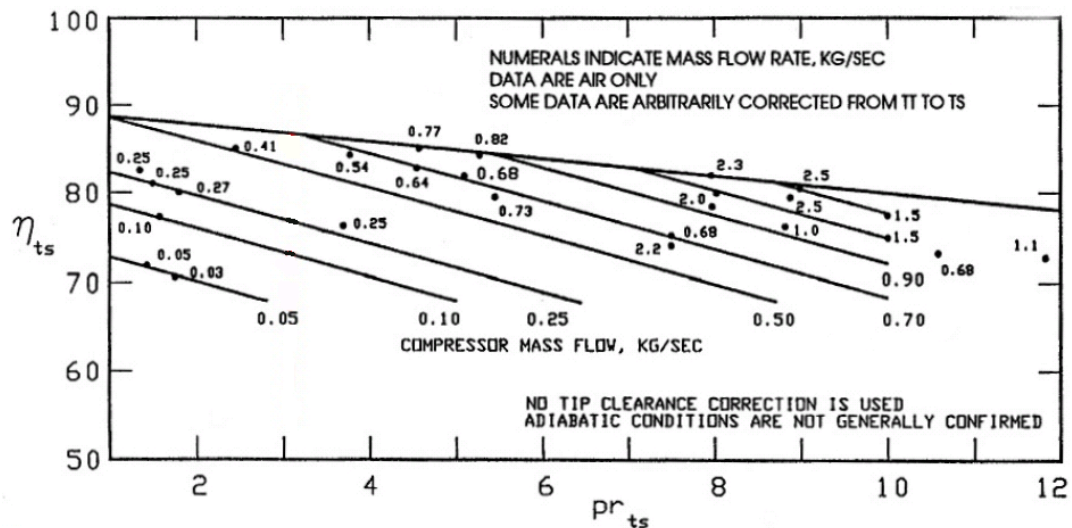


Figure 3 General Centrifugal Compressor Performance Diagram [2]

The thermal efficiency of an ideal gas turbine is related to the pressure ratio and it can be simply estimated by the following equation [5]:

$$\eta_{th} = 1 - \frac{1}{(P_2/P_1)^{(k-1)/k}} \quad (1.1)$$

For small engines, the thermal efficiency is very low and ranges between 10 and 20% [6].

1.2 Objectives of the Thesis

The geometric modelling, optimization and computational fluid dynamics (CFD) analysis of a centrifugal compressor are challenging processes. Since the geometric optimization process is based on many parameters to be examined, huge computational effort and time are needed for overall optimization process.

In this study, the geometry of an existing centrifugal compressor of a small turbojet engine is to be optimized on pressure ratio. Therefore, firstly the original geometry is analyzed, then the parametrically modelled geometry is run into an optimization process. The impeller side is modelled parametrically for flexible handling through the optimization process. The flowchart of the thesis study is given in Figure 4.

The main objectives of this study can be summarized as:

- Disassembling the turbojet engine and obtaining the CAD of the centrifugal compressor by means of point cloud acquired by a 3-D optical scanning method according to reverse engineering requirements.

- Parametric geometry modelling of a centrifugal compressor with splitters such that a flexible manipulation of the geometry is obtained for the computational analysis.
- Definition of parameters, constraints and objectives for the optimization studies and computational fluid dynamics analyses.
- Pursuing a design of experiments (DOE) methodology to analyse the single or combined effects of parameters, elimination of non-effective or less effective parameters and therefore reducing the computational effort.
- Meshing of the centrifugal compressor including the impellers and the diffuser and solving the geometry with FLUENT solver according to some boundary conditions.
- Evaluating the results of CFD analyses in an optimization code which is guided by the DOE methodology and reaching the desired optimum geometry.

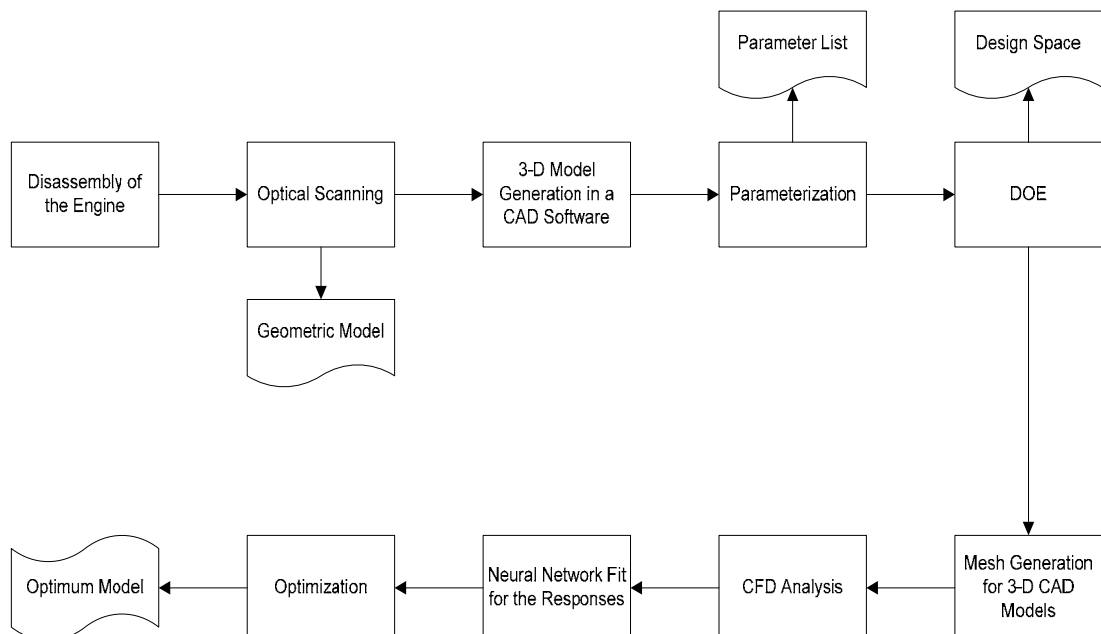


Figure 4 Flowchart of the Thesis Study

1.3 Outline of the Thesis

This chapter provides a brief introduction to centrifugal compressors including the definition of main parts, working principle and performance characteristics. After describing the objectives of the study, this chapter is followed by Chapter 2 in which a detailed literature survey is presented. In Chapter 2, literature survey on any study that this thesis covers is provided. It covers the literature work and some definitions, equations and explanations needed for studies and analyses to be done. Therefore, the methodology and its detailed explanation is provided and supported with similar studies in literature. Reverse engineering methodology, geometric modelling, CFD studies, design of experiments and optimization methodology are the main titles explained in literature survey.

Chapter 3 includes the studies carried out for obtaining the 3-D geometric model of the original centrifugal compressor. The reverse engineering methodology (disassembly and 3-D optical scanning) to gather the compressor geometry is provided and the main parameters of a centrifugal impeller needed for parametric 3-D modelling are presented. Then, the parameter values of the original geometry is tabulated.

Chapter 4 covers the design of experiment and parameterization studies which guide the optimization process. In this chapter, study on the evaluation of parameters in order to reduce computational effort and required time is presented. The geometric parameters and their intervals of interest within the optimization study are defined. The design space is generated which guides the parameter variation along the analysis. The combination of parameters are provided which are used in CFD analyses in a sequence. The methodology to reach and estimate the optimum point is presented.

Chapter 5 includes the computational fluid dynamics (CFD) analyses for the original compressor geometry and sample analyses for other different geometries. Mesh generation of the flow field in the impeller and diffuser is presented. Boundary conditions and solver options are explained in this chapter.

Chapter 6 covers the neural network fit and optimization studies. In this chapter, the relation between the input parameters and the output (pressure ratio) is obtained by using artificial neural network methodology. Then, an optimization algorithm is applied on the fit to find the optimum configuration.

Chapter 7 includes the conclusion remarks and future works to be done.

CHAPTER 2

LITERATURE SURVEY

This chapter presents the results of a deep literature survey on similar studies which create an important theoretical background through the thesis work. Beside similar studies, completely different cases are also researched in order to offer a solution to some parts of the thesis study. Furthermore, a comprehensive survey on past studies is presented and their relation to this thesis work is explained.

The thesis study is divided into sub-sections and the literature survey on each section is presented separately.

2.1 Reverse Engineering

Engineering covers two branches, forward and reverse engineering. Forward engineering is the traditional approach in which a design process is performed from the requirements stage up to physical implementation of a product. On the contrary, reverse engineering is the analysis and processing of technical specifications of an existing system. Reverse engineering is also described as the process of obtaining a geometric CAD model from 3-D points acquired by scanning and digitizing of existing parts [7]. Briefly, reverse engineering is taking apart an object to see how it works for duplication or enhancement purposes. A general comparison of two methods is summarized in Figure 5.

Some important reasons for using reverse engineering can be listed as [7]:

- Gathering required technical information about a part which has unknown geometrical and performance specifications,
- Inspection and quality control,
- Manufacturing of a part for which there are no CAD data,
- Exploring new avenues to improve product performance.

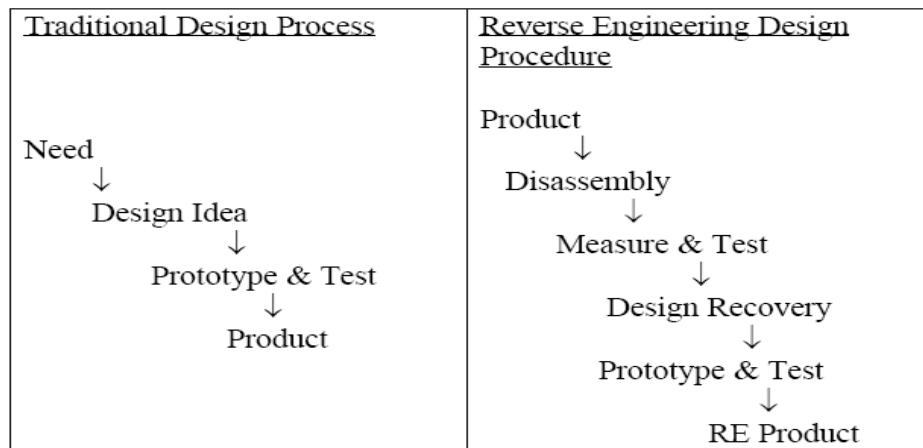


Figure 5 Traditional vs. Reverse Engineering Process [8].

The methodology to be chosen on gathering the required CAD data depends on the reason of reverse engineering a part, number of parts to be examined, size of the part, complexity of the shape, part material and surface finish (shiny or not) and expected accuracy. According to these parameters, the researcher chooses between contact or non-contact type of scanners [7].

Contact scanners mainly have probes which automatically follows the contours of the part to be examined. CMM (Coordinate Measuring Machine) is the most common example for contact type scanners. The abilities of a CMM are restricted with its degree of freedom and the probe's characteristics.

Laser and optic scanners are non-contact type of scanners which have better abilities with respect to CMM especially for complex geometries. Unless the part is shaded, these scanners provide perfect results.

The CAD of a centrifugal impeller can be obtained via either CMM or optic 3-D scanners. Depending on the complexity of the impeller shape, both of the techniques can be chosen. Chen et al. [9] describes how the impeller geometry of a centrifugal compressor can be obtained by using a CMM machine. Several points on the hub and shroud camber lines are measured by means of a CMM probe and the measured coordinates are used in a CAD software for post processing. The accuracy of the reconstructed model depends on the degree of precision of the digitized conversion process from the original part.

Bell [10] presents reverse engineering of a centrifugal compressor by using a 3-D imaging scanner. The part is scanned by means of two high-resolution cameras. As a result of the scan, millions of points generate a point cloud and by means of a CAD software these points are used to represent the solid model of the compressor. Between the scan and complete 3-D solid model handling, there are some intermittent repair and cleaning processes to be done. Due to some shiny or shaded regions, irregular shape formations may occur and these are corrected by applying some cleaning and repairing tools.

3-D scanning techniques are more applicable for the reverse engineering of a centrifugal impeller. It provides the chance of gathering more accurate results and it is more compatible with any CAD software for post-processing applications. When the complexity of the impeller shape increases, the CMM results occur to be less accurate. Moreover, there is a physical restriction due to the probe dimensions and its degree of freedom.

2.2 Geometric Modeling

2.2.1 General Definitions

The centrifugal compressor is composed of several parts which have to be separately modelled. In the modelling of a centrifugal compressor, the impeller, casing and diffuser are modelled independently and then assembled together to form the whole compressor geometry.

The impellers of a centrifugal compressor are either radial or twisted. Radial impellers are in fact defined in 2-D coordinate space. The solid radial impeller is the extruded version of a 2-D sketch. On the contrary, twisted impellers are fully 3-D shapes. The radial impellers are defined in (r, θ) plane while twisted impellers are defined in (r, z, θ) space. As a result, twisted impellers are more difficult to model and include many parameters for the definition of the full geometry.

Some important terminology used in the geometric modelling of a centrifugal compressor is given in Figure 6 and Figure 7 [11].

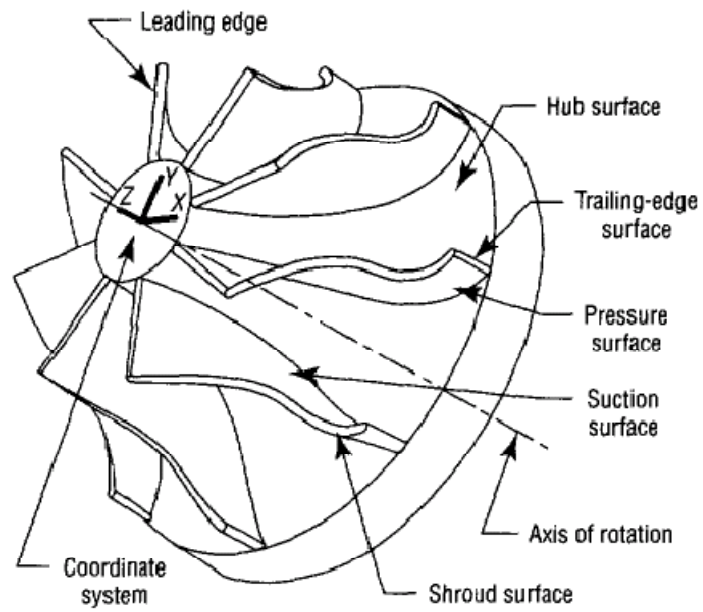


Figure 6 Entities of an Impeller

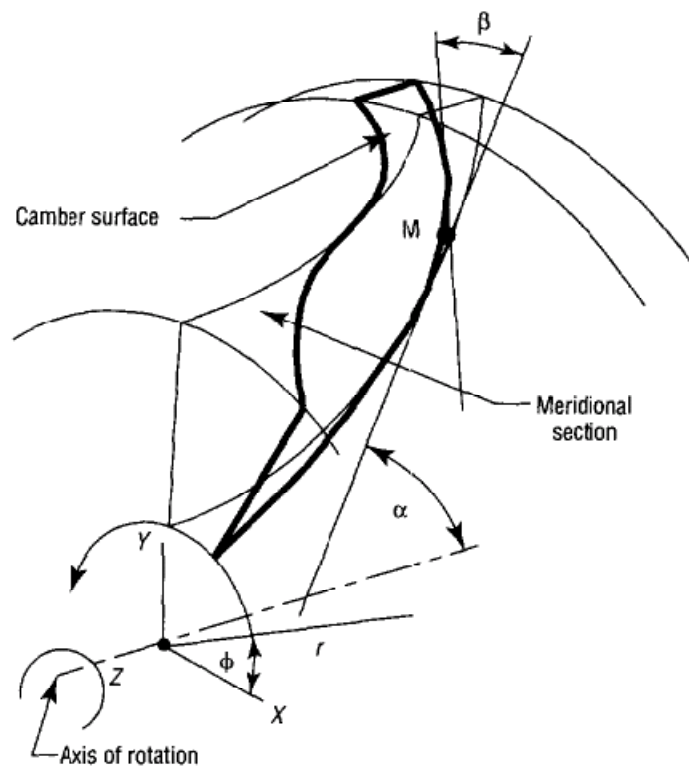


Figure 7 Coordinates, Meridional Section and the Camber

The definitions for common terminology used for centrifugal compressor geometry are given in Table 1.

Table 1 Important Terms & Definitions

Terms	Definitions
Hub	The conical surface which holds the blades of the compressor.
Shroud	The top casing that covers the compressor assembly.
Impeller	Name used for assembly of hub and the blades.
Splitter	Additional, smaller blades placed circumferentially between the main blades.
Blade Angle, β	The angle representing the amount of turn that a blade makes with respect to axial direction.
Theta Angle, θ	The angle that a blade covers which is measured from the beginning of the blade up to the end.
Camber Line	3-D curves formed by applying blade angle distribution over 2-D hub and shroud curves. It forms the mean-line of the blade profile.
Meridional Plane	A plane that cuts the hub and shroud surfaces through r and z axes.
Meridional Length, m	The length of curves measured in meridional plane.
Cut-off Ratio	Splitter hub or shroud curve meridional lengths divided by main blade hub or shroud meridional lengths respectively.
Radius Normalized Meridional Length, m'	Length defined for blade angle distribution equations which is in fact dm/r .
Pressure Surface	The concave surface of the blade along which the pressures are highest.
Suction Surface	The convex surface of the blade along which the pressure is lowest.
Leading Edge	The edge of the blades at the inlet which is the first boundary to force the fluid flow.
Trailing Edge	The edge of the blades at the exit.

2.2.2 Impeller Geometry Generation

Techniques used in the generation of impeller geometry depend on the needs of the study. For a design or optimization purpose, parametric geometry generation is suggested.

Surfaces are divided into two groups as algebraic and parametric surfaces. Algebraic surfaces are those which can be represented by implicit equations, while parametric surfaces are represented by means of patches. Bezier surfaces or NURBS are examples for parametric surfaces.

The algebraic surfaces offer solutions for data collection and fitting purposes, while parametric surfaces provide better, smoother control of curves and surfaces [12].

According to Casey [13], traditional geometry definition for turbo-machinery impellers involves either curve-fitting through many points or use of some polynomial expressions for blade shapes. Curve-fitting through many points has the disadvantage of weak controllability of the blade shape. Any requirement on the change of a point results in inevitable oscillations in the geometry. Use of smaller number of points which are joined by piecewise continuous segments decreases the need to large number of points. As a result, two techniques have been used widely in turbo-machinery modelling: Bezier curves and non-uniform rational B-spline (NURBS) curves. Grein et al. [14], Merryweather [15] and Casey [16] provide the geometry definition of turbo-machinery by using Bezier and NURBS curves.

The use of Bezier curves makes the definition of the geometry of any surface simpler. Both passages and blade surfaces can be modelled with equations of same type and these equations make the use of computer aided design easier [17]. However, Keskin [18] states the disadvantages such that, the modification of a

control point affects the whole geometry, therefore no local curve control, and use of Bezier curves for very complex shapes leads to use of more control points and constraints.

The first stage of impeller geometry generation is to define the meridional view in r - z plane. Then, the blade angle distribution is applied on hub and shroud curves to have the final 3-D hub and shroud camber curves. Finally, a surface is fit through the camber lines and after a thickness distribution around the surface, the 3-D solid impeller model is obtained. These distributions provide considerable flexibility in modern design. With thoughtful hub and shroud contour choice and appropriate blade angle distributions, a well-crafted impeller can be obtained as a result of optimization studies [19].

2.2.2.1 Meridional Channel

Meridional channel is defined in r - z plane which represents the through-flow geometry. The hub and shroud curves are defined as Bezier curves of any required degree as shown in Figure 8.

Formation of meridional channel is the first stage of geometric modelling. The 2-D hub and shroud curves which form the boundaries of the compressor are defined in this stage. Revolving the hub and shroud curves about the z -axis forms the hub and shroud surfaces.

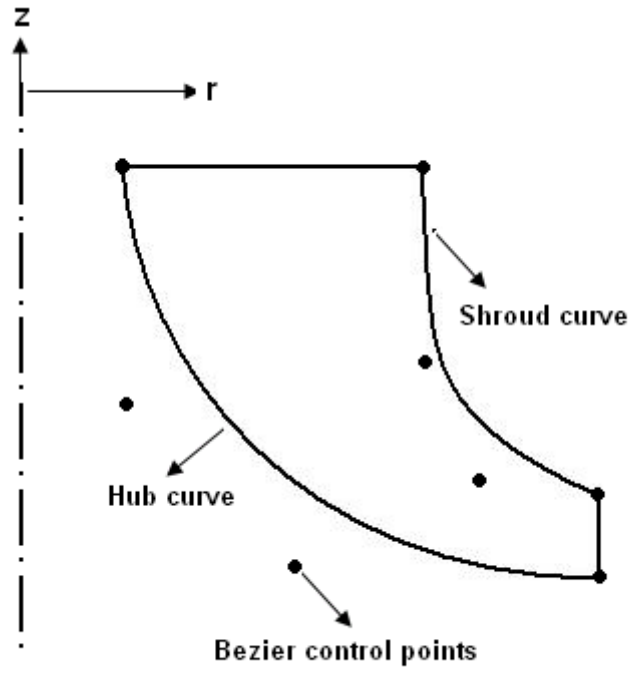


Figure 8 Meridional Channel

Bezier curves are represented with the following expression [20]:

$$\begin{pmatrix} r \\ z \end{pmatrix} = \sum_{k=0}^n \binom{n}{k} u^k (1-u)^{n-k} P_k \quad (2.1)$$

In equation (2.1), “n” is the degree of the Bezier curve. “u” is the Bezier parameter which varies between 0 and 1. P_k represents the corresponding control point coordinates in r and z. For n degree of curves, (n+1) number of control points is needed.

The Bezier curves pass through the first and the last control points. The rest of control points determine the slope of the curve between the first and the last control points.

The hub and shroud curves are generally represented by third or fourth order Bezier curves. Depending on the depth of analysis, fifth or more order Bezier curves can be selected to define the meridional section which brings more parameters to be studied and more computational effort.

2.2.2.2 Blade Angle Definition

The blade profiles are defined by a prescribed blade angle distribution, β , along the hub and shroud curves of interest. The blade angle distribution can be defined in several ways. The angle distribution is defined as a form of Bezier curve for which the non-dimensional Bezier parameter belongs to the hub or shroud curve's Bezier parameter. Moreover, angle distribution is also defined as a function of meridional length, m , or radius normalized meridional length, m' .

Harinck [21] and Van den Braembussche [22] define the blade angle β as:

$$\beta(u) = \beta_0 u^3 + \beta_1 u^2(1 - u) + \beta_2 u(1 - u)^2 + \beta_3 (1 - u)^3 \quad (2.2)$$

In equation (2.2), “ u ” is the non-dimensional Bezier parameter (0 at leading edge and 1 at trailing edge of the hub and shroud curves). β_3 is the blade angle at leading edge and β_0 is the angle at trailing edge.

In addition to Bezier definition of the blade angle, Benini [20] and Miller et al. [23] state that the blade angle is defined as a function of radius normalized meridional length. A sample definition is given in Figure 9.

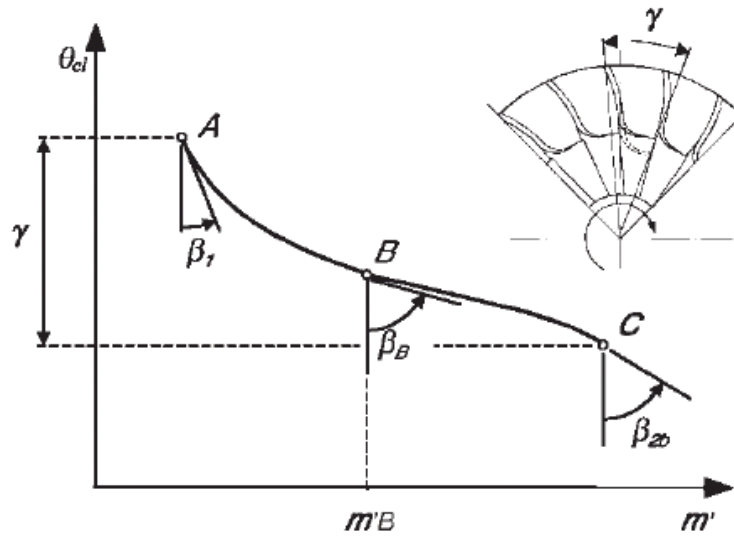


Figure 9 Blade Angle vs. m' [20]

2.2.2.3 Camber Line Generation

Camber line is the 3-D curve that forms the main profile of a blade. The camber lines are created by applying blade angle distribution over the 2-D hub and shroud curves of meridional section.

Conformal mapping method is used to create the camber line. In conformal mapping method, the theta angle is calculated from the blade angle distribution. Then, by using the theta angle, cylindrical coordinates are converted to Cartesian coordinates.

The steps to be followed for the generation of a camber line are listed below:

- The number of patches to be used in Bezier curves of meridional section is assigned by means of the Bezier parameter “u”. Then, by using the Bezier equation, the points on the Bezier curve are composed.
- The meridional length is the summation of lengths of all finite segments between points constructed. Therefore, increasing the number of patches results in more exact meridional length calculation.

$$m = \int_0^u \delta m \, du \quad (2.3)$$

$$\delta m = \sqrt{\delta r \cdot \delta r + \delta z \cdot \delta z} \quad (2.4)$$

- The radius normalized meridional length is given as:

$$dm' = \frac{dm}{r} \quad (2.5)$$

The definite integral of equation (2.5) between two points can be approximately calculated by means of the trapezoidal rule:

$$m'_2 - m'_1 = (m_2 - m_1) \left[\frac{\frac{1}{r_1} + \frac{1}{r_2}}{2} \right] \quad (2.6)$$

- The relation between the blade angle, β , and the theta angle, θ :

$$R d\theta = \tan \beta \, dm \quad (2.7)$$

The equation (2.7) can also be shown as:

$$d\theta = \tan \beta \, dm' \quad (2.8)$$

The definite integral of equation (2.8) between two points can be approximately calculated by means of the trapezoidal rule:

$$\theta_2 - \theta_1 = (m'_2 - m'_1) \left[\frac{\tan \beta_1 + \tan \beta_2}{2} \right] \quad (2.9)$$

- After the θ angle distribution is found, conformal mapping is used to translate the camber line coordinates to Cartesian coordinates [20].

$$x_{cl,i} = \frac{r_{cl,i}}{\sqrt{1 + (\tan \theta_{cl,i})^2}} \quad (2.10)$$

$$y_{cl,i} = \sqrt{r_{cl,i}^2 - x_{cl,i}^2} \quad (2.11)$$

The z-coordinates of the camber line are already calculated in meridional section curves.

2.2.2.4 Camber Surface Generation

Camber surface represents the 3-D blade surface without the thickness distribution. The camber surface is fit through the hub and shroud camber lines. Infinitely many surfaces can be created between the two curves. However, some restrictions are important while fitting a surface through the camber curves.

In literature, most of the surfaces are generated by using the “ruled surface” criteria and the use of ruled surfaces is mainly based upon the machinability of the impellers.

The machining of impellers with high local curvatures is a difficult task. Therefore use of point contact tools requires more time. However, using a tool with line contact is better for surface finish and ease of machining. Therefore, a blade shape formed by a ruled surface is preferred [11].

Most of the impellers are machined by flank milling. Iancu [24] states that for flank-milling machined impellers, the blade surface should be constructed by means of straight line elements. Then, the tool axis can easily collide with the straight line elements which makes the machining easier.

Chu et al. [25] also underscores the use of ruled surface in flank milled impellers and analyses the tool-impeller interference in machining. The tool-impeller interference is nearly negligible for the machining of ruled surfaces.

A ruled surface is defined by two boundary curves in space as can be seen in Figure 10 and Figure 11:

$$S(v, u) = (1 - v)A(u) + vB(u), \quad 0 \leq v, u \leq 1 \quad (2.12)$$

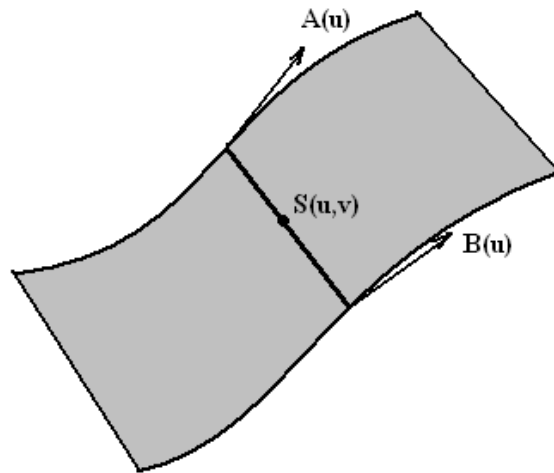


Figure 10 Ruled Surface by Two Curves

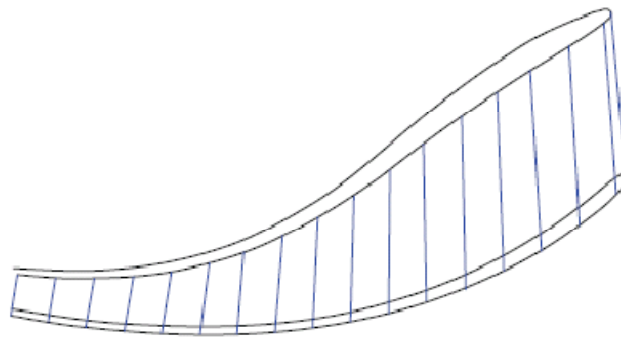


Figure 11 Ruled Surface by Straight Line Elements [24]

2.3 Computational Fluid Dynamics

2.3.1 General

Computational fluid dynamics (CFD) is today's most challenging and practically the most useful branch of fluid mechanics in which numerical methods are used to analyse the problems related with the fluid flow. Many engineering problems related with fluid flow can be analysed and predicted with acceptable accuracy. Computers are used to perform several operations depending on the complexity of the problem and the accuracy of the results expected. Advances in computer technology lead to more accurate and fast solutions even for very complex flow fields.

The general methodology followed during CFD analyses can be summarized as below:

- The geometry representing the physical boundaries of the problem is generated.
- The volume occupied by the fluid flow is divided into discrete grids (meshes). According to the geometrical complexity, the meshes can be generated as structured (uniform) or unstructured (non-uniform).
- The numerical simulation method is defined.
- The boundary conditions representing the restrictions or intervals of operation at physical boundaries are defined.
- The analysis is started according to the boundary and initial conditions with solver specifications defined before. The solution processes as steady-state or transient depending on the choice.
- Finally, the results are analysed or visualized by means of post-processing procedures.

The Navier-Stokes equations form the basis of continuum based CFD problems. Navier-Stokes equations coupled with the equation of state describe the fluid motion. The variations of fluid properties in three spatial dimensions and time are related with a set of partial differential equations.

The Navier-Stokes equations are derived from the law of conservation of mass and Newton's law of motion for fluid flow. Conservation of energy must also be included for compressible flows. The original equations can be modified by eliminating some terms according to the problem requirements. The conservation of mass is given in equation 2.13 as:

$$\frac{\partial \rho}{\partial t} + \nabla \cdot (\rho \vec{v}) = 0 \quad (2.13)$$

The conservation of momentum for constant viscosity coefficient is given in equation 2.14 as:

$$\rho \frac{\partial \vec{v}}{\partial t} + \rho(\vec{v} \cdot \nabla) \vec{v} = -\nabla p + \mu \left[\Delta \vec{v} + \frac{1}{3} \nabla(\nabla \cdot \vec{v}) \right] + \rho \vec{f}_e \quad (2.14)$$

In equations 2.13 and 2.14, \vec{v} is the velocity vector and μ is the dynamic viscosity coefficient of the fluid. $\rho \vec{f}_e$ represents the sum of external forces per unit volume.

For an inviscid flow the viscosity and hence the shear force term is zero. Eliminating this term forms the well-known Euler equation.

Very few analytic solutions of Navier-Stokes equations exist. Navier-Stokes equations are mostly solved by numerical methods [2]. The numerical solution requires the equations to be solved on a set of points in the fluid flow. Therefore, the discretization of the fluid flow reduces the partial differential equations to difference equations and these equations are solved by appropriate techniques like finite difference, finite element and finite volume. As a result, grid generation is another challenging process itself and should be formed such that the resulting network lead to reliable solutions.

It is not necessary to model the flow in 3-D for all engineering flows. There may be cases where two dimensional solutions can be easily adopted to fluid flow analysis. With a few steps, the solutions of two-dimensional analysis can be transferred to three-dimensional results which reduces the computational effort and time needed for analysis.

2.3.2 Application to Turbomachinery

The geometry of the centrifugal compressors are complex. Having 3-D twisted blades and being assembled with a stationary diffuser make the computational fluid dynamics analyses difficult and time consuming.

The aerodynamic analysis for a turbomachinery covers the calculation of full flow field of a blade passage including primary and secondary flows. The flow phenomena inside the blade passages of the impeller and inside the diffuser are highly complex. Therefore, three-dimensional analysis of the fluid flow is to be accomplished and codes are available for this purpose.

For many fluid flows in a turbomachinery, simplifications to the Navier-Stokes equations are applicable. Therefore, it may not be efficient to solve the Navier-Stokes equations including all the terms for all flow fields within a turbomachinery. The technique to be employed for the computation of a flow field in a turbomachinery depends on the geometry, the flow regime and the objective of the analysis. The major effects can be captured by Euler equations and then viscous effects can be held by using some boundary layer codes [45]. According to Lakshminarayana [45], the Euler codes have matured and are routinely used in the design and analysis of flows within turbomachineries.

According to Japikse [2], there are many cases in turbomachinery analysis where it is quite applicable to represent the fluid flow in two dimensions and ignore small variations in fluid properties in the third dimension.

The fluid flow in a blade passage can be represented on two surfaces as in Figure 12. The S1 surface represents the blade-to-blade surface, where S2 represents the hub-to-shroud surface. For two dimensional analysis of the fluid flow in blade passages,

these S1 and S2 surfaces are used. The flow is constrained to follow one of the surfaces. The solutions are obtained separately for both surfaces and the results are interacted, iterated and modified between two surfaces. As a result, quasi-three-dimensional solutions are obtained.

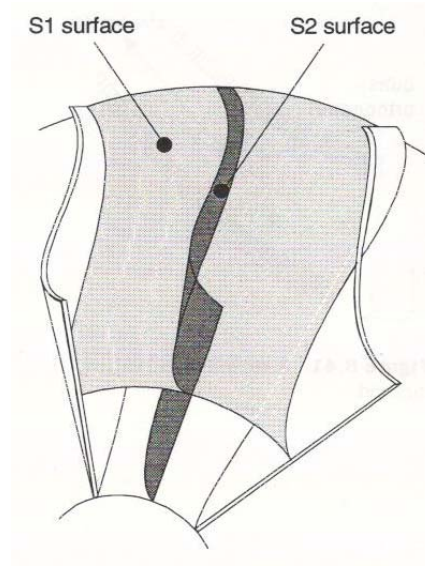


Figure 12 Flow Surfaces S1 and S2 for a Centrifugal Impeller [2]

The solution for a turbomachinery can be inviscid or viscous depending on the case and the purpose of the analysis. The inviscid solution methods are two and three dimensional potential flow solutions, two dimensional and quasi-three-dimensional stream function solutions and two and three dimensional Euler solutions. In streamline curvature method, the streamlines are used as grid lines. The velocity gradient along an arbitrary quasi-orthogonal, which are straight lines across the passage, is determined by using the momentum equation. Katsanis [28] applied this method for a radial inflow turbine with splitter blades and obtained a quasi-three-dimensional solution by using the hub-to-shroud analysis followed by blade-to-blade analysis. Moreover Smith et al. [29] and Wu [30] also used the same two-dimensional methods and obtained quasi three-dimensional solutions for centrifugal impellers. If the pressure distribution is of interest, the inviscid codes are the most

appropriate solutions for flow within a turbomachinery provided that viscous regions are small [45].

For flow regions where inviscid solutions cannot predict the flow field with required accuracy, viscous solutions are preferred. Viscous studies are mainly performed for turbomachinery analysis which are expensive and time consuming to run. Reynolds-averaged-Navier-Stokes equations are used for turbomachinery analysis with a turbulence model. One of the most popular simplifications made to the Navier-Stokes equations is "Reynolds Averaging". This simplification to the Navier-Stokes equations involves taking time averages of the velocity, pressure and temperature terms in the equations.

The turbulence model used in an analysis is another important issue. k - ϵ and k - ω models are the most common two equation turbulence models in literature. k - ϵ is the most common model used in turbomachinery analysis due to its simplicity and less computational effort with respect to k - ω . For wall bounded and internal flows, the k - ϵ model gives good results if pressure gradients are small. If there exists large adverse pressure gradients, the accuracy of k - ϵ model reduces [31]. Therefore, use of k - ω model is provided where high pressure gradients are expected. Although k - ω appears to be more useful for turbomachinery analyses, k - ϵ model is used more due to the need of less computation effort.

Ling et al. [6] used a CFD package to analyse the flow through centrifugal compressor impeller and diffuser. A rotational periodic boundary condition is applied to one passage of diffuser and impeller section. The diffuser and impeller are meshed independently and two domains are connected by General Grid Interface with non-matching grid which iterates and checks the flux balances. k - ϵ turbulence method is used which does not give information about flow separations, but sufficient to obtain performance data.

In addition to Ling et al. [6]; Benini et al. [20] used $k-\epsilon$ in the study of a diffuser-impeller interaction. Wu et al. [32] again used $k-\epsilon$ model to analyse a hydro turbine and the results are verified by testing. Pazzi et al. [27] studied on the optimization of a centrifugal impeller and suggested to use a $k-\omega$ turbulence model for CFD analysis. Instead of two-equation turbulence models, Kuzmenko et al. [33] used Spalart-Allmaras one-equation turbulence model. This model results in satisfactory outputs while requiring small computational resources. Kim and Seo [34] study on the design optimization of a centrifugal fan and uses $k-\epsilon$ turbulence model. Briefly, although the $k-\omega$ can provide more accurate results, the use of $k-\epsilon$ model is more common since the accuracy of the $k-\epsilon$ turbulence method seems good enough for designers.

There are many software specially designed for obtaining fluid flow solutions. With these codes, the grid generation and fluid flow solutions can be obtained for any type of problems. The grid generation can be parametrically done and the meshed geometry can automatically proceed to the solution process. Therefore, these codes provide flexibility and time saving in turbomachinery analysis and design. The restrictions, boundary conditions and the solver type is given as input and after the grid generation, the codes solve the problem according to the conditions supplied before the analysis.

A centrifugal compressor system is an assembly of the impeller and the diffuser. Then, the system is modelled by assigning different frames of reference regarding the rotating impeller and stationary diffuser. Therefore, a suitable interface model between the impeller and the stationary components is needed. There are three different techniques to handle such cases. These are frozen rotor, circumferential average and transient sliding mesh models [35]. In circumferential averaging, the upstream flow velocity is firstly averaged circumferentially and the data is then transferred to other reference of frame. For the frozen rotor case, the flow profile in the circumferential direction is kept fixed across the interface. The frozen rotor and the circumferential averaging techniques can be used to couple portions of flow path.

In transient sliding mesh technique, a sliding interface is used between the moving mesh of the impeller side and the non-moving mesh is made to slide past the stationary part. Information exchange continuously occurs across the interface [35].

According to Liu's studies [35], frozen rotor provide over-predicted results, while circumferential averaging and sliding mesh techniques give reasonable results. The transient sliding mesh method is necessary to predict the inherently unsteady flow field of a centrifugal compressor.

2.4 Design of Experiments & Optimization

The centrifugal impeller geometry contains many parameters to be investigated during the design and optimization processes. In order to find the most suitable configuration of parameters for the objective desired by the designer, a methodology to reach the optimum in an efficient way is to be followed.

The optimization is the process of reaching a better solution according to specified objectives and constraints. During the optimization process, all the parameters of interest are investigated thoroughly and their effects on the objective is analysed. However, the number of parameters is an important criteria in optimization studies. As the number of parameters increase, the computational effort and the necessary time to complete the study increases.

The optimization process is in fact a maximization or minimization of an objective function by taking care of the necessary constraints. The objective function may be an already existing correlation between the input parameters and the output, or the relation between the inputs and the output may be defined by fitting a function that satisfactorily shows the behaviour of the relation. There exist many methods for

fitting purposes in literature, but the most illustrative is the choice for the optimization studies.

The effects of parameters are examined in an optimization study. The effects can influence the response individually or jointly with other parameters [36]. For an optimization study, a combination of overall parameters are chosen from a set of parameter combination list. The list of discussion may be formed by combining every possible value of parameters with each other. Therefore, for optimization studies regarding too many parameters, a large table of parameter value combination is obtained which is not desired due to computational effort and waste of time.

In statistics, the parameters are called “factors” and the values of the parameters are called “levels”. The combination of parameters and their corresponding values form the so called design space. In an optimization study, all the factors and their values can be combined with each other in order to investigate any effect of the factors and their relations with each other. This is called “full factorial experiment” which is not desirable for large number of parameters as mentioned above [36]. Therefore, a design space which is smaller in size, but leading the optimization study to a reliable and accurate enough result can be defined by using several methods.

There are many methods in literature in which definitions of the methods are provided with explanatory samples. The main objective of using design of experiments is to guide the optimization studies in such a way that reliable and acceptable accurate results are obtained with less computational effort and within less time.

The formation of design space and the optimization code used in a study are generally coupled. The design of experiments method is executed according to the

optimization strategy to be used. In the upcoming paragraphs, a literature survey on the design space formation and optimization studies applied for the optimization studies in turbomachines is summarized. The optimization and design of experiments methodology cover many different techniques which can be chosen according to the problem characteristics.

Papila [37] provides a neural-network and polynomial based response surface strategy for the optimization of a supersonic turbine. A shape optimization with 10 variables is done by means of suitable design of experiments approach followed by the response surface and neural-network methods to reach the optimum, and the comparison of the methods are provided.

Harinck [21] and Van den Braembussche [22] used the artificial neural-network methodology combined with Genetic Algorithms which is a quasi-stochastic approach based on “natural selection” and Darwin’s “survival of the fittest” principle. Genetic Algorithm is used to minimize the objective function. The database generated after the Genetic Algorithm stage is used in artificial neural network (ANN) to predict the objective function. ANN is a very fast predictor and allows the evaluation of the objective function of the many geometries generated by the Genetic Algorithm. The predicted result of the ANN method is verified by making analysis in a Navier-Stokes solver. The optimization cycle is stopped until the prediction of ANN and the Navier-Stokes solver is in an agreement. This optimization cycle is summarized in Figure 13.

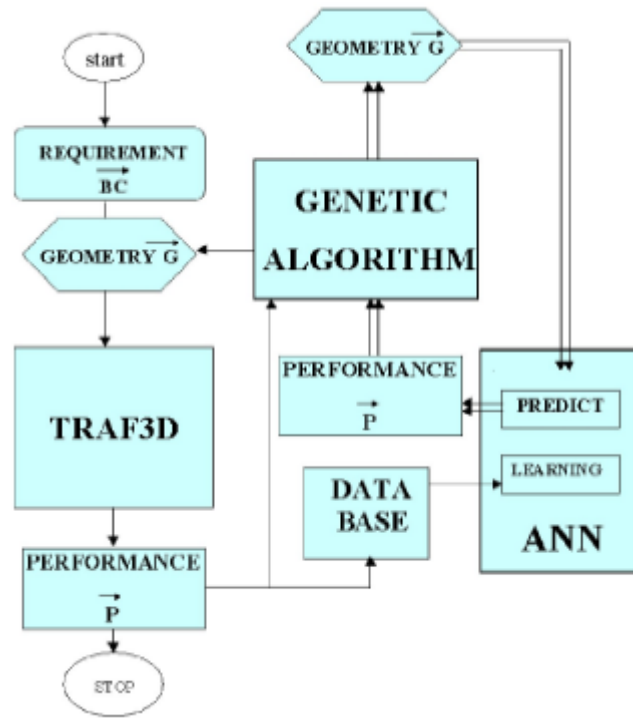


Figure 13 Genetic Algorithm with Artificial Neural Network (ANN) [21]

Wu et al. [38] used artificial neural network with back-propagation (BP-ANN) method for the optimization of the manufacturing of centrifugal pump impellers for higher efficiency that the existing design cannot offer. In this study, the BP-ANN is trained with a set of samples from CFD simulations. The design space is formed by orthogonal arrays to obtain the combination of impeller geometric parameters that are uniformly distributed. The well-trained BP-ANN is used to predict the optimum geometry and the predictions are verified with CFD solutions.

Japikse and Platt [39] use a different technique for the design optimization of a centrifugal compressor, but the methodology is the same. Only the codes leading to optimization are different. 280 trial configurations are obtained through the geometrical parameters and by using “simulated annealing” technique, a wide selection of possible designs were searched until the best domain is established which is needed for another subsequent optimization process. The subsequent

process is the “hill-climbing” technique which is used to iterate to the final values with the lowest objective penalty function. The simulated annealing method is a technique related to stochastic optimization just like the Genetic Algorithm.

2.4.1 Design of Experiments (DOE)

The representation of the design space is an important step of an optimization study. The predictive capability of Response Surface Method (RSM) or Neural-Network is greatly influenced by the distribution of sampling points in space. The even distribution of points are obtained such that their evaluation in RSM or Neural-Network results in acceptable accuracy.

The analysis of variance principle is the heart of the design of experiments. The main objective is to maximize the amount of information gathered about the effect of parameters with few observations as much as possible.

The optimization of a centrifugal compressor is a challenging and time consuming study. The analysis period takes longer with increasing number of parameters and the size of their interval of interest. Instead of taking all the parameter combinations into the optimization process, considering some portion of the overall combinations such that the selected combinations can represent the system behaviour is the purpose of design of experiments studies.

A full factorial experiment includes all possible factor-level combinations in an experimental design. For the vast majority of full factorial experiments, the factors are chosen to have only two levels. Therefore 2^n number of designs are generated for the experiment where n denotes the number of parameters. If the number of combinations in a full factorial design is unfeasible, the experimental designs called “fractional factorial design” are applied which provide less combinations.

The design of experiments methods are mainly categorized as modern and classical methods. The classical methods were developed for simple experimental configurations due to lack of computerized power. They are especially used in experiments where results are not repeatable. However, the computer analysis results are repeatable and there are no random errors associated with the experimentation. The classical methods use fixed structures, while modern methods are iterative and flexible [46]. The choice of methodology depends on the case, but modern methods try to optimize the design space such that the best available data set is obtained for the study of interest.

There are many techniques used in the formation of design space. In this section, the most common techniques will be examined. These are face centered cubic design and orthogonal arrays as the classical methods, and I and D-optimal designs as the modern methods.

2.4.1.1 Orthogonal Arrays

In a design space formed by orthogonal arrays, each level of a factor occurs an equal number of times with each level of each of the other parameters (factors). An orthogonal array is in fact a fractional factorial matrix which uses only a fraction of the factorial design points.

The orthogonality of the columns is an indication of a better design. The comparison of an orthogonal design and non-orthogonal design is given in Figure 14.

Orthogonal Array			Nonorthogonal Array		
Factors: A	B	C	Factors: A	B	C
1	1	1	1	1	2
1	2	2	1	2	1
2	1	2	2	1	2
2	2	1	1	2	1

Figure 14 Orthogonal vs. Non-Orthogonal Design Space [36]

The use of orthogonal arrays can significantly reduce the number of experimental configurations when compared to the full factorial experiment designs. Orthogonal arrays is one of the most efficient fractional factorial design methodology. In an orthogonal array table, balance is achieved because each level of a factor occurs an equal number of times with each level of each of the other factors. Note that all complete factorials in which there are an equal number of repeats for each factor-level combination are orthogonal arrays.

2.4.1.2 Face Centered Cubic Design

Face centered cubic design allows a design space which is composed of eight points at the corner, one at the center of the cube and four at the center of the faces as can be seen in Figure 15. Therefore, the number of designs is $2^n + 2n + 1$ where “n” is the number of design parameters. The face centered cubic design is mainly used for fitting second-order response surfaces [37].

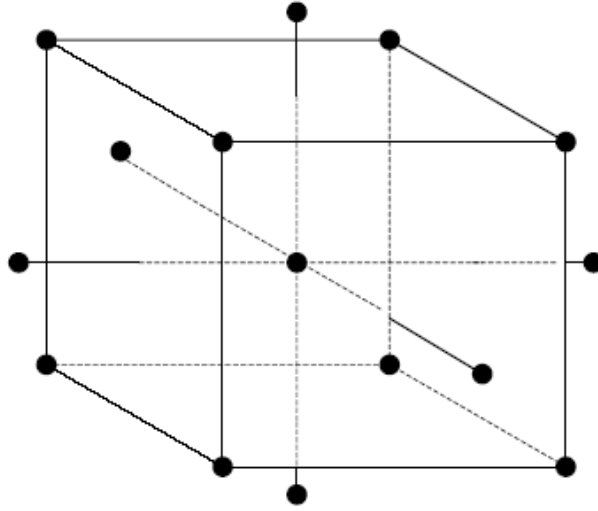


Figure 15 Face Centered Cubic Design

2.4.1.3 I-optimal and D-optimal Designs

The modern experiment designs are generally defined to somehow minimize a term derived from prediction variance so that prediction variance in certain regions or all over the area of interest is minimized. I-optimal and D-optimal designs are common modern experiment design methods.

Prediction variance at an arbitrary point x can be found as:

$$var\ y(x) = \frac{\sigma^2}{n} f(x) M_x^{-1} f(x)' \quad (2.15)$$

where σ^2 is the standard deviance of the regression errors and n is the total number of design points. $f(x)$ defines the array of effects such that:

$$f(x) = [1, x_1, x_1^2, x_2, x_2^2, x_1 x_2, \dots] \quad (2.16)$$

where x_1 and x_2 denotes the main effects of each factor, while x_1x_2 denotes the joint effect of the factors x_1 and x_2 .

$$M_x = \frac{1}{n} X'X \quad (2.17)$$

X is the design matrix formed by $f(x)$ arrays as rows for each sampling points.

D-optimal refers to a type of experiment design that attempts to produce the most accurate coefficients for a model. “D” stands for “determinant” which is useful in generating these designs where $D=|M_x|$. This design tries to minimize the prediction variance of the model. D-optimal designs are useful when the effect of each parameter is to be investigated thoroughly. The minimization of the prediction of variance is carried out by maximizing the determinant, D .

I-optimal refers to a design that attempts to provide the best predictions for any given trial. This is the best method if the accuracy response to be predicted is important. The design space is created according to the minimization of the average (integral) variance for a design. “I” stands for “Integrated Variance”.

2.4.2 Response Surface Method

Response surface methodology is a collection of mathematical and statistical techniques used for developing and optimizing a process. This technique uses the design space generated by the design of experiments studies, and fits a surface that represents the behaviour of the parameters. Response surfaces are models used to predict input – output relations of complex systems with rather simple polynomials.

The design space generated by full factorial or fractional factorial (composite design, face centered design etc.) methods can be efficiently fit through a response surface model [36].

The second order (quadratic) response surface model can be written as [40]:

$$y = \beta_0 + \sum_{i=1}^k \beta_i x_i + \sum_{i=1}^k \beta_{ii} x_i^2 + \sum_{i=1}^k \sum_{j=2}^k \beta_{ij} x_i x_j + \epsilon \quad (2.15)$$

where y is the response variable and ϵ is the error. x terms represent the parameters or namely the design variables. The subscript “ij” denotes the joint effect of variables.

A first order response surface only includes the main effects of the variables themselves. However, by using a second order response surface, the joint effect of each variable with another variable is also included in design.

At the beginning of an optimization study, the response values are not known. Therefore, the β terms in response surface equation are unknowns. After getting the necessary amount of experimentation data, the response variable is defined and the β terms are found by using a regression analysis.

When the polynomial representation of the response surface is obtained, determining the factor levels that conform the optimum response is of interest. The optimum can be handled by drawing the contour plots of variables or by using some mathematical techniques to get the optimum point. All the stationary points of the response curve can be calculated and the local and global maximums or minimums are obtained.

2.4.3 Artificial Neural-Network Method

An artificial neural-network is a system based on the operation of biological neural networks. A neural network conducts an analysis of the information and provides a probability estimate that the data matches the characteristics which it has been trained to recognize [41].

The use of neural-network has many advantages. A neural-network can perform tasks that a linear code cannot do. If an element of the network fails, computation continues with a parallel nature. It is a self-learning code which does not need to be reprogrammed. The main disadvantages of using neural-networks are high computation time and database training requirements.

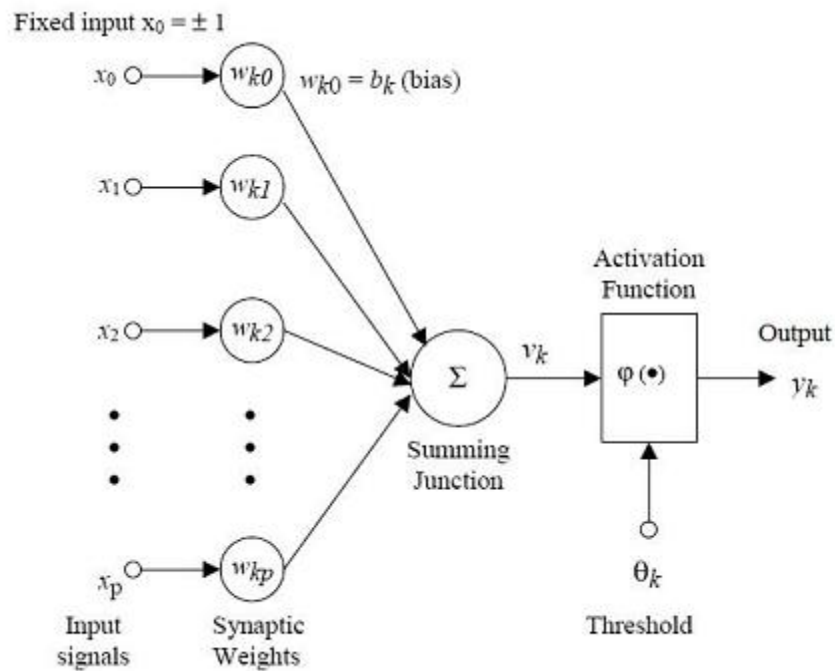


Figure 16 Artificial Neurons [42]

Figure 16 shows a general structure of an artificial neural network. Artificial neurons consist of the summing junction which sums the inputs with certain weights, threshold, activation function and the output. There are many activation functions in literature which can be selected according to the problem to be investigated. Non-linear least-squares regression is used to determine the values of weights.

The artificial neural networks are useful in the modelling of non-linear systems. However, it has a risk of over-fitting which is defined as fitting a model which has too many parameters. Therefore, the ability of emulating the actual system is reduced due to the increase of arbitrariness [43].

In order to handle the over-fitting problem, neural-networks are generally fitted with holdback samples to cross validate the model which are not used in the estimation process. The data used for fitting is the training data, while the data used for cross-validation are the holdback samples.

CHAPTER 3

COMPRESSOR GEOMETRY MODEL

The original geometry of the centrifugal compressor is a complex and 3-D twisted geometry which composes of the impellers, splitters, inlet & exit spaces and a diffuser.

In order to obtain the full geometry of the centrifugal compressor, a reverse engineering methodology is followed. The turbojet engine is carefully disassembled until the centrifugal compressor is clearly observed. Then by using optic scanning on the engine, a 3-D model of the compressor is gathered. Then, the model is processed on Unigraphics NX software to handle the parameterized model of the compressor.

3.1 Engine Disassembly

One of the important steps of reverse engineering applications is the disassembly process. The engine is disassembled with attention and every step is recorded by taking pictures and numbering related parts. Since only the compressor part is the main interest of the study, all the part of the engine are not disassembled.

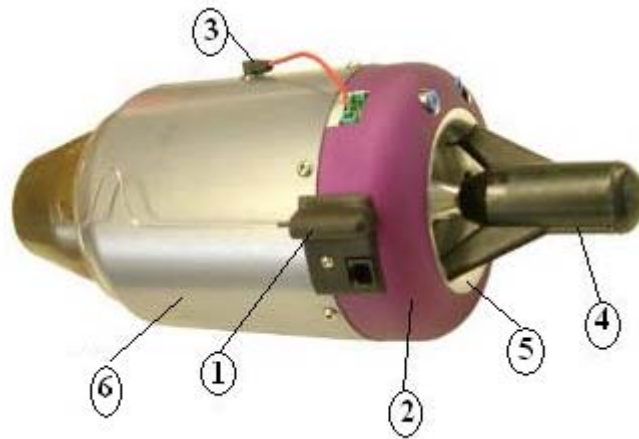


Figure 17 Disassembly Sequence

The disassembly sequence of the small turbojet engine is described below briefly (Figure 17) and some disassembled parts are shown in Figure 18:

- Firstly, the thermocouple extending from the inlet casing up to the nozzle exit is disassembled.
- The pink casing that covers the electronic circuitry and the compressor assembly is removed.
- The electronics related with the ECU (Engine Control Unit) is taken out, but the line connecting the starter motor and the circuit is kept alive.
- The starter motor assembly is pulled out with the rest of the electronic circuits.
- The shroud casing that covers the centrifugal compressor is disassembled and the impellers of the compressor become evident.
- The fuel feeding system and the thin body structure (no.6 in Figure 17) are taken out. Both the impellers and the diffuser can easily be reached after this stage.

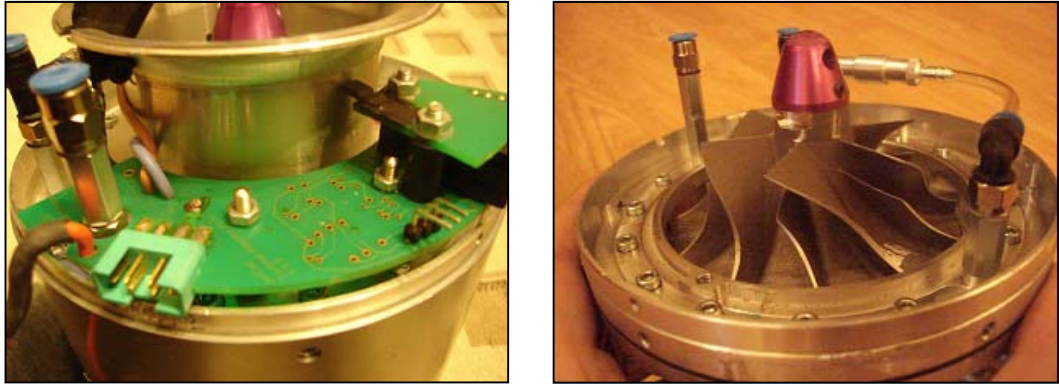


Figure 18 Disassembly of the Engine

3.2 Optical Scanning

The geometry of the centrifugal compressor is a complex 3-D shape. Initially, the points of hub and shroud camber lines are intended to be measured by means of a CMM device. However, the small and deep gaps of the compressor make it difficult to measure by means of the existing probe. As a result, 3-D optical scanning methodology is used to obtain the 3-D model of the original geometry.



Figure 19 optoTOP-HE 3-D Optical Scanner

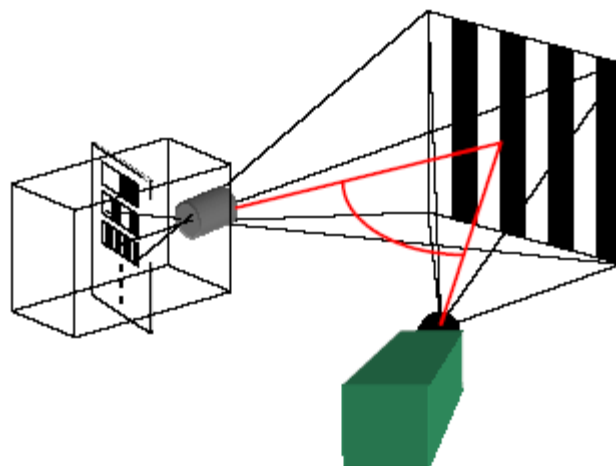


Figure 20 Working Principle of an Optical Scanner [26]

Figure 20 shows the working principle of an optical scanner. Optical scanners work on the basis of using structured light. A known pattern of light is projected on the object and a camera records the image of the pattern with the real image of the part. The system composes of two cameras. One of the cameras act as a light source which illuminates the part with a known pattern, while the other camera tries to digitize the illumination and get the image of the part [26].

The complex geometry of the compressor is obtained by means of optical scanning with an optoTOP-HE optical scanner (Figure 19). High definition scanners allow the 3-D digitizing of parts with high resolution and accuracy.

In order to have better results, some precautions are taken:

- The whole compressor is powdered in order to make the shiny surfaces disappear.
- The compressor is positioned such that the scanner can reach all the deepest sides of the part.
- Since the compressor is rotating part, it is fixed by means of restricting the motion of the shaft passing through the whole engine.
- Any properties near the scanner setup that can shade the compressor are carried away.

The output of the optic scanner (Figure 22) is a faceted 3-D model which cannot be edited by means of any modelling software. Although the necessary precautions are taken, there are irregular patterns on the output like holes and incomplete curves. However, the required procedures can be applied on that model by using the smooth regions. Only measurement and curve fitting through facets are available on the scanner output model. Figure 21 shows the original compressor geometry with its diffuser. Figure 22 is the result of 3-D scanning.



Figure 21 Original Compressor Geometry

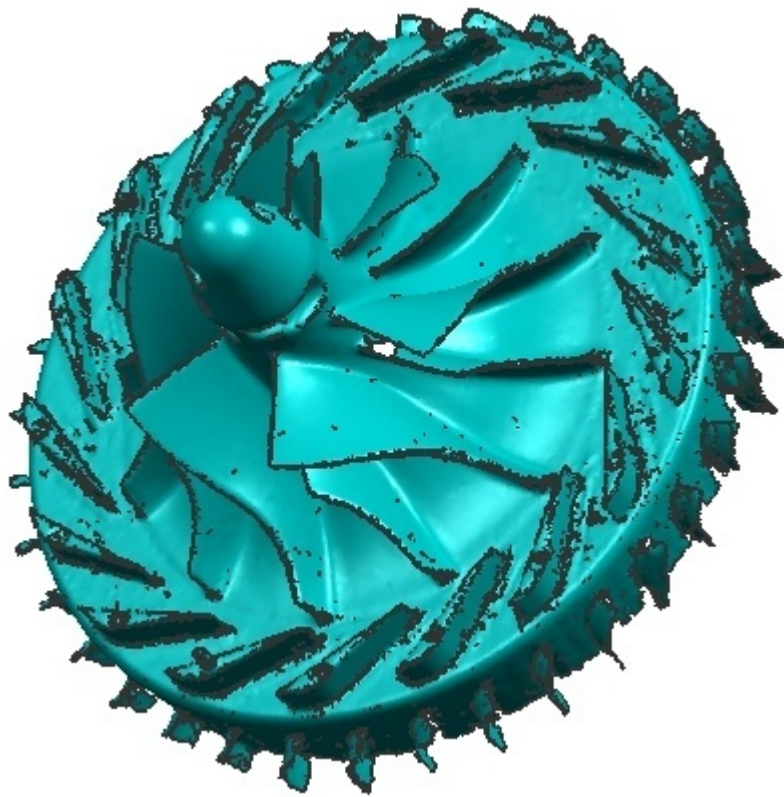


Figure 22 Optic Scanner Output

3.3 Geometry Generation

In order to have a parameterized model of the centrifugal compressor, the scanner output model is processed in Unigraphics NX software environment. Two splines are created on hub and shroud camber lines and by creating a ruled surface through these splines, the 3-D impeller geometry is obtained.

In Figure 23, the red curves are the hub and shroud camber lines for the splitter and the main blade. These curves are formed by passing splines through the facets on the mean edges of the blades.

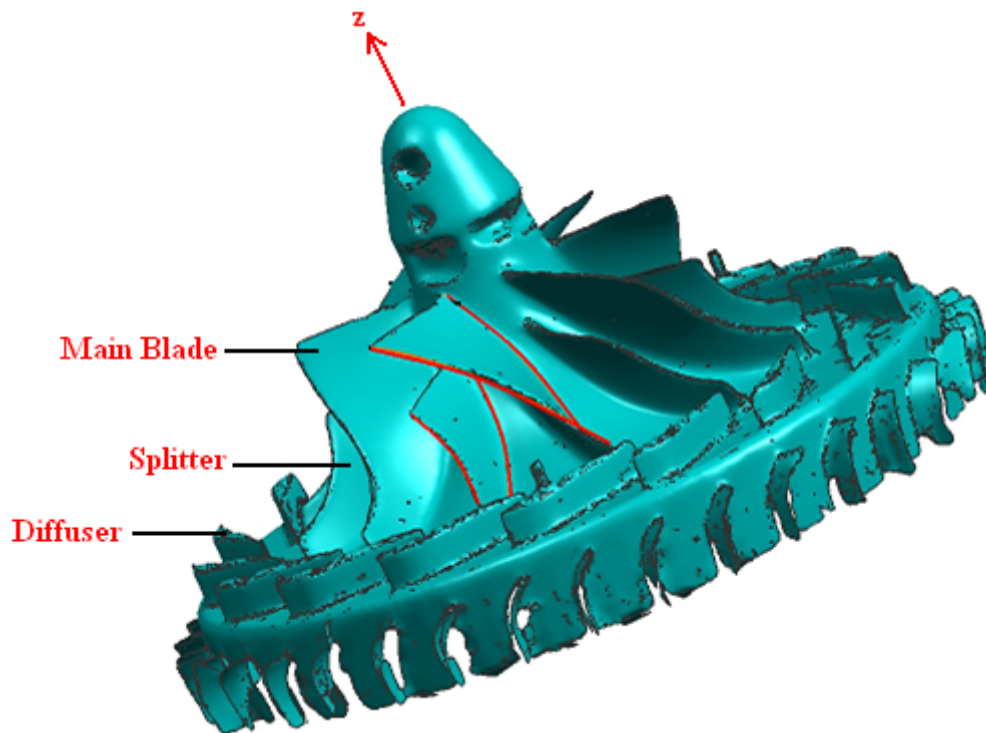


Figure 23 Hub & Shroud Curve Formation

The camber surface of the splitter and the main blade is formed by fitting ruled surfaces between the hub and shroud camber lines. “Ruled surface” command of the UGS NX software is used to fit the desired surface.

The blades formed by ruled surfaces are easy to manufacture and provide better efficiency. Therefore, use of ruled surfaces is a means of concurrent engineering.

By revolving the hub and shroud camber lines about the z-axis, the hub and shroud surfaces are obtained. Then, intersecting hub and shroud curves with z-r plane gives the meridional curves for both hub and shroud. The splitter and main blade camber surfaces formed by ruled surface fitting and the corresponding meridional sections are given in Figure 24.

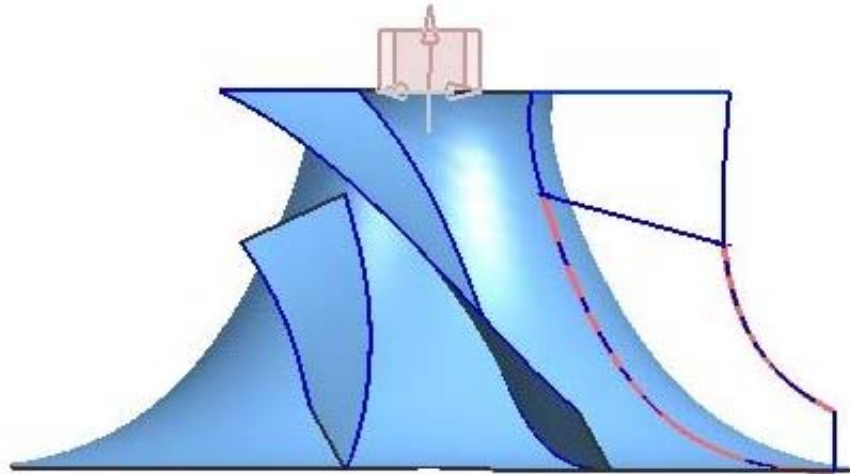


Figure 24 Splitter, Main Blade Camber Surfaces and Meridional Section

In order to have the final geometry without the diffuser, thickness distribution is applied on the camber surfaces shown on Figure 24, and the solid blade and the splitter is copied around the z-axis such that 6 main blades and 6 splitters are generated. The finalized model of the compressor without the diffuser is given in Figure 25.

The diffuser geometry is obtained by fitting the necessary curves over the faceted surface of the original diffuser. Then, these curves are extruded to form the solid diffuser geometry. By using the Unigraphics NX “assembly” abilities, the separately sketched impeller and diffuser sections are assembled as shown in Figure 26.

The final geometry obtained is not parametric. Therefore, it can be only used in the initial analysis. In order to study on the optimization of a geometry; a parametric, flexible geometry is needed.

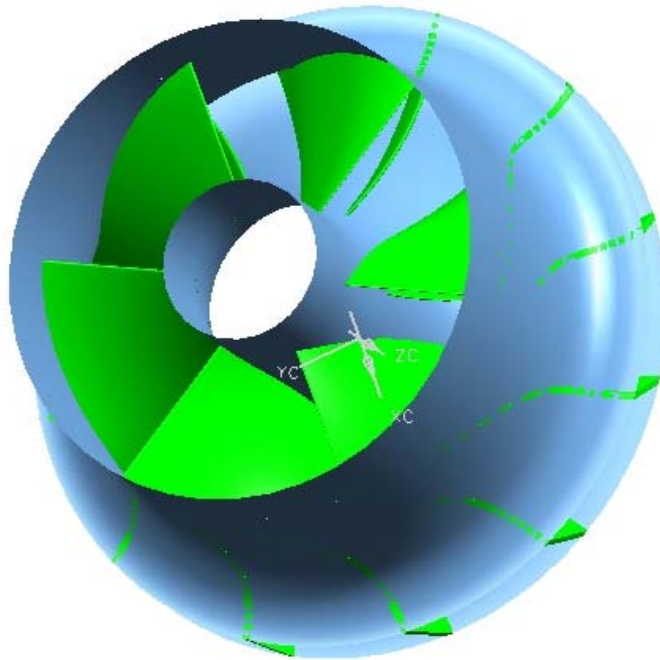


Figure 25 3-D Model of the Impellers and the Shroud Casing

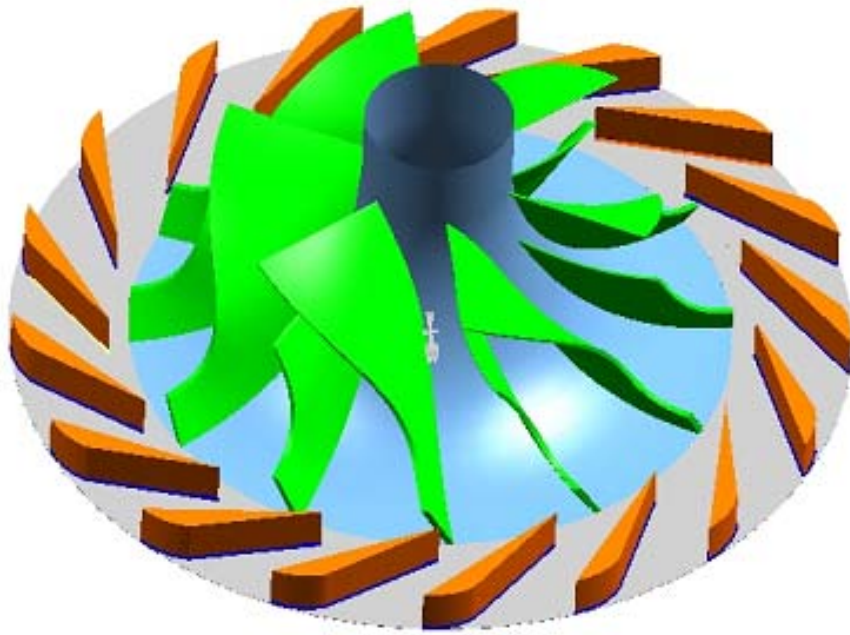


Figure 26 Impeller-Diffuser Assembly (Casing removed)

3.4 Parameters and Dimensions

For the optimization studies of the centrifugal compressor geometry, the geometry to be analysed is modelled as a parametric, flexible and easy to manipulate model. Therefore, the 3-D model of the compressor is to be generated parametrically through the 3-D modelling software.

The main parameters to be considered in centrifugal impeller modelling are thoroughly explained in Section 2.2.2. The values corresponding to the parameters of the original geometry is given in this section.

The meridional curves are obtained by intersecting the z - r plane with the hub and shroud surfaces. The intersection curves are then fitted by a third degree Bezier curves with 4 control points. Two points of the four control points belong to the points at the inlet and exit of the curves.

The Bezier curves and the corresponding control point coordinates (z , r) are given in Figure 27.

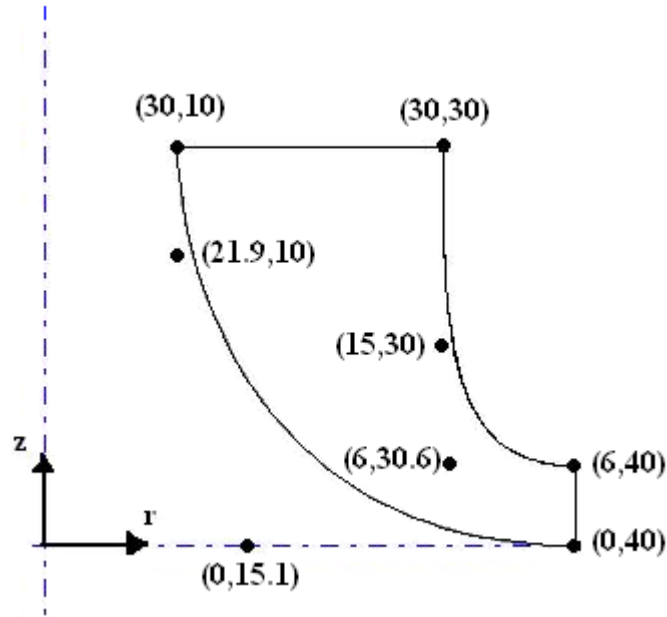


Figure 27 Bezier Control Points for Original Geometry Meridional Section

Some restrictions are applied during Bezier fitting for the meridional curves. As stated by Toker [17], dr/dz at the inlet of hub and shroud curves and dz/dr at the exit of the curves should be zero for structural and manufacturing concerns. Also Van den Braembussche et al. [22], Harinck et al. [21] and Pazzi et al. [27] use the same concept in their geometric models. Therefore, in order to have zero slopes at the suggested points, the Bezier control points next to that point must lie on the same line parallel to the axis. Then, Bezier curves are fitted according to the described restriction.

The cut-off ratio which defines the length of splitter at the hub and shroud are measured in the meridional view. The meridional length of hub and shroud curves of splitter and the main blade are measured and the cut off ratios are calculated by dividing the splitter hub/shroud curve lengths with the main blade hub/shroud curve lengths.

The blade angles β , θ and the thickness of the blade are measured by using measurement tools of the 3-D modelling software UGS NX. Splitters use the main blade's angular and thickness distribution. Therefore, the main blade is created initially and then splitter models are obtained by applying the related cut-off ratios on the main blade.

The blade angles on hub and shroud at the exit are measured to be 5° and 10° respectively. Analyzing the original geometry model shows that the blades are of “backswept” or “backward-curved” type. Namely, the relative velocity of the fluid exiting the blades makes an angle with the surface normal.

The main parameters to form a parametric centrifugal compressor model and their values for the original case is summarized in Table 2 and Table 3. In Table 3, the Bezier control point coordinates are tabulated. The subscripts “h” and “s” denote hub and shroud respectively, while “z” and “r” represent the axial and radial coordinates.

Table 2 Parameters and Values

Parameter Name	Symbol	Value
Blade inlet angle (hub)	β_{ih}	45°
Blade exit angle (hub)	β_{eh}	5°
Blade inlet angle (shroud)	β_{is}	69°
Blade exit angle (shroud)	β_{es}	10°
Inlet theta angle (hub)	θ_{ih}	0°
Exit theta angle (hub)	θ_{eh}	57°
Inlet theta angle (shroud)	θ_{is}	0°
Exit theta angle (shroud)	θ_{es}	52°
Splitter cut-off ratio (hub)	COR_h	0.8
Splitter cut-off ratio (shroud)	COR_s	0.6
Thickness	t	1 mm
Number of blades	N	6 main blades + 6 splitters

Table 3 Bezier Control Point Coordinates (mm)

HUB SIDE				SHROUD SIDE			
P_{h1z}	30	P_{h1r}	10	P_{s1z}	30	P_{s1r}	30
P_{h2z}	21.9	P_{h2r}	10	P_{s2z}	15	P_{s2r}	30
P_{h3z}	0	P_{h3r}	15.1	P_{s3z}	6	P_{s3r}	30.6
P_{h4z}	0	P_{h4r}	40	P_{s4z}	0	P_{s4r}	40

The original geometry is created on the 3-D modelling software by using the optical scanning output data. The other geometries are obtained by using the Bezier and camber line formation equations. Then, the resulting points are imported in Unigraphics NX software and manipulated. Equations 2.1 to 2.11 are used to calculate the camber line point coordinates in a MS Excel sheet. The points generated by the Excel are imported into UGS NX software by means of the “Import” function. Finally, the 3-D hub and shroud camber lines are formed within the software. The remaining processes are the same as explained in Section 3.3.

CHAPTER 4

PARAMETERIZATION & DESIGN OF EXPERIMENTS METHODOLOGY

4.1 Design Parameters

The parameters in the definition of a centrifugal impeller geometry are defined and listed in section 3.4. However, all the parameters listed are not used in the optimization study of the existing model. There are some constraints on the geometry such that the number of the parameters listed is reduced.

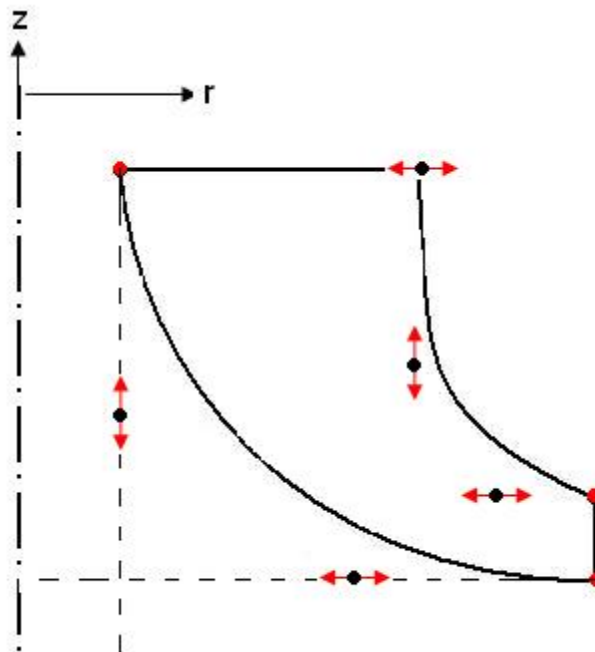


Figure 28 Constraints on Meridional Section

As stated in Section 3.4, dr/dz at the inlet of hub and shroud curves and dz/dr at the exit of the curves should be zero for structural and manufacturing concerns. Therefore, all the Bezier control points shown in Figure 28 with red arrows only move in one direction. As a characteristic of the Bezier curves, the first two and the last two control points define the slopes at the beginning and at the end of the Bezier curves. As a result, the control points must be situated on the same horizontal or vertical axis.

The diffuser section beginning at the end of the meridional section is not studied within this thesis work. Therefore, the dimensions of diffuser are kept constant. As a result, the two control points at the end of the meridional section are fixed.

As a result, the meridional section has 5 parameters to be examined through optimization study. Other important parameters to be included in optimization process are blade angles, splitter cut-off ratios and the number of blades.

Through the optimization study, the parameters are evaluated at certain intervals due to some geometrical and physical constraints. For some values of the parameters the blade geometry can be corrupted such that no flow can pass through these blades. Moreover, for some intervals the geometry can have shape such that its manufacturing might be impossible with known manufacturing techniques. Therefore, the intervals of interest are chosen regarding these consequences. The parameters to be studied within this thesis study and their ranges to be included for experimental design are given in Table 4. Table 4 contains all the continuous parameters with their ranges. Only discrete parameter is the number of blades, N .

Table 4 Continuous Parameters List

Parameters	Range
COR_h	0.15-0.3
COR_s	0.3-0.5
H2Z	5-25 mm
H3R	15-30 mm
S2Z	10-25 mm
S3R	30-35 mm
S1R	30-35 mm
β_{ih}	30°-50°
β_{is}	40°-70°
β_{eh}	0°-30°
β_{es}	0°-30°

Table 4 provides 11 continuous parameters to define the geometry. In addition to these parameters, number of blades, N , is another parameter to be examined. N is not a continuous parameter and defined discretely which can take the values 6, 7 and 8.

The splitter parameters COR_h and COR_s ranges are chosen according to physical constraints of the geometry. For other values out of the specified ranges, the geometry of the splitters deteriorate.

4.2 Design of Experiments

Once the design variables (parameters) are selected, the designer's task is to generate the alternative configurations that are to be used as basis of the optimization process. Since these base configurations created by using the design of experiments methodology will be used to construct the so called analytical functions representing the relation between the pressure ratio of the compressor and the input parameters, the number of configurations used will increase the accuracy of the models. However, as the number of configurations increase, it will give rise to the computational time which is an undesirable case. As a result, an intelligent scheme is needed for selecting the base configurations which will yield a reliable relation between the inputs and the output.

The optimization study is to be carried out for 12 parameters. Use of full factorial design means including all the factor-level combinations which results in a huge design space, namely many number of experiments to carry out. Therefore, a methodology is to be followed to decrease the number of design points. By doing this, a suitable optimization method is to be chosen accordingly for accurate prediction of the optimum.

The classical design of experiment techniques like full or fractional factorial designs, orthogonal arrays or face centered cubic designs provide too many design points. Although the fractional factorial designs provide less configurations with respect to a full factorial design, again the number of designs can exceed the limit set by the designer. Moreover, the designer is restricted to divide the interval of the parameter value into small pieces. The resulting design points are important, while the intervals between these points are disregarded. However, the modern approaches for design of experiments try to optimize the design space such that the resulting space compensates the overall effects well.

The modern design of experiments methodologies are more applicable for the purpose of this thesis study. I-optimal and D-optimal designs are the most common modern approaches for the design of experiments. Between I and D-optimal designs, I-optimal is more appropriate for this study. I-optimal design generates the design space such that the average variance is minimized. Therefore, I-optimal design is the best method for the accurate prediction of the response. However, D-optimal study is generally selected when the effects of parameters are needed to be deeply investigated.

I-optimal methodology tries to minimize the average variance of prediction over the region of the data.

$$I = \frac{n}{\sigma^2} \int \text{var } y(x) d\mu(x) \quad (4.1)$$

Use of I-optimal design is more appropriate when your objective is to determine optimal operating configurations, and also is appropriate to determine regions in the design space where the response falls within an acceptable range; or, to develop feedback-control models.

The number of design points are determined according to the desired degree of interaction between the input parameters. In this study, up to second order interaction of input parameters is included. The next step after design of experiments study is to fit a function between the input parameters and the output such that the output is handled as a result of multiplying single and joint effects of input parameters with weights which are calculated by some regression analyses through function fit studies. As a result of 12 parameters, the function to be fitted will have 12 first order terms defining single parameter effects. The joint effects of two parameters are formed by taking any two parameter combinations out of 12 parameters which

results in 66 combinations. Moreover, there are 12 second order effects of single parameters. As a result, the function to be fitted will have 90 terms with unknown weights. Within this thesis study, the joint effects of parameters COR_h and COR_s with β_{ih} , β_{is} , β_{eh} , β_{es} and N are excluded, since their joint effects are expected to be small. Therefore, 10 terms out of 90 terms are excluded from the function. Finally, a common approach in design of experiments study is to add a so called “center point” which is a point centered in the overall design space. As a result, 81 design points are needed for function fitting and optimization studies.

According to I-optimal design, the design space is generated by using the pre-defined 11 continuous parameters and a discrete parameter N . The design space is provided in Appendix A. There exist 81 design points to be experimented through the CFD analyses. As a result, an optimization process will be carried out by fitting the response (pressure ratio) obtained from 81 CFD runs to the input parameters. Then an optimization algorithm will be applied on the relation between the inputs and the output, and an optimum geometry configuration will be obtained.

The design space generated by the I-optimal design of experiments methodology can be interpreted by 3-D scatter plots including the parameters of interest. Several 3-D scatter plots can be obtained by choosing three parameters of interest. Triple combinations of 12 parameters can be interpreted separately. The triple combinations of 12 parameters make 220 different combinations. Therefore, only a few sample 3-D design spaces will be shown as in Figure 29, Figure 30 and Figure 31.

The success of the design of experiments methodology can be predicted by checking the even point distributions. Figure 29, Figure 30 and Figure 31 show that there is an even distribution of the points. In Figure 31, all the points are distributed evenly without any loss of points. However, although the even distribution exists for Figure 29 and Figure 30, some points are not included in the design space.

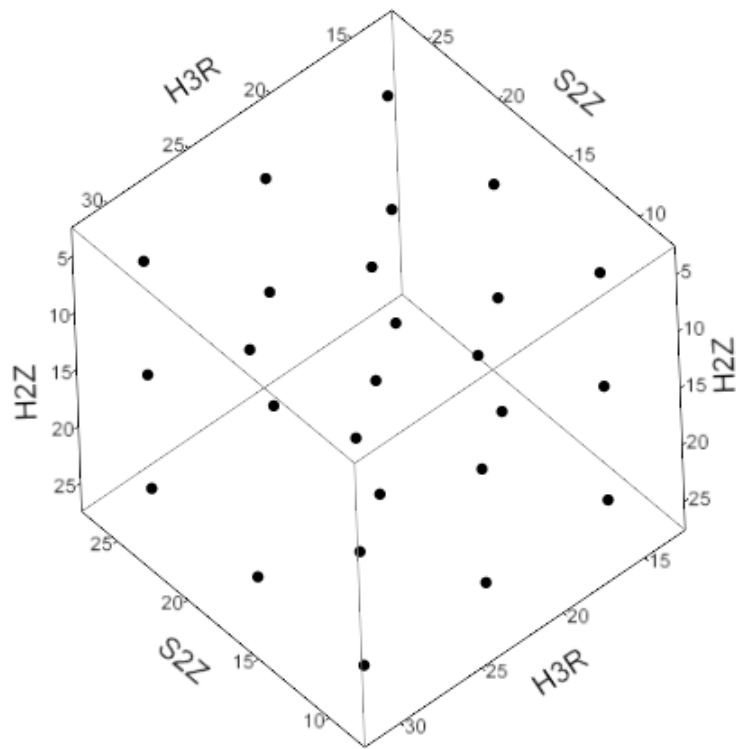


Figure 29 Design Space for H2Z, H3R and S2Z

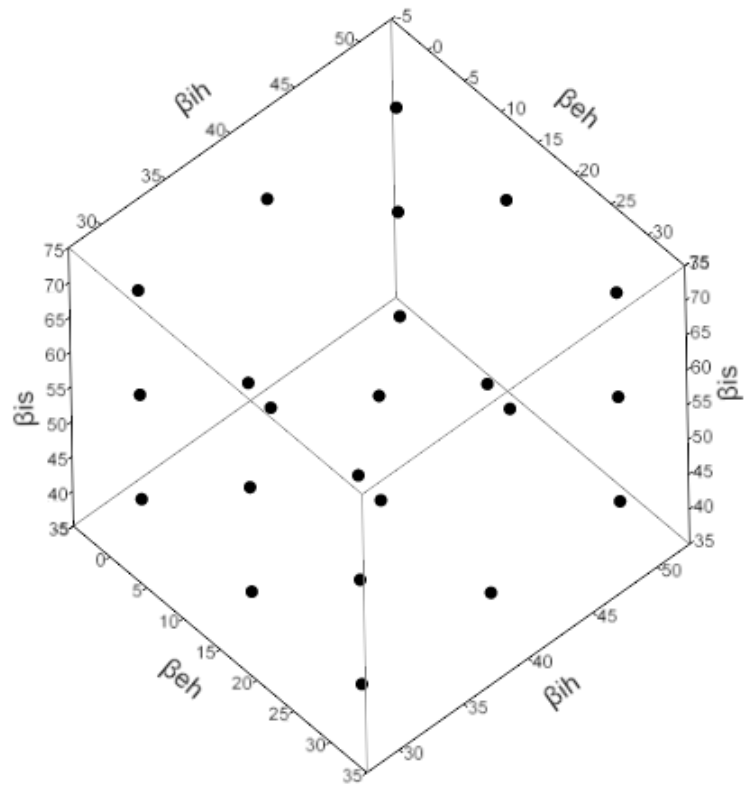


Figure 30 Design Space for β_{ih} , β_{is} , β_{eh}

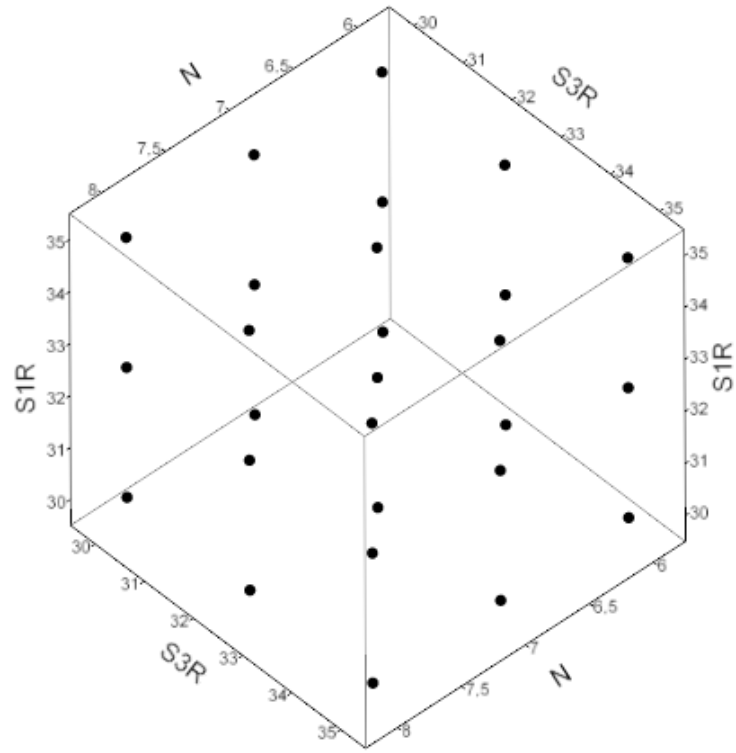


Figure 31 Design Space for S1R, S3R and N

CHAPTER 5

COMPUTATIONAL FLUID DYNAMICS ANALYSES

Computational fluid dynamics (CFD) is today's most challenging and practically the most useful branch of fluid mechanics in which numerical methods are used to analyse the problems related with the fluid flow. In this chapter, the CFD analyses of the centrifugal compressor is carried out in order to obtain the system's response to the changes in parameters. All the 81 designs obtained by the design of experiments study are analysed and the results are discussed in this chapter.

All the necessary CFD analyses are done by using the FLUENT [47] software. Any boundary conditions and equations required to solve the flow through the centrifugal compressor are implemented on the software. The grid generation is carried out in GAMBIT [48] software which is needed for the finite element CFD analyses.

The results of the CFD analyses will be used to create a response fit through the inputs and the pressure ratio as an output. The repeatability of the computational fluid dynamics analyses and absence of random errors make the optimization process more reliable. The computational analyses do not contain any interferences to the system like laboratory experiments. In laboratory experiments, the environmental conditions are not controlled which produces random errors. However, computational analyses have controlled boundary conditions which lets the designer to follow up the optimization process without random errors.

5.1 CFD Analysis Assumptions

For many flows in a turbomachinery, simplifications to the Navier-Stokes equations are applicable. Solving Navier-Stokes equations with all the terms included results in a rise in the computational time needed for the analysis. Therefore, it is not efficient to solve the Navier-Stokes equations for all flow fields within a turbomachinery. The technique to be employed for the computation of a flow field in a turbomachinery depends on the geometry and the flow regime.

The case to be studied is a 3-D, compressible ideal gas flow. The main purpose of the computational fluid dynamics analyses to be done within this study is to obtain the pressure distribution within the compressor. Use of Navier-Stokes equations provide the most accurate solution for the flow field. However, by taking the purpose of the study and the time required for analyses into consideration, the solutions are obtained by using the Euler (inviscid) equations which reduces the time required for the analyses significantly and make reliable predictions for the flow in the compressor.

Japikse [2] compared the use of Euler and Navier-Stokes equations for a radial turbine and shows that the results are remarkably similar. The overall pattern of the Navier-Stokes solutions are very similar to Euler solutions, but the viscous terms in Navier-Stokes case reduce the momentum of the fluid which results in some pressure drop. Moreover, Lakshminarayana [45] supports the use of Euler equations where pressure distributions is of main interest.

Since the aim of the study is to maximize the pressure ratio generated by the compressor, the Euler equations can predict the response of the compressor to the geometry changes. By using the Euler equation solutions, a designer is able to gauge the results and obtain a deeper understanding of the fluid flow by inference from the results. The underlying trends in the relation between machine geometry and the resulting aerodynamic behaviour can be easily discovered.

Using Euler equations reduce the computational time significantly, since the Euler equations are simpler form of Navier-Stokes equations. In addition to simplicity, the finite element grids needed for the solution of Euler equations can be coarser compared to the grids generated for viscous Navier-Stokes analysis. This situation also reduces the time required for the computational analysis.

Within this thesis study, the pressure ratio at the maximum angular velocity of the engine is to be maximized. Therefore, the solutions are obtained only for the maximum speed condition. A steady state analysis will be carried out and the flow is assumed to be adiabatic.

The case to be studied is a system which consists of a rotary impeller surrounded by a stationary diffuser. Therefore, a multiple reference frame (MRF) model will be used through the CFD analyses. At the interfaces between the rotating and stationary zones, appropriate transformations of the velocity vector and velocity gradients are performed to compute fluxes of mass, momentum, energy, and other scalars. The flow is assumed to be steady in each zone. MRF ignores the relative motions of the zones with respect to each other.

For rotating systems, it is necessary to describe the flow behaviour relatively to a rotating frame of reference. For the compressor rotating steadily with an angular velocity of $\vec{\omega}$, the velocity of fluid particle is given as:

$$\vec{v} = \vec{w} + \vec{\omega} \times \vec{r} \quad (5.1)$$

where \vec{w} is the velocity vector relative to the rotating system. Therefore, the conservation of mass equation for steady state case can be given as:

$$\nabla \cdot (\rho \vec{w}) = 0 \quad (5.2)$$

Two forces must be added in the rotating frame of reference which are Coriolis force per unit mass (\vec{f}_{cor}) and the centrifugal force per unit mass (\vec{f}_c).

$$\vec{f}_{cor} = -2(\vec{\omega} \times \vec{w}) \quad (5.3)$$

$$\vec{f}_c = -\vec{\omega} \times (\vec{\omega} \times \vec{r}) \quad (5.4)$$

Therefore, the conservation of momentum equation for steady and inviscid flow becomes:

$$\nabla \cdot (\rho \vec{w} \otimes \vec{w}) = \rho \vec{f}_e - \rho \vec{\omega} \times (\vec{\omega} \times \vec{r}) - 2\rho(\vec{\omega} \times \vec{w}) - \nabla p \quad (5.5)$$

The conservation of energy equation for steady, adiabatic and inviscid flow can be given as:

$$\nabla \cdot \left[\rho \vec{w} \left(h + \frac{\vec{w}^2}{2} - \frac{\vec{u}^2}{2} \right) \right] = W_f \quad (5.6)$$

where $\vec{u} = \vec{\omega} \times \vec{r}$, and W_f is the work done by the external forces in the relative system which is defined as:

$$W_f = \rho \vec{f}_e \cdot \vec{w} \quad (5.7)$$

The system of Navier-Stokes equations is supplemented by the equation of state for a perfect gas which is given as:

$$p = \rho RT \quad (5.8)$$

In equation 5.8, R is the gas constant per unit of mass, or namely the universal gas constant divided by the molecular weight of the fluid.

For calorifically perfect gases, the enthalpy is only a function of temperature which is defined as:

$$h = c_p T = \frac{\gamma}{\gamma-1} \frac{p}{\rho} \quad (5.9)$$

where c_p is the specific heat for constant pressure and γ is the specific heat ratio of the fluid.

5.2 CFD Solutions

The computational fluid dynamics analyses are done by using the FLUENT software, while the grid (mesh) generation is carried out with the GAMBIT software throughout the thesis study. The FLUENT software iterates on the grids generated by the GAMBIT software by using the necessary equations for the flow indicated by the user. Therefore, the grids and the solver options (equations, boundary conditions and constraints) must be compatible with each other.

The grid size is an important factor in CFD analyses. Finer grids result in more accurate results, but it gives a rise to total computational time used in CFD analyses. Coarser grids provide less accurate results, but the computational time needed for the analyses is less. Therefore, an income-outcome analysis can be conducted to decide on the grid size considering the predicting capability and the computational time.

The first CFD analysis is done for the original centrifugal compressor geometry. In order to check the effect of grid size on the solution, a grid size convergence study is preferred. Grids with 10,000, 150,000, 300,000 and 600,000 number of elements are studied. Since the geometry of the compressor consists of repeating blade sections, only a portion of the full geometry representing the overall characteristics is chosen. Therefore, the grid size is reduced and as a result the time required for the CFD analysis is reduced.

The original diffuser geometry is not parametrically studied and optimized within this study. The diffuser must be chosen as a part of another optimization study following the studies regarding the blade geometry optimization. Therefore, the diffuser geometry is not included in the CFD analyses. A vaneless diffuser section is provided at the end of blade section in order to see the flow characteristics at the exit of the blades and to let the flow settle down in the diffuser section.

A *tetrahedral mesh* is used throughout the volume within the blades, while *hexahedral mesh* is used for the diffuser section. The grids having 10,000 and 600,000 elements are given in Figure 32 and Figure 33 respectively.

After grid generation, some boundaries are defined in the GAMBIT software. In Figure 32 and Figure 33, the surface with dark blue colour is the inlet surface which is defined as “mass flow inlet” boundary. The black coloured faces are solid boundaries defined as “wall” boundaries. The red surface is the flow exit surface defined as a “pressure outlet” boundary. The light blue surfaces denote the “periodic boundaries” which defines the periodicity of the portion.

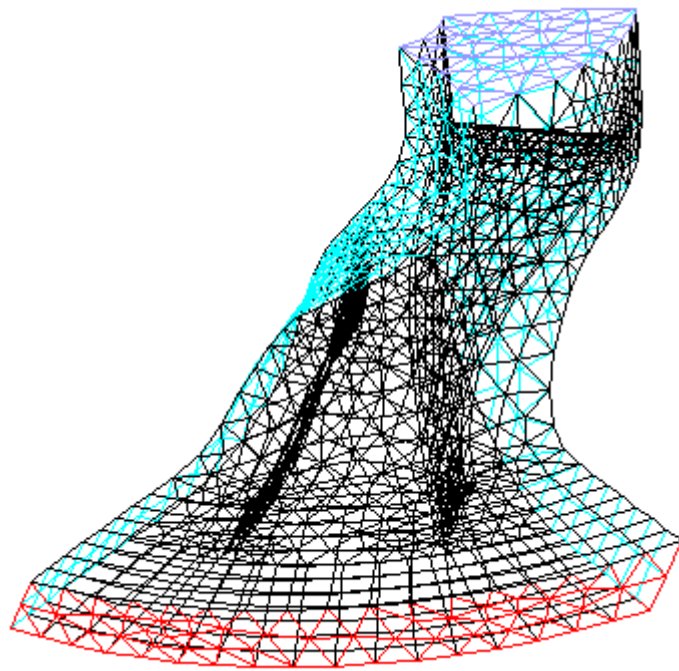


Figure 32 Coarse Grid with 10,000 Elements

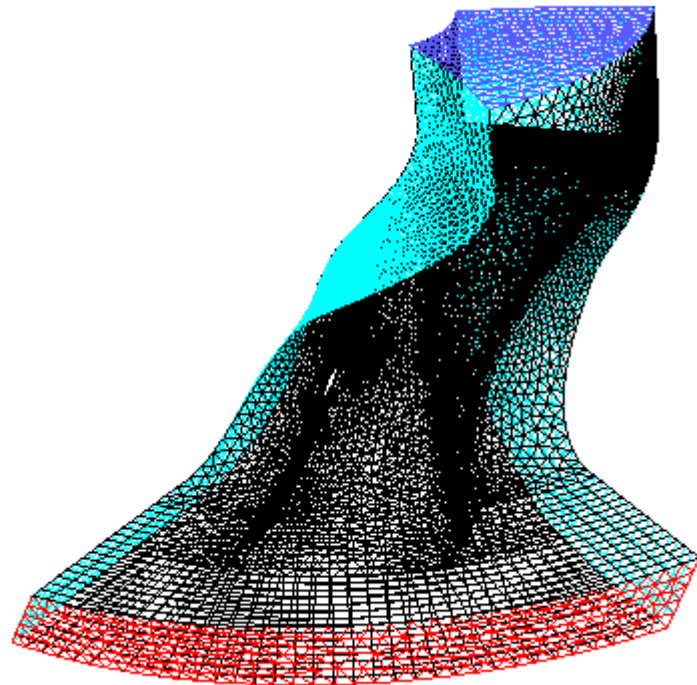


Figure 33 Fine Grid with 600,000 Elements

The computational fluid dynamics analyses can be done after an effective grid generation and boundary settings. The mass flow rate and the rotational speed of the compressor are given as an input to the FLUENT software. The rotational speed of the compressor is 112,000 rpm and the mass flow rate is 0.45 kg/s. Since one sixth of the total geometry is analysed, the mass flow rate is taken as one sixth of the total mass flow rate.

The blades of the compressor are rotating while the diffuser is stationary. Therefore, a scheme to be applied for the volume between the blades and the diffuser volume in order to match the grids of adjacent volumes. The “moving reference frame” scheme is applied to the rotary volume to simulate the rotation of the blades in steady state.

For complex flow problems, the flow convergence can be accelerated if a better initial solution is used at the start of the calculation. The Full Multigrid (FMG) initialization command of FLUENT is used to provide this initial and approximate solution at a minimum cost to the overall computational expense.

An iterative process is followed during the CFD analyses. The static pressure value in the “pressure outlet” boundary is changed until the total pressure at the inlet reaches 101.3 kPa. Then, the area-weighted average of the total pressure at the exit is calculated and divided by 101.3 kPa to find the pressure ratio of the compressor.

The pressure ratios obtained by the CFD analyses for the original geometry is listed in Table 5. The total pressure contours for the coarse and fine meshes are given in Figure 34 and Figure 35 respectively.

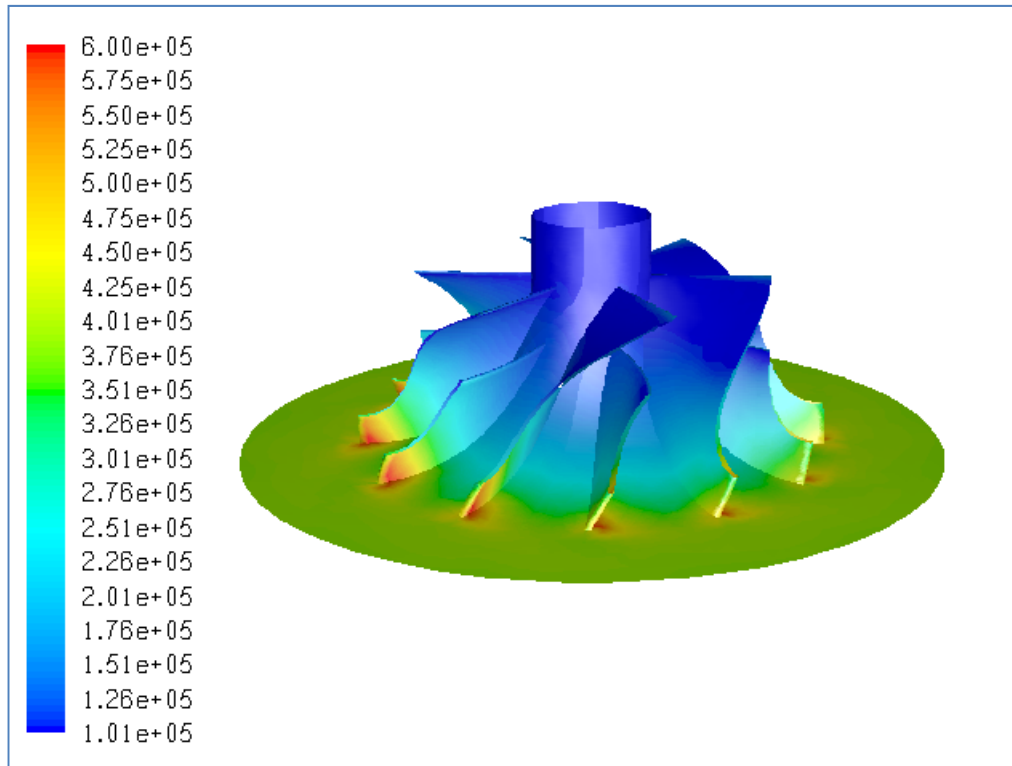


Figure 34 Total Pressure Distribution (in Pa) (10,000 elements)

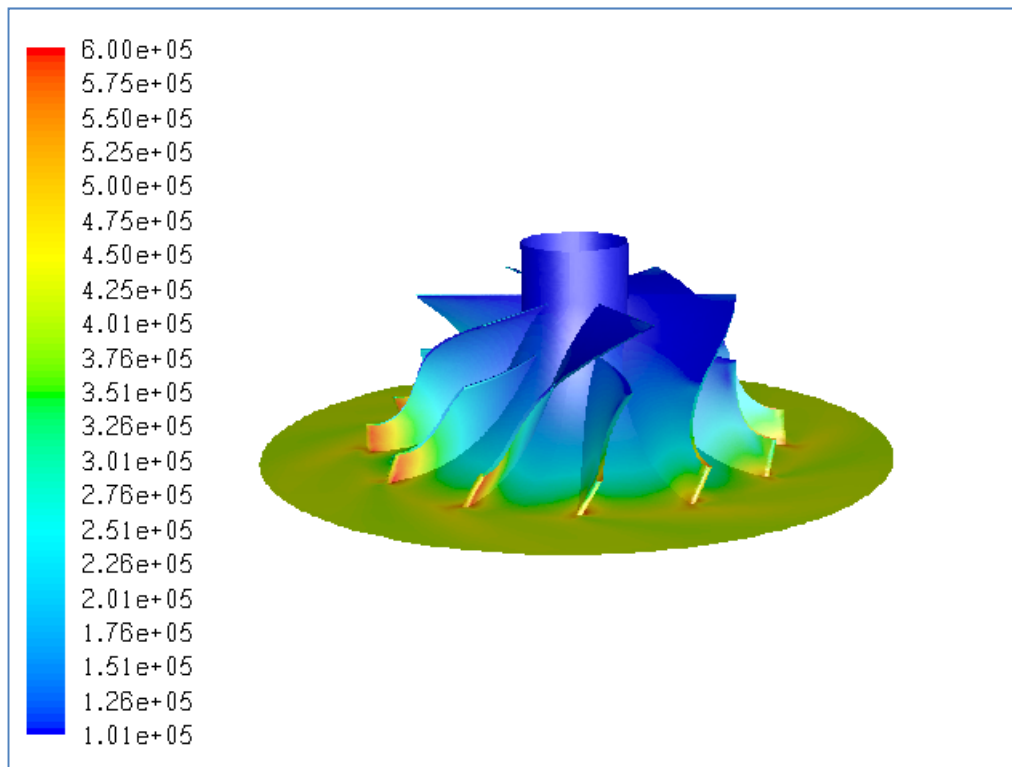


Figure 35 Total Pressure Distribution (in Pa) (600,000 elements)

Table 5 Grid Convergence

Grid Size	Pressure Ratio
10,000 elements	3.68
150,000 elements	3.77
300,000 elements	3.85
600,000 elements	3.90

As can be seen in Figure 34 and Figure 35, the flow characteristics for fine and coarse meshes are very similar. The pressure increases as flow proceeds downstream and has its highest value at the pressure surface of the blades on the trailing edge corner. After getting into the diffuser section, the flow settles down and gets more uniform.

When the grid convergence table is examined, the result of the coarse mesh is only 5.6% less than the result of the fine mesh. Moreover, the flow patterns are similar, too. Therefore, the coarse mesh (10,000 elements) can be used to analyse all the 81 designs. This approach will reduce the time needed for the computational analyses.

When all the 81 analyses are carried out there exists both superior and worse cases with respect to the original case. There are cases where higher pressure ratios are obtained, but, for some cases, the flow is choked and cannot operate for the given mass flow rates. The design case number 4 in Table A.1 provides the highest pressure ratio. For case #4, the number of blades is increased to 8 and the inlet diameter does not change when compared to original geometry. However, the Bezier curves of the meridional view provide a wider area of flow throughout the domain. These changes in geometry are the important factors in obtaining a higher pressure ratio.

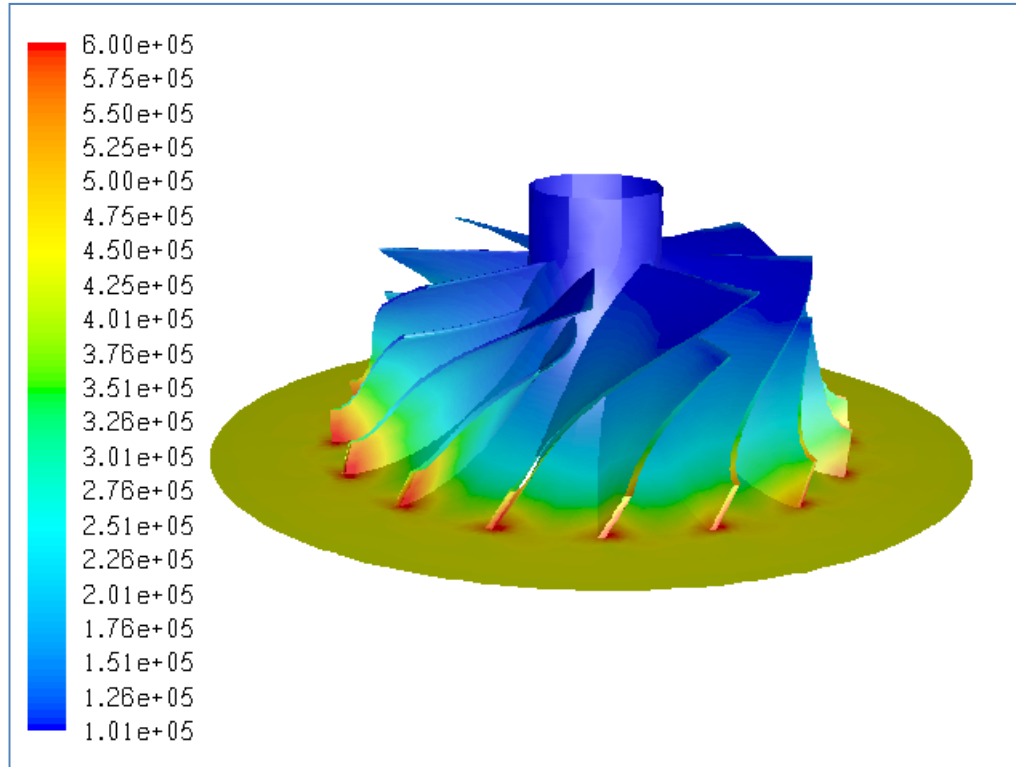


Figure 36 Total Pressure Distribution (in Pa) for Case #4

For some cases, the flow area is reduced such that the flow is choked and the compressor no more operates. These designs will be excluded from the optimization studies. The design case number 6 is an example to such geometries. For such cases, the flow cannot be forced downstream as can be seen in Figure 37. The mass flow rate should be reduced significantly for these geometries to operate, but this is not the case desired in this optimization study.

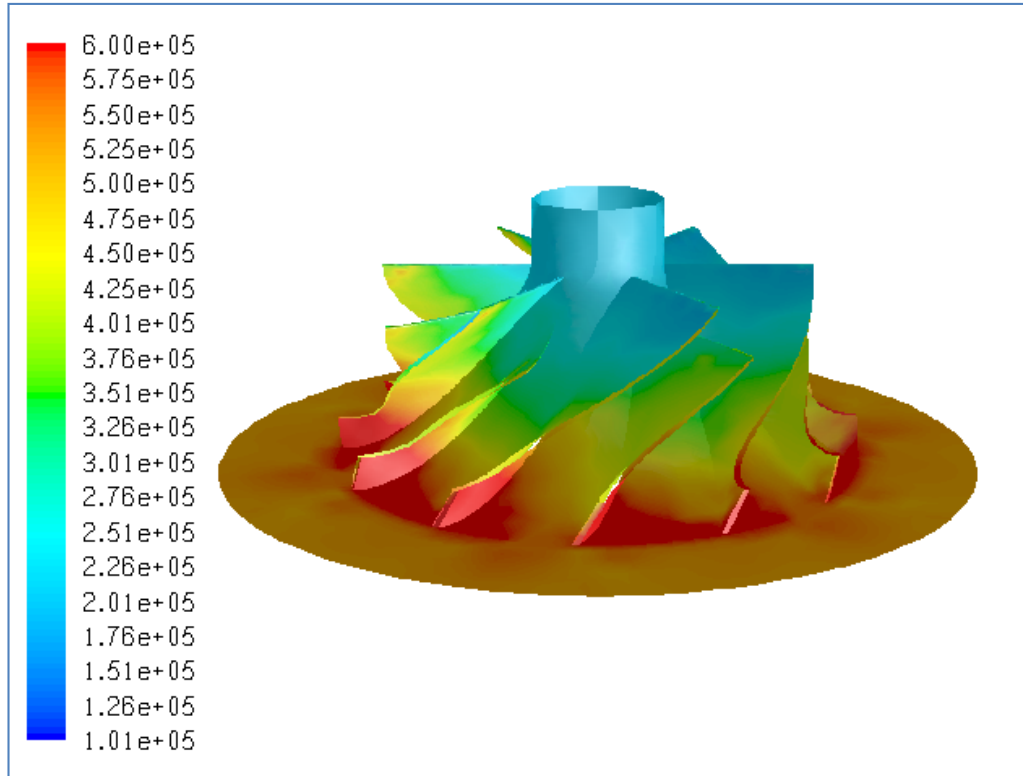


Figure 37 Total Pressure Distribution (in Pa) for Case #6

All the pressure ratio results of the CFD analyses are tabulated in Appendix A with corresponding geometries and all the total pressure distributions (coarse grid) for all cases are presented in Appendix B. The optimum geometry configuration will be obtained in the next chapter and its CFD results and comparisons with the original geometry will be provided within that chapter.

CHAPTER 6

ARTIFICIAL NEURAL NETWORK FIT & OPTIMIZATION

The last stage of this thesis study is to define the relation between the input parameters and the pressure ratios found as a result of CFD studies and then apply a suitable optimization algorithm in order to seek for the optimum configuration.

6.1 Artificial Neural Network

Artificial neural networks are known as learning methods which provide robust approaches to approximate an objective function and used preferably for modelling non-linear systems. Especially, Artificial neural networks is preferred for systems with unknown or unpredictable behaviour. Artificial neurons consist of a unit that sums the inputs with some specified weights, a threshold, an activation function, and an output. There are many activation functions used in Neural Networks. The most commonly used activation functions is the S-shaped sigmoid function. A neural network is just a set of nonlinear equations that predict output variables from input variables in a flexible way using layers of linear regressions and S-shaped functions.

$$S(x) = \frac{1}{1+e^{-x}} \quad (6.1)$$

Artificial neural networks are composed of layers of neurons connected to other neurons on the neighbouring layer. Between the input and output layer, there is a hidden layer of neurons where the relation between the input and the output is defined as shown in Figure 38.

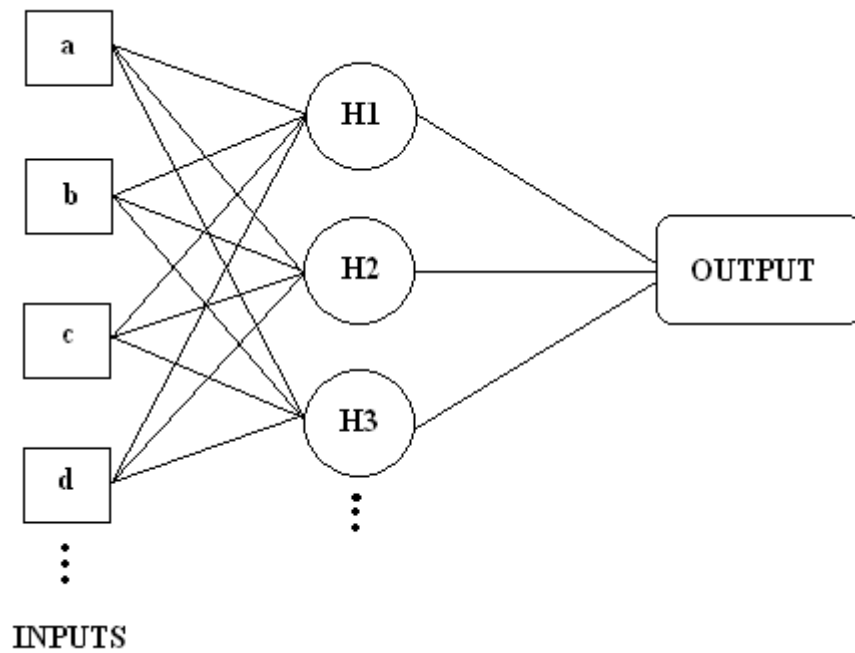


Figure 38 Sample Neural Network with 3 Hidden Nodes

Number of nodes to include for the hidden layer is to be decided upon an iterative process by considering the r-square and cross-validation r-square values of the neural network fit. R-square values give opinion about the quality fit with respect to the actual data. Cross-validation r-square value is obtained by self-checking of the algorithm with some holdback samples.

Although artificial neural networks are preferable for the modelling of non-linear systems, they maintain a risk of over-fitting, namely fitting a model with too many parameters. The over-fitting problem can be avoided by selecting high cross-validation r-square valued fits. However, a cross check of the r-square value must be made in order to see the quality of the fit. As a result, there might be several neural network fits for a dataset each having different hidden node numbers, r-squares and CV r-squares, but the one with high CV r-square and r-square values should be chosen.

The necessity to optimize the number of nodes makes the training of neural networks an iterative process. Therefore, indications for goodness of fit and over-fitting are required. K-fold cross validation method can be used to obtain cross validation r-square so that over-fitting can also be inspected during the fitting process.

In this thesis study all the neural network fit studies are carried out with SAS JMP [49] software. The optimum configuration given by the software is run into the CFD analysis and the results provided by the optimization algorithm and CFD analyses are compared. If there is an unacceptable difference between the results, the optimum configuration is added to the design space as an additional point and another neural network fit is applied on the new design space. This process is iteratively continues till the results converge.

The JMP software uses the Simplex algorithm to find the maximum of a function generated by the artificial neural network fit. The optimization process starts with an initial design of $n+1$ trials where n is the number of parameters. The resulting n -dimensional space is called a simplex. For a single parameter the shape of the simplex is a line, while for two parameters it is a triangle (Figure 39) and for three parameters it is a tetrahedron. For 12 parameters, a 12-dimensional polyhedron simplex is formed by 13 trial points which is difficult to interpret. After the generation of simplex shape, the first rule is to reject the trial with the least favourable response value in the current simplex. A new set of control variable levels is calculated by reflecting the least favourable result to the opposite side. At each step, the least favourable conditions are rejected and more favourable results are held. During this procedure another important rule is not to return to parameters that have just been rejected.

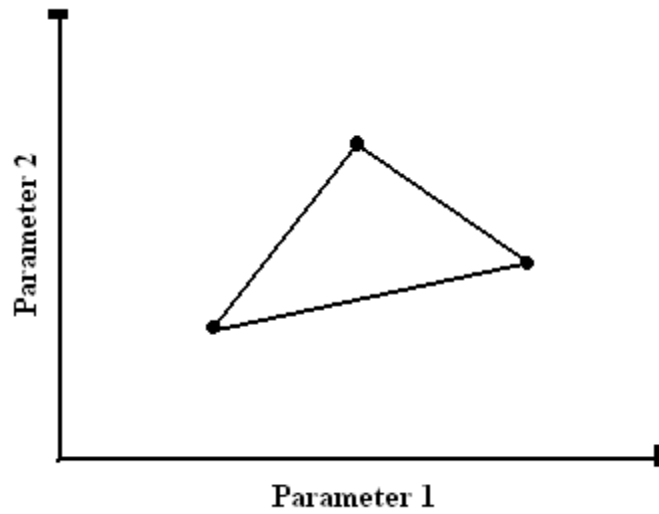


Figure 39 Triangular Simplex

The iterations followed through the neural network fit and optimization studies are listed in Table 6. In addition to 81 designs generated by the design of experiments study, additional 12 designs are analyzed to reach the optimum geometry configuration.

The last Neural Network fit is done at the end of 11th iteration. The Neural Network structure obtained has 4 hidden nodes and fit has a r-square value of 0.99518 and cross validation r-square of 0.81161 which are quite acceptable. The structure of the Neural Network is given in Figure 40. The actual pressure ratio versus the predicted pressure ratio is plotted in Figure 41.

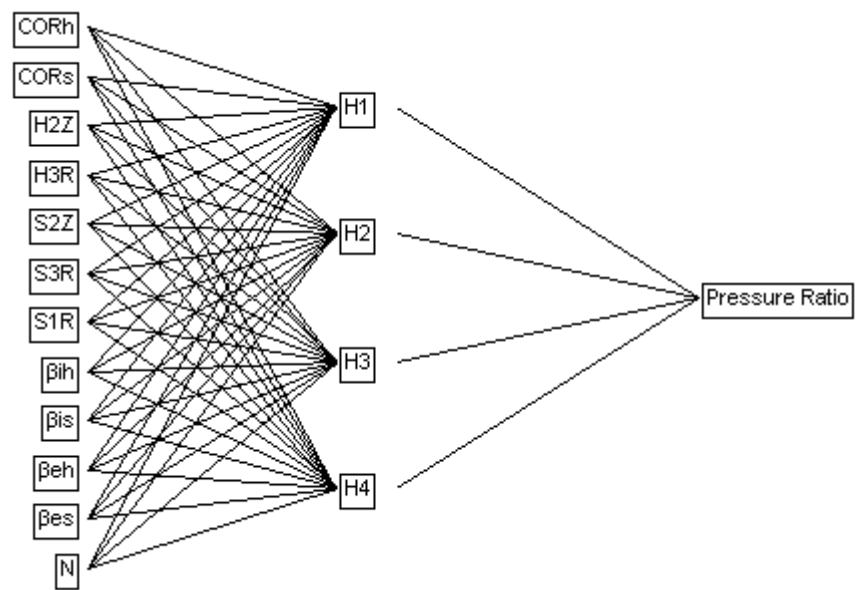


Figure 40 Neural Network Structure with 4 Hidden Nodes

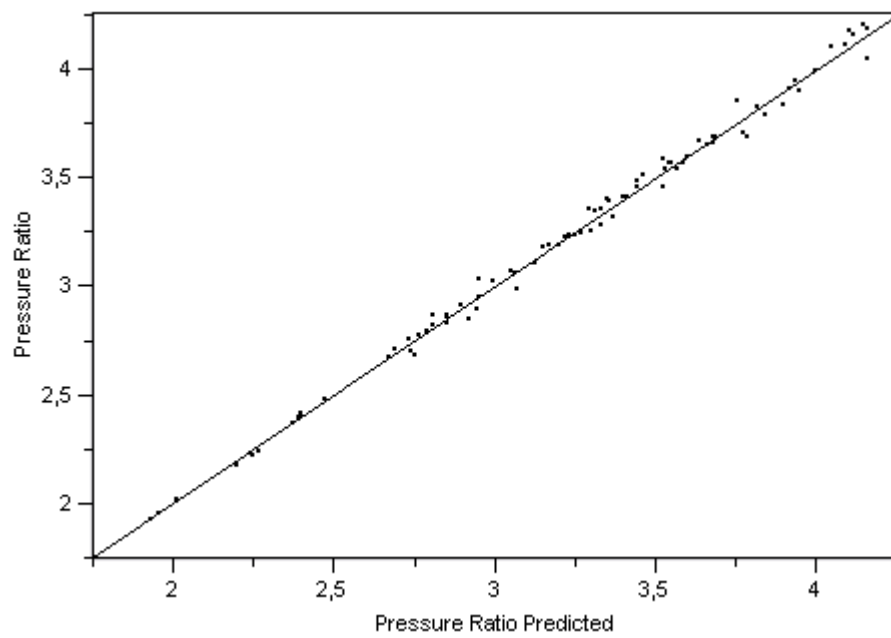


Figure 41 Actual Pressure Ratio vs Predicted Pressure Ratio

The CFD analyses of the optimum geometry is carried out on both the coarse and fine meshes. The pressure ratio for the coarse mesh case is obtained as 4.2119, while it is 4.6128 for the fine mesh case. In the design space generated by the design of experiments stage, the 4th design produced the highest pressure ratio. This case is also solved with a fine mesh and the pressure ratio is calculated as 4.5310 which is again less than the optimum geometry pressure ratio.

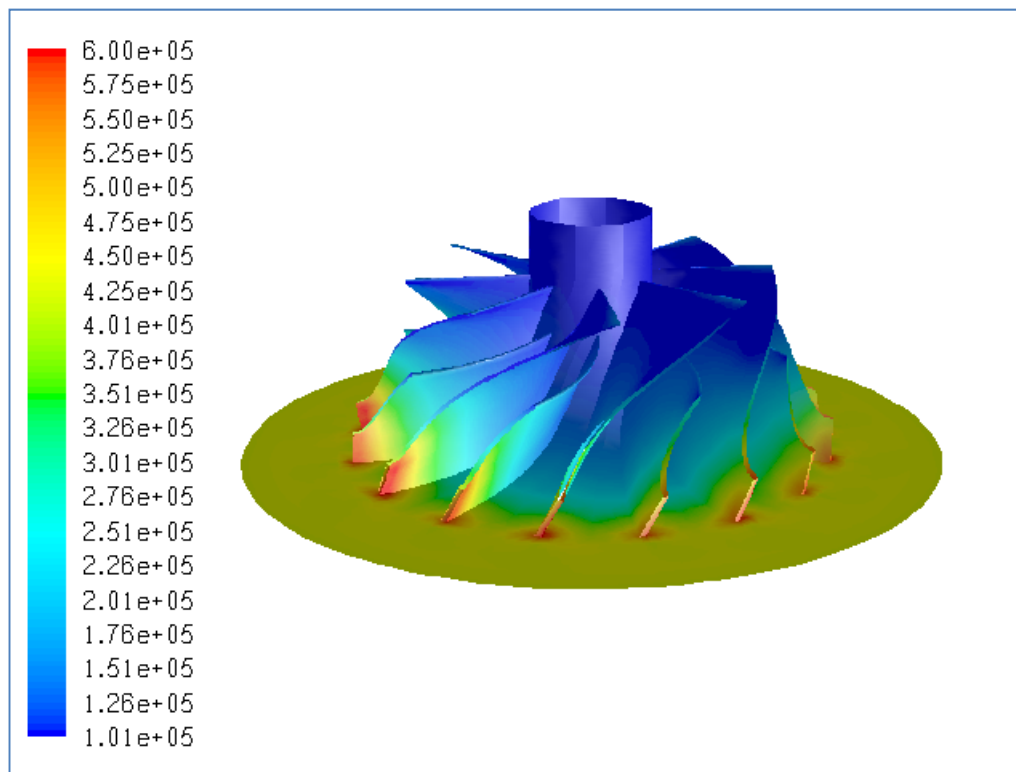


Figure 42 Optimum Geometry Pressure Distribution (in Pa) (10,000 elements)

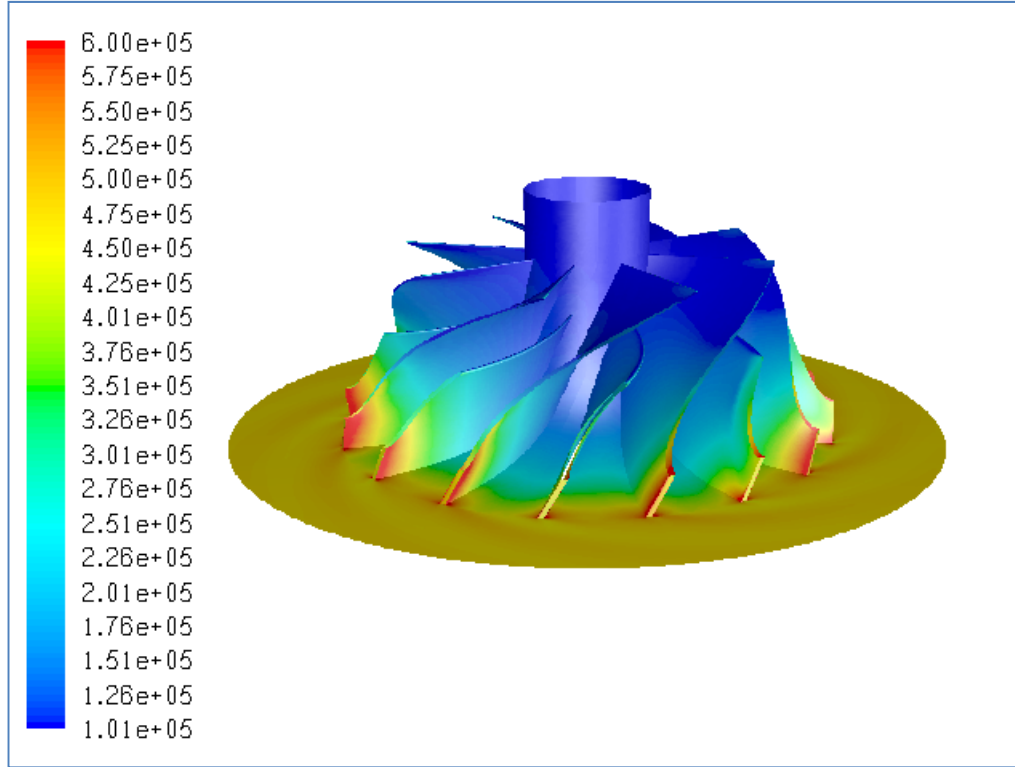


Figure 43 Optimum Geometry Pressure Distribution (in Pa) (600,000 elements)

When compared to the original geometry, the optimum compressor geometry has an increased number of blades which has a positive effect on pressure increase. The blade angles at the exit are 0° . Therefore, the blades are called as radial blades. The original geometry has back-swept blades. As it is the case in the literature, for fixed mass flow rate, the radial blades provide higher pressure ratios and this is proven within this thesis study. The splitters for the optimum geometry is longer in hub and shorter in shroud with respect to original geometry splitters. The pressure ratio produced by the optimum geometry is calculated as 4.2119 for the coarse mesh case, while it is 3.6834 for the original geometry. As a result, there is a 16% increase in the pressure ratio for the optimal design. Considering the fine mesh results, the optimum geometry provides a pressure ratio of 4.6128, while it is 3.9018 for the original geometry. Therefore, there is a 18% increase in pressure ratio for the fine mesh case.

Table 6 Iterative Neural Network Studies

Iteration	CORh	CORs	H2Z	H3R	S2Z	S3R	S1R	β_{ih}	β_{is}	β_{eh}	β_{es}	N	Predicted Pressure Ratio	Pressure Ratio (CFD)
1	0.15	0.5	5	26.5	25	30	30	30	70	30	30	8	4.5987	3.5639
2	0.15	0.3	5.51	28.13	10.2	35	31.43	41.65	69.67	0	4.77	6	4.4301	3.895
3	0.2	0.5	5	15.07	25	35	30	31.59	70	0	0	8	4.4154	4.0503
4	0.15	0.3	5	15	12.1	35	30.12	30	70	0	0	7	4.3577	4.1026
5	0.3	0.33	14.59	30	25	35	30	50	70	0	0	8	4.3201	2.9870
6	0.23	0.3	25	15	25	35	30	30	70	0	2.34	8	4.3105	4.1157
7	0.3	0.5	10.55	15	25	35	30	50	70	0	30	8	4.3059	3.2391
8	0.15	0.34	5	15	25	35	30	30	70	0	0	8	4.3041	4.2015
9	0.3	0.42	25	15	21.59	35	30	30	70	0	0	6	4.2997	3.9929
10	0.3	0.5	19.59	15	25	35	30	30	70	0	0	8	4.2875	4.1793
11	0.3	0.3	11.82	15.28	25	35	30	33.25	70	0	0	8	4.2517	4.1829
12	0.15	0.45	5.22	14.8	25	35	30	31.2	70	0	0	8	4.2007	4.2119

CHAPTER 7

CONCLUSION and FUTURE WORK

7.1 General

The optimization of a centrifugal compressor is a complex study involving 3-D parametric geometry generation, mesh generation and computational fluid dynamics analyses. Since the geometry of the centrifugal compressor impeller is defined by many parameters, many CFD runs are needed to be done by trying several combinations of parameters. Therefore, a huge computational effort and analysis time are needed to accomplish the optimization task. In the course of this study, a statistical methodology is adapted to the process in order to reduce computational effort and time needed for the analyses.

The optimization study is implemented on an existing centrifugal compressor of a small turbojet engine. Firstly, the geometry of the compressor is obtained by using an optical scanner with better accuracy compared to other reverse engineering techniques. Then, the obtained geometry is processed in UGS NX software and the original geometric model is created within that software. All the necessary measurements are done on the model and the values of the parameters that define the impeller are provided.

In order to carry on with the optimization study, the geometric parameters to be examined are determined. Due to some restrictions (constraints) on the geometry, all the parameters defined for the original geometry cannot be used. As a result, some of

the parameters are fixed and the rest are defined in an interval in order to form a design space for design of experiments study.

The design of experiments methodology is the heart of this thesis study. Selection of a DOE technique which provides smooth distribution of design points and the technique's conformity with the selected optimization method in an important step for prediction of the optimum. As a result, the I-optimal design method is selected for design space generation. In literature, classical DOE methods are generally chosen. I-optimal is a modern technique which distinguishes this thesis work from other studies. I-optimal design can provide a better design space with fewer number of designs and can help the optimization process to predict the optimum more precisely.

In CFD studies, in case of using Navier-Stokes equations, Euler equations are used to solve the fluid flow within the compressor. Moreover, by following a grid size convergence study, use of a coarse mesh resulted in similar pressure distribution trend with the fine mesh. Therefore, implementing steady state Euler equations on a coarse mesh predicted the flow pattern well and ensured the reduction in computational time.

The relation between the input parameters and the pressure ratio is obtained by means of Artificial Neural Network approach. By applying some iterations on the Neural Network fits supported with an optimization algorithm, an optimum geometry configuration is obtained.

7.2 Discussion and Recommendations for Future Work

With this thesis study, an accelerated and intelligent methodology on the aerodynamic optimization of a small centrifugal compressor is presented. The methodology developed provides a fast prediction of the optimum geometry for maximized pressure ratio at a specified working condition of a small turbojet engine. This methodology can be applied as a preliminary aerodynamic optimization study for any types of turbomachinery. Then, detailed optimization studies including structural, logistical and cost issues can be followed. A computational analysis period which may prolong for months can be easily carried out within a few weeks with reliable results.

A centrifugal compressor design study consists of preliminary cycle analyses and meanline analyses where the general dimensions and stage properties are determined. Then, an optimization procedure is carried out on the preliminary geometry in order to reach the desired optimal configuration. The studies described within this thesis study can be used during optimization stage of centrifugal compressor design.

In addition to aerodynamic issues, the surfaces generated during the geometry generation step are created by taking the machinability concept into consideration. Use of ruled surfaces make the machinability of the compressor impeller surfaces easier with traditional machining approaches.

The assumptions on the CFD analyses simplifies the optimization process significantly. Use of Navier-Stokes equations including the viscous terms would give more accurate results about the flow field within the compressor. However, that would not affect the trend of the flow with changing geometry. The same approach is valid for the mesh sizing. Similar flow characteristics are seen for the coarse and fine meshes with slightly different pressure ratios. A fine mesh provides more accurate

solution clearly, but use of coarse mesh do not affect the trend of pressure distribution with changing geometry.

Within the designs generated by the design of experiments methodology, some of them provided somehow narrower geometries such that the flow is choked at the specified mass flow rate. Therefore, the centrifugal compressor do not operate at this condition and no pressure ratio results can be entered as an output for those geometries. For the I-optimal design to be more successful, all the geometries have to give a result. Since 8 of the points out of 81 design points are choked, more iterations are needed during the Neural Network fit and optimization stage. If there were no choked cases, the number of iterations during the Neural Network fit and optimization stage would be less. The reason is that the parameter configurations resulting in bad geometries could not be introduced to the algorithm in a sense.

The methodology presented in this study can be developed by making some additional works. Firstly, all the geometry generation, meshing, CFD analyses and optimization studies can be done automatically by implementing some user interfaces which will reduce the time required for this study significantly. Moreover, in addition to aerodynamic optimization, structural finite element analyses can be applied by using the pressure distribution around the blades in order to include the structural optimization process into account.

REFERENCES

- [1] Boyce, P.M., *Centrifugal Compressors: A Basic Guide*, Oklahoma, USA, PenWell Corporation, 2003.
- [2] Japikse, D., and Baines, C.N., *Introduction to Turbomachinery*, Vermont, USA, Concepts ETI, Inc., 1997.
- [3] Gorla, R.S., and Khan, A.A., *Turbomachinery Design and Theory*, New York, USA, Marcel Dekker, 2003.
- [4] Bloch, H.P., *Compressors and Modern Process Applications*, John Wiley & Sons Inc, NJ, USA, 2006.
- [5] Sonntag, R., Borgnakke, C., and Van Wylen, G., *Fundamentals of Thermodynamics*, 5th edition, John Wiley & Sons, 1998.
- [6] Ling, J., Wong, K.C., and Armfield, S., *Numerical Investigation of a Small Gas Turbine Compressor*, 16th Australasian Fluid Mechanics Conference, Gold Coast, Australia, 2007.
- [7] Raja, V. and Fernandes, K.J., *Reverse Engineering: An Industrial Perspective*, London: Springer Science, 2007.
- [8] Kathryne, A. Ingle, *Reverse Engineering*, McGraw-Hill, 1996.
- [9] Chen, S., and Wang, W., *Computer Aided Manufacturing Technologies for Centrifugal Compressor Impellers*, Journal of Materials Processing Technology, 115 (284-293), 2001.
- [10] Bell, D.W., *Best Practices: Parametric Design with Hybrid Modelling*, Geomagic, Inc., 2006.
- [11] Bohez, L.J., Pole, K., *A Geometric Modeling and Five-Axis Machining Algorithm for Centrifugal Impellers*, Journal of Manufacturing Systems, vol. 16 no. 6 (422-436), 1997.

- [12] Chivate, P.N., Jablokow, A.G., *Review of Surface Representations and Fitting for reverse Engineering*, Computer Integrated Manufacturing Systems, vol.8 no.3 (193-204), 1995.
- [13] Casey, M.V., *Computational Methods for Preliminary Design and Geometry Definition in Turbomachinery*, AGARD-LS-195, Turbomachinery Design Using CFD, Ohio, USA, 1994.
- [14] Grein, H., Scheebeli, F., and Bantli, H., *Die Modellierung Dreidimensionaler Flächen, ein Werkzeug für Entwicklung und Fertigung Hydraulischer Maschinen*, Technischer Rundschau Sulzer, vol.2, 1989.
- [15] Merryweather, H., Smith, D.J.L., *The Use of Analytic Surfaces for the Design of Centrifugal Impellers by Computer Graphics*, International Journal for Numerical Methods in Engineering, vol.7, pp 137-154, 1973.
- [16] Casey, M.V., *A Computational Geometry for the Blades and Internal Flow Channels of Centrifugal Compressors*, ASME, Journal of Engineering for Power, vol. 105 no.2 (288-295).
- [17] Toker, K.A., *Design and Analysis of Industrial Centrifugal Compressors*, 2000.
- [18] Keskin, A., *Process Integration and Automated Multi-Objective Optimization Supporting Aerodynamic Compressor Design*, 2006.
- [19] Platt, M.J., Marsh, M., *Multidisciplinary Optimization of a LH2 Turbopump Design in an Agile Engineering Environment*, AIAA-2003-4765, Joint Propulsion Conference and Exhibit, Huntsville, Alabama, 2003.
- [20] Benini, E., *Optimal Navier-Stokes Design of Compressor Impellers Using Evolutionary Computation*, International Journal of Computational Fluid Dynamics, vol.17(5), pp 357-369, 2003.
- [21] Harinck, J., *Genetic Algorithm for Radial Turbomachinery Design Optimizations*, Delft, 2004.

- [22] Van den Braembussche, R.A., İşlek, A.A, and Alsalihi, Z., *Aerothermal Optimization of Micro-Gasturbine Compressor Including Heat Transfer*, International Gas Turbine Congress, Tokyo, 2003.
- [23] Miller, P.L., Oliver, J.H., Miller, D.P., and Tweedt, D.L., *BladeCAD: An Interactive Geometric Design Tool for Turbomachinery Blades*, 41st Gas Turbine and Aeroengine Congress, Birmingham, United Kingdom, June 10-13, 1996.
- [24] Iancu, F., Trevino, J., and Sommer, S., *Numerical Analysis of Blade Geometry Generation Techniques for Centrifugal Compressors*, International Journal of Rotating Machinery, vol. 2007, Article ID 48683, 2007.
- [25] Chu, C.H., Chen, J.T., *Tool Path Planning for Five-Axis Flank Milling With Developable Surface Approximation*, International Journal of Advanced Manufacturing Technologies, vol.29, pp 707-713, 2006.
- [26] Akça, D., Grün, A., Breuckmann, B., and Lahanier, C., *High Definition 3-D Scanning of Arts Objects and Paintings*, Optical 3-D Measurement Techniques VIII, vol. 2, pp 50-58, 2007.
- [27] Pazzi, S., Martelli, F., Michelassi, V., Giachi, M., and Bersini, H., *Intelligent Performance CFD Optimisation of a Centrifugal Impeller*, 5th European Conference on Turbomachinery, Prague, March 2003.
- [28] Katsanis, T., *Use of Arbitrary Quasi-Orthogonals for Calculating Flow Distribution in a Turbomachine*, NASA, Cleveland, Ohio, 1965.
- [29] Smith, K.J., and Hamrick, J.T., *A Rapid Approximate Method for the Design of Hub Shroud Profiles of Centrifugal Impellers of Given Blade Shape*, National Advisory Committee for Aeronautics, Technical Note 3399, Ohio, 1955.
- [30] Wu, C.H., *A General Theory of Three-Dimensional Flow in Subsonic and Supersonic Turbomachines of Axial-, Radial, and Mixed-Flow Types*, NASA, Washington, 1952.
- [31] Bardina, J.E., Huang, P.G., Coakley, T.J., *Turbulence Modelling Validation, Testing, and Development*, NASA Technical Memorandum 110446, 1997.

- [32] Wu, J., Shimmei, K., Tani, K., Niikura, K., and Sato, J., *CFD-Based Design Optimization for Hydro Turbines*, Journal of Fluids Engineering, vol. 129, pp 159-168, 2007.
- [33] Kuzmenko, M.L., Egorov, I.N., and Shmotin, Y.N., *Improvement of the Gas-Turbine Engine Compressor Using Modern CFD Technique and IOSO-NM Optimization Software*, Moscow, Russia, 2006.
- [34] Kim, K.Y., and Seo, S.J., *Design Optimization of Turbomachinery Using Three-Dimensional Navier-Stokes Analysis*, The 7th Asian International Conference on Fluid Machinery, Fukuoka, Japan, 2003.
- [35] Liu, Z., and Hill, D.L., *Issues Surrounding Multiple Frames of Reference Models for Turbo Compressor Applications*, Olean, NY USA.
- [36] Mason, R.L., Gunst, R.F., and Hess, J.L., *Statistical Design and Analysis of Experiments*, 2nd edition, John Wiley & Sons, NJ, USA, 2003.
- [37] Papila, N.U., *Neural Network and Polynomial Based Response Surface Techniques for Supersonic Turbine Design Optimization*, 2001.
- [38] Wu, K.H., Lin, B.J., and Hung, C.I., *Novel Design of Centrifugal Pump Impellers Using Generated Machining Method and CFD*, Engineering Applications of Computational Fluid Mechanics, vol. 2, pp. 195-207, 2008.
- [39] Japikse, D., and Platt, M.J., *Optimization in Component Design and Redesign*, The 10th International Symposium on Transport Phenomena and Dynamics of Rotating Machinery, Honolulu, Hawaii, 2004.
- [40] Myers, R.H., Montgomery, D.C., and Anderson, M.C., *Response Surface Methodology*, 3rd edition, John Wiley & Sons, NJ USA, 2009.
- [41] Cannady, J., *Artificial Neural Networks for Misuse Detection*, Nova Southeastern University, 2003.
- [42] *Neural Networks*, WEB: <http://www.learnartificialneuralnetworks.com> (20.06.2009)

- [43] Hasanoğlu, M.S., *Storage Reliability Analysis of Solid Rocket Propellants*, 2008.
- [44] McGlumphy, J., and Fai-Ng, W., *An Investigation to Improve Gas Turbine Engine Performance Through the Use of Splittered Rotors*, Blacksburg, USA.
- [45] Lakshminarayana, B., *Fluid Dynamics and Heat Transfer of Turbomachinery*, John Wiley & Sons, 1996.
- [46] Hasanoğlu, M.S., Karbancıoğlu, İ.M., and Kutluay, Ü., *External Geometry Optimization with Flight Mechanics Constraints Using Response Surfaces*, AIAA-2008-6886, Atmospheric Flight Mechanics Conference & Exhibit, Honolulu, Hawaii, 2008.
- [47] FLUENT-Computational Fluid Dynamics Software, Version 6.3, Ansys Inc., 2008.
- [48] GAMBIT, Version 2.4.6, Fluent Inc., 2004.
- [49] JMP, Version 7.0, SAS Institute Inc., 2007.

APPENDIX A

I-OPTIMAL DESIGN SPACE

Table A.1 I-optimal Design Space

Design Number	COR _h	COR _s	H2Z	H3R	S2Z	S3R	S1R	β_{ih}	β_{is}	β_{eh}	β_{es}	N	Pressure Ratio
1	0.15	0.3	5	22.5	17.5	35	30	50	70	30	30	6	3.318
2	0.15	0.3	15	15	10	32.5	32.5	30	40	0	15	7	2.864
3	0.15	0.3	15	15	25	35	32.5	40	70	30	0	7	3.689
4	0.15	0.3	15	22.5	17.5	35	32.5	50	70	0	15	8	4.162
5	0.15	0.3	25	15	10	30	35	50	70	0	0	7	3.4606
6	0.15	0.3	25	30	10	30	32.5	50	40	30	0	6	Choked
7	0.15	0.3	25	30	25	30	32.5	30	40	30	30	8	Choked
8	0.15	0.3	25	30	25	35	35	30	55	0	30	6	2.8313
9	0.15	0.3	25	30	25	35	35	50	40	0	0	7	3.3517
10	0.15	0.4	5	15	10	32.5	30	50	70	0	0	8	3.3932

Design Number	COR_h	COR_s	H2Z	H3R	S2Z	S3R	S1R	β_{ih}	β_{is}	β_{eh}	β_{es}	N	Pressure Ratio
11	0.15	0.4	5	15	17.5	30	35	50	40	30	0	8	2.6851
12	0.15	0.4	15	22.5	17.5	32.5	35	40	55	15	15	6	2.8954
13	0.15	0.4	15	30	10	30	30	50	70	15	30	7	2.0137
14	0.15	0.4	25	15	10	35	30	30	40	15	0	6	3.2245
15	0.15	0.4	25	15	25	35	30	50	55	0	30	6	3.6829
16	0.15	0.4	25	22.5	10	30	32.5	50	70	30	15	8	2.2424
17	0.15	0.5	5	15	17.5	35	32.5	50	70	15	15	7	3.8374
18	0.15	0.5	5	15	25	30	30	40	40	30	30	6	2.9093
19	0.15	0.5	5	22.5	17.5	30	35	30	40	0	30	7	2.2248
20	0.15	0.5	5	30	10	35	30	30	40	30	30	7	2.7961
21	0.15	0.5	5	30	25	30	30	30	70	0	0	6	3.9417
22	0.15	0.5	5	30	25	35	30	50	70	15	0	8	3.178
23	0.15	0.5	15	22.5	10	30	35	30	70	0	30	8	2.7753
24	0.15	0.5	25	30	25	32.5	35	50	70	30	30	7	3.024
25	0.225	0.3	5	15	10	30	35	50	70	30	30	6	2.7055
26	0.225	0.3	5	15	25	35	35	50	40	15	0	6	3.0736

Design Number	COR _h	COR _s	H2Z	H3R	S2Z	S3R	S1R	β_{ih}	β_{is}	β_{eh}	β_{es}	N	Pressure Ratio
27	0.225	0.3	5	22.5	10	30	30	40	40	15	15	8	2.394
28	0.225	0.3	5	30	25	32.5	30	50	40	30	30	7	3.1871
29	0.225	0.3	15	22.5	10	32.5	35	50	55	30	0	7	2.7532
30	0.225	0.3	25	22.5	17.5	30	30	50	40	0	15	6	1.9534
31	0.225	0.3	25	30	10	30	30	30	70	30	30	6	Choked
32	0.225	0.4	5	15	17.5	35	35	30	70	0	30	6	3.3433
33	0.225	0.4	5	22.5	25	32.5	30	30	55	30	0	8	3.647
34	0.225	0.4	5	30	10	35	32.5	50	55	0	15	6	3.4839
35	0.225	0.4	5	30	17.5	35	30	30	40	0	30	8	3.5428
36	0.225	0.4	5	30	25	30	35	30	70	30	30	6	2.868
37	0.225	0.4	15	22.5	17.5	32.5	32.5	40	55	15	15	6	3.2578
38	0.225	0.4	15	30	25	32.5	35	30	70	0	0	7	3.7059
39	0.225	0.4	15	30	25	35	35	50	55	30	30	8	2.8512
40	0.225	0.4	25	15	17.5	32.5	35	40	55	15	30	8	2.9472
41	0.225	0.4	25	22.5	17.5	35	32.5	40	40	15	30	7	3.0357
42	0.225	0.4	25	30	10	35	35	30	40	30	0	8	Choked

Design Number	COR _h	COR _s	H2Z	H3R	S2Z	S3R	S1R	β_{ih}	β_{is}	β_{eh}	β_{es}	N	Pressure Ratio
43	0.225	0.4	25	30	25	30	30	40	70	0	15	8	Choked
44	0.225	0.5	5	22.5	17.5	30	32.5	30	70	30	0	7	3.5683
45	0.225	0.5	15	15	10	35	32.5	40	55	15	0	8	3.6558
46	0.225	0.5	15	15	25	30	30	50	55	30	30	8	3.4102
47	0.225	0.5	15	30	10	30	35	50	55	0	0	8	1.9228
48	0.225	0.5	15	30	25	35	30	40	40	30	15	6	3.1909
49	0.225	0.5	25	15	25	30	30	40	40	15	0	7	3.5706
50	0.225	0.5	25	15	25	32.5	35	30	70	30	0	6	3.2355
51	0.225	0.5	25	22.5	10	35	30	30	70	0	15	7	3.5417
52	0.3	0.3	5	15	17.5	35	35	30	40	30	30	8	2.48
53	0.3	0.3	5	30	10	35	35	30	55	0	0	7	3.2443
54	0.3	0.3	5	30	10	35	35	30	70	30	0	6	3.1058
55	0.3	0.3	5	30	25	30	35	50	40	0	30	6	2.6686
56	0.3	0.3	5	30	25	35	30	40	70	0	30	7	3.8564
57	0.3	0.3	15	22.5	25	32.5	32.5	40	40	0	0	8	3.5913
58	0.3	0.3	15	30	25	30	35	40	70	30	0	8	3.3977

Design Number	COR_h	COR_s	H2Z	H3R	S2Z	S3R	S1R	β_{ih}	β_{is}	β_{eh}	β_{es}	N	Pressure Ratio
59	0.3	0.3	25	15	10	35	35	50	40	30	30	6	2.3652
60	0.3	0.3	25	15	25	30	30	30	70	0	30	7	3.7929
61	0.3	0.3	25	22.5	25	35	30	30	70	30	30	8	3.4604
62	0.3	0.3	25	30	10	35	30	50	40	0	30	8	Choked
63	0.3	0.3	25	30	17.5	32.5	32.5	30	55	15	0	7	2.1768
64	0.3	0.4	5	22.5	25	30	32.5	50	55	0	15	7	3.6844
65	0.3	0.4	15	15	17.5	32.5	30	50	70	30	0	6	3.3592
66	0.3	0.4	15	15	25	30	35	30	40	0	0	6	2.8579
67	0.3	0.4	15	15	25	30	35	50	40	15	30	7	2.6985
68	0.3	0.4	25	15	10	30	30	50	55	30	30	7	2.2342
69	0.3	0.4	25	30	10	30	35	40	40	15	15	7	Choked
70	0.3	0.4	25	30	25	35	35	50	70	15	0	6	3.6673
71	0.3	0.5	5	15	10	35	35	50	40	0	30	8	3.0576
72	0.3	0.5	5	15	17.5	35	30	50	40	0	0	7	3.9066
73	0.3	0.5	5	15	25	30	35	30	70	15	15	8	3.5897
74	0.3	0.5	5	22.5	10	32.5	32.5	30	40	15	30	6	2.4128

Design Number	COR_h	COR_s	H2Z	H3R	S2Z	S3R	S1R	β_{ih}	β_{is}	β_{eh}	β_{es}	N	Pressure Ratio
75	0.3	0.5	5	30	17.5	32.5	32.5	40	70	30	30	8	3.4148
76	0.3	0.5	15	15	10	35	35	30	70	30	30	7	2.8183
77	0.3	0.5	25	15	10	30	30	50	70	0	30	6	2.4019
78	0.3	0.5	25	15	17.5	30	30	30	55	0	0	8	3.8249
79	0.3	0.5	25	15	25	35	30	50	40	30	15	8	3.5077
80	0.3	0.5	25	15	25	35	35	30	40	0	0	7	3.2792
81	0.3	0.5	25	30	10	30	30	30	40	0	0	7	Choked

APPENDIX B

CFD RESULTS

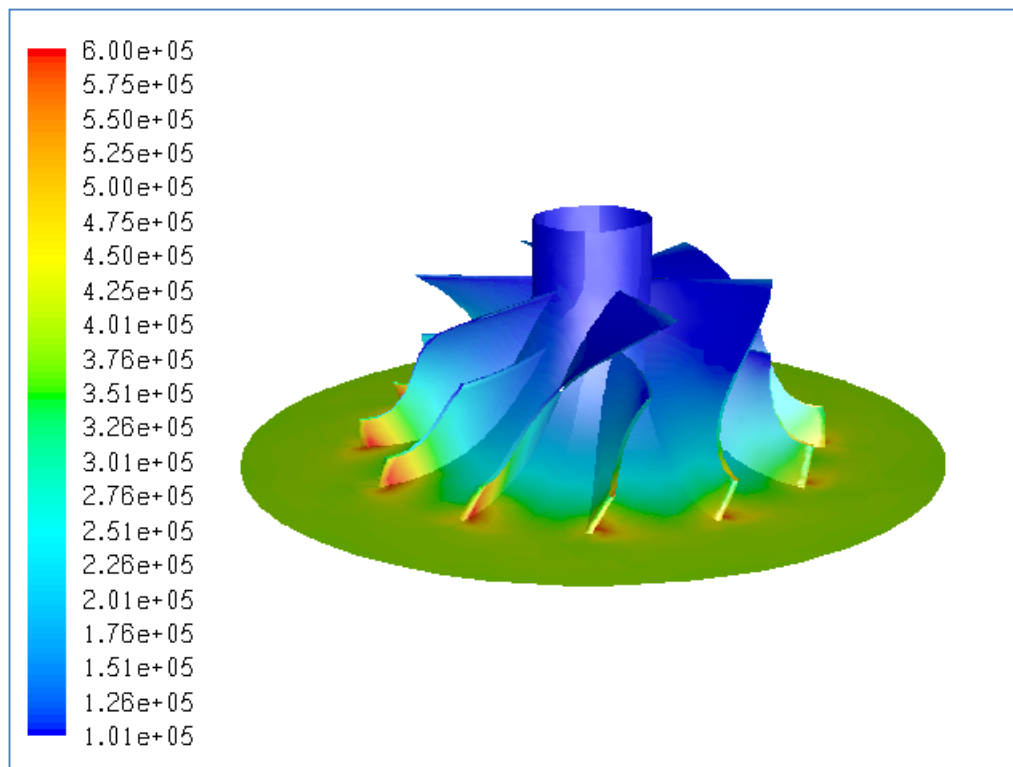


Figure B.1 Total Pressure Distribution (in Pa) for Original Case, PR=3.68

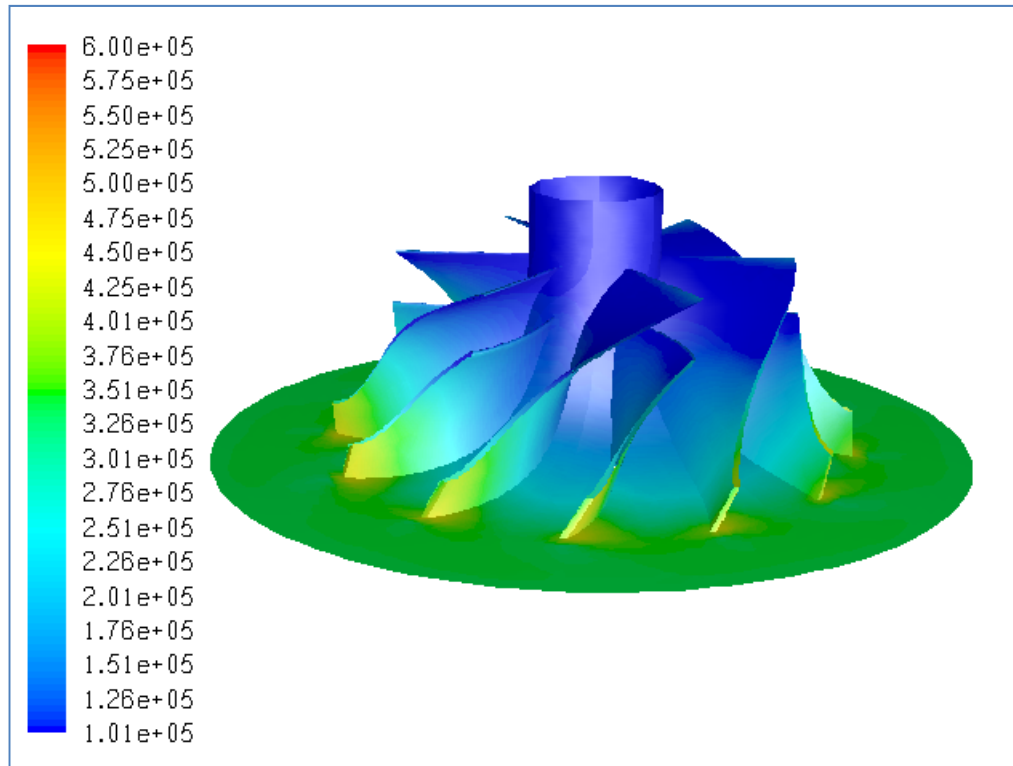


Figure B.2 Total Pressure Distribution (in Pa) for Case #1, PR=3.32

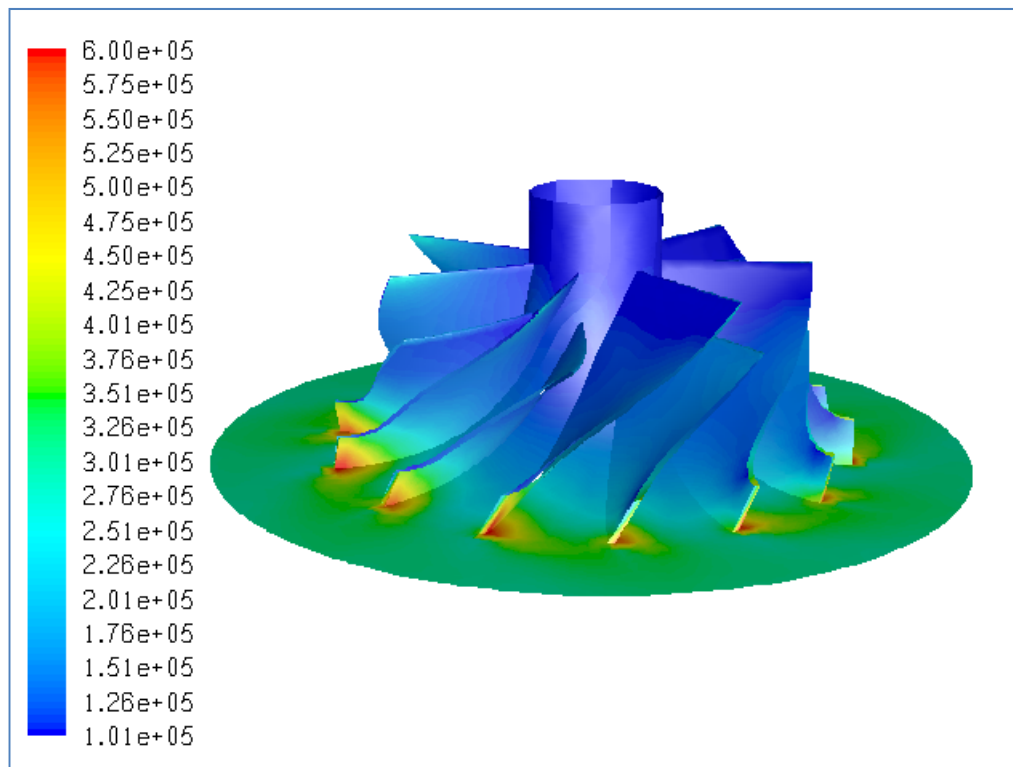


Figure B.3 Total Pressure Distribution (in Pa) for Case #2, PR=2.86

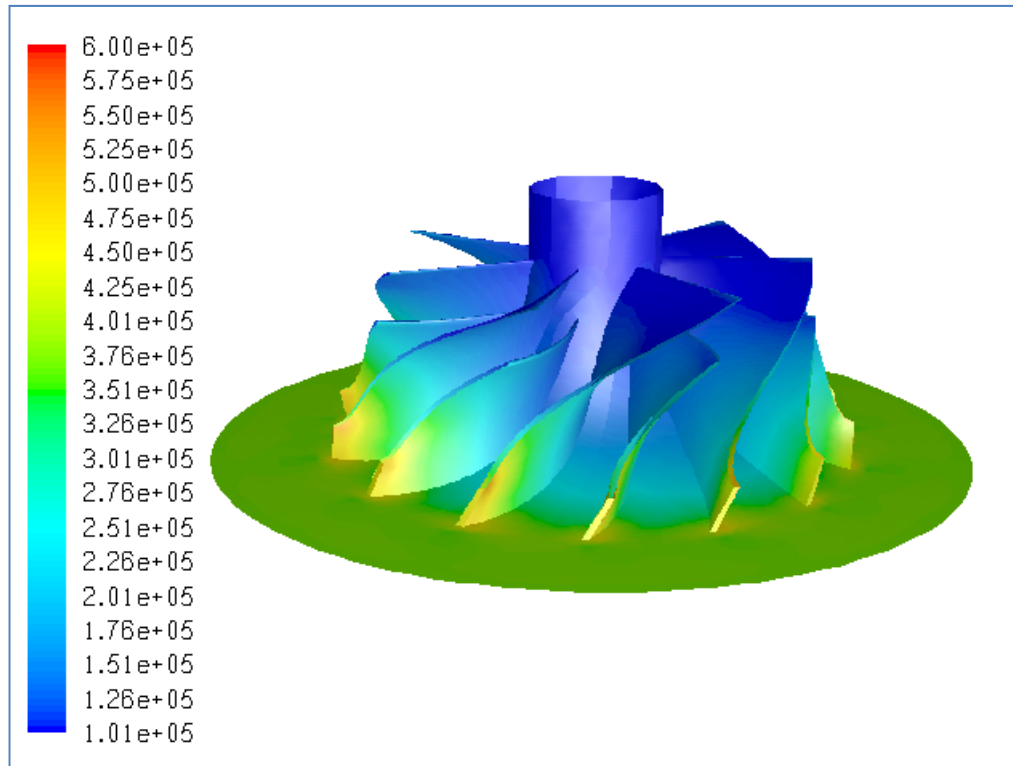


Figure B.4 Total Pressure Distribution (in Pa) for Case #3, PR=3.69

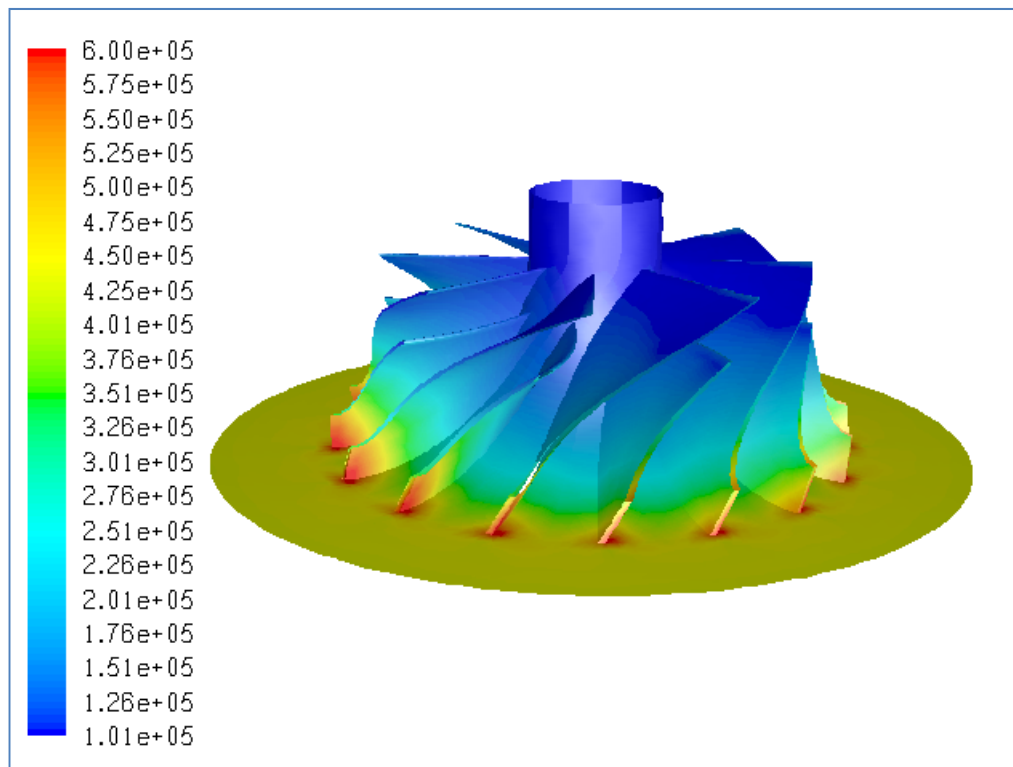


Figure B.5 Total Pressure Distribution (in Pa) for Case #4, PR=4.16

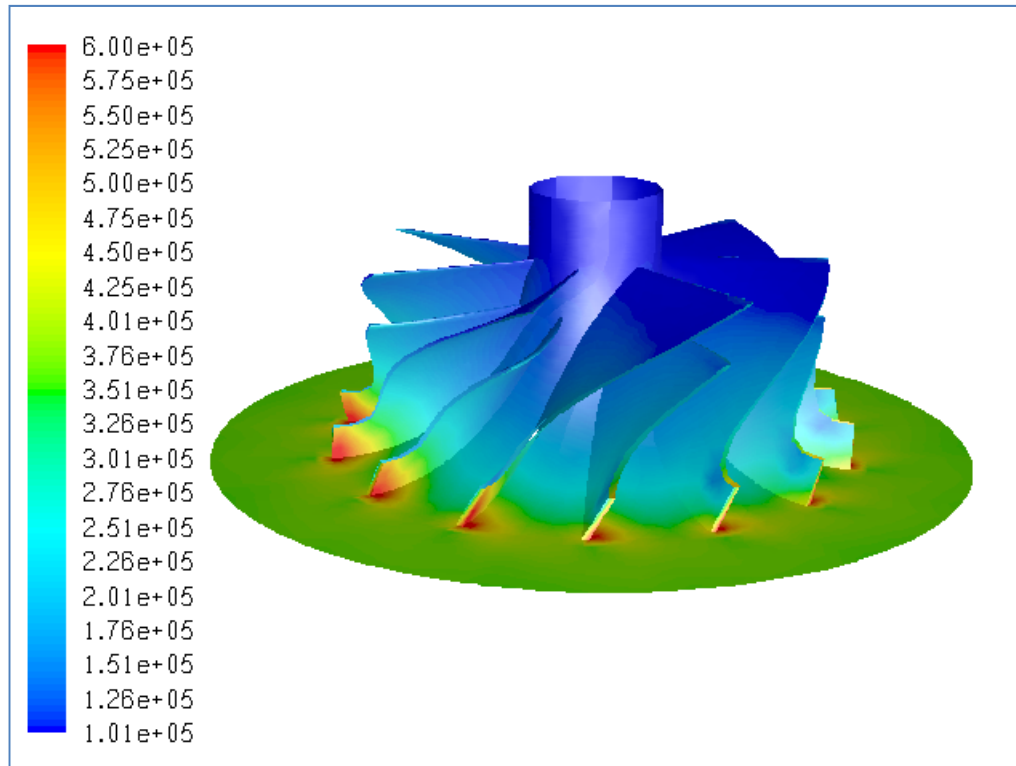


Figure B.6 Total Pressure Distribution (in Pa) for Case #5, PR=3.46

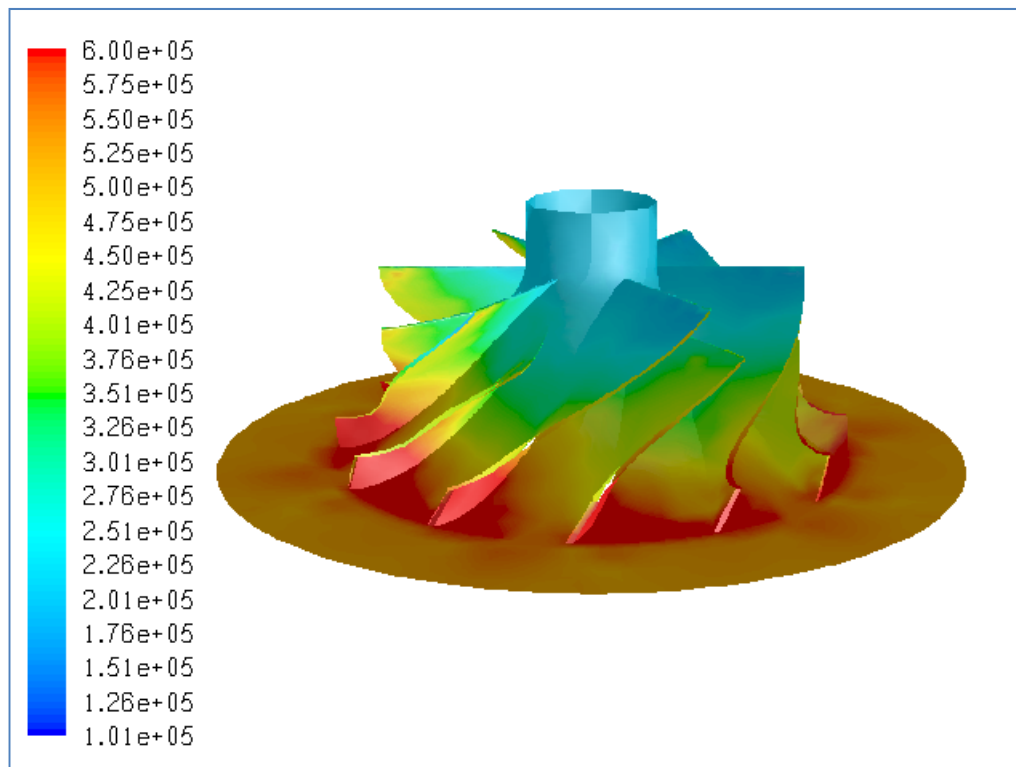


Figure B.7 Total Pressure Distribution (in Pa) for Case #6, Choked

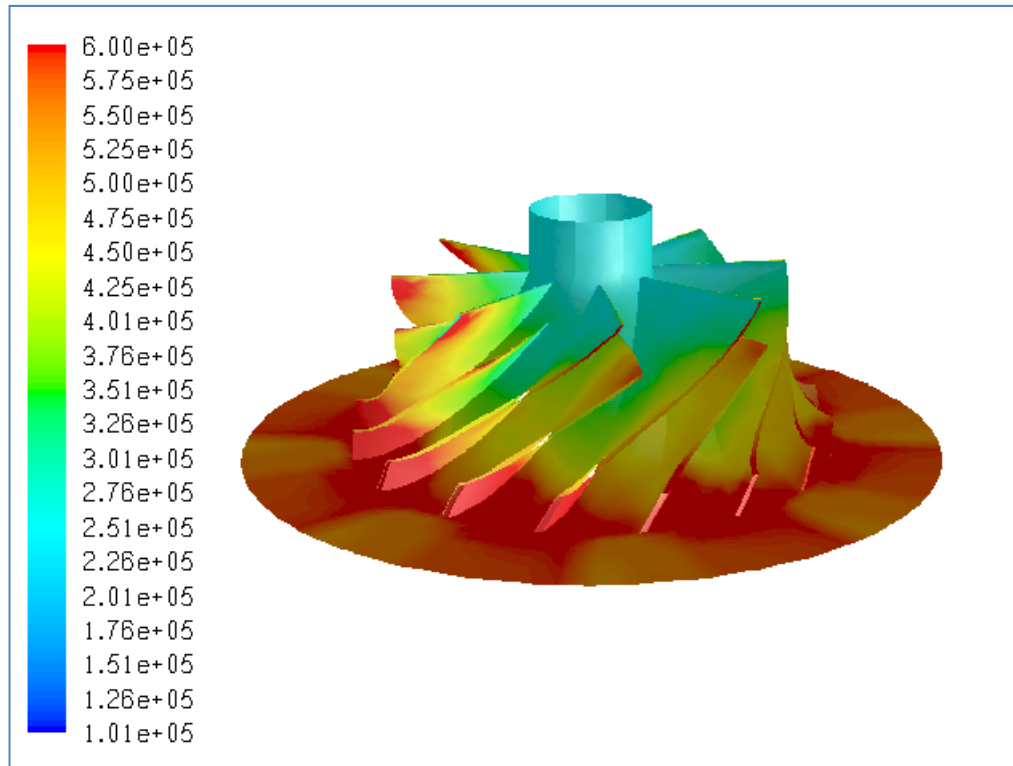


Figure B.8 Total Pressure Distribution (in Pa) for Case #7, Choked

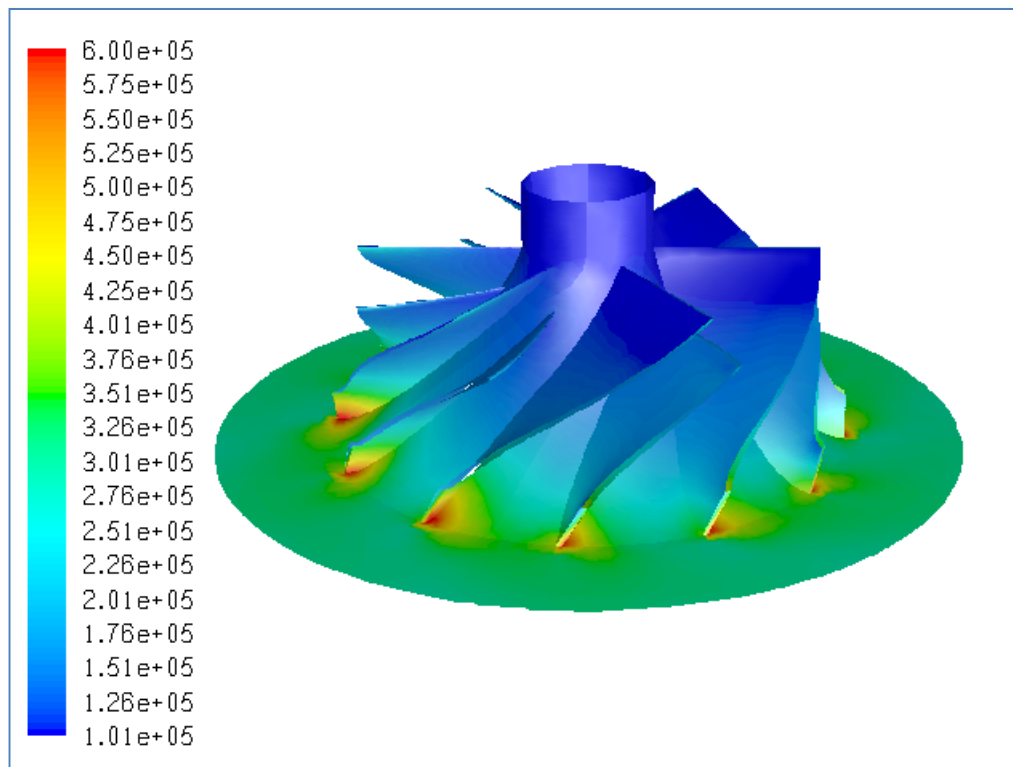


Figure B.9 Total Pressure Distribution (in Pa) for Case #8, PR=2.83

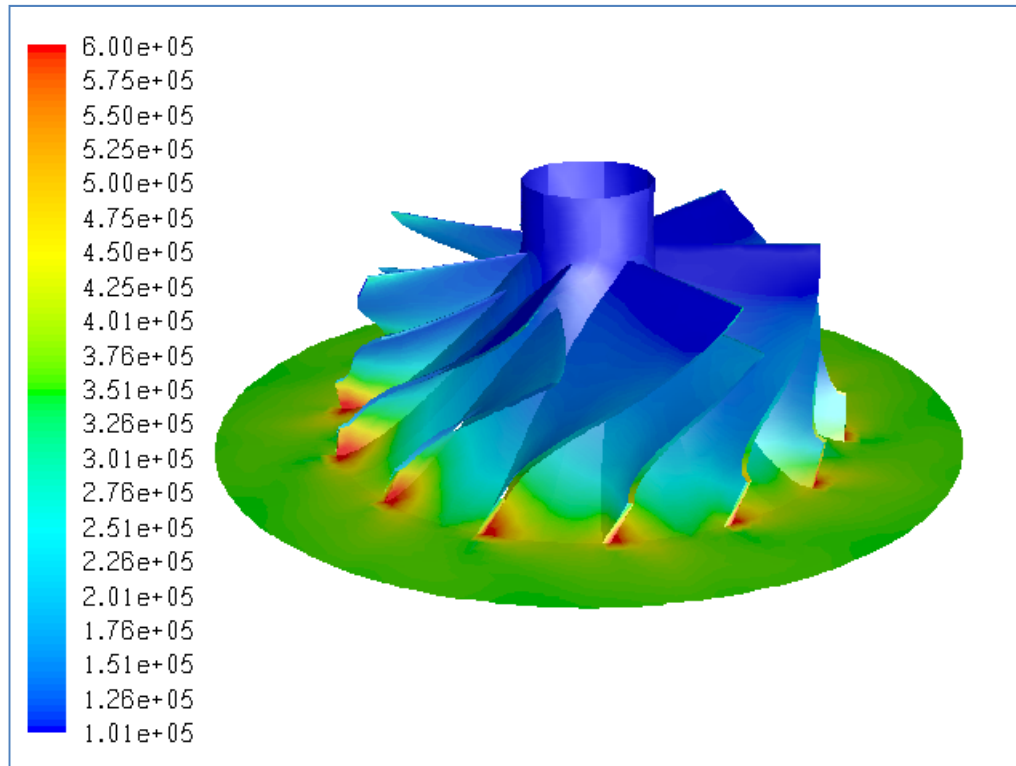


Figure B.10 Total Pressure Distribution (in Pa) for Case #9, PR=3.35

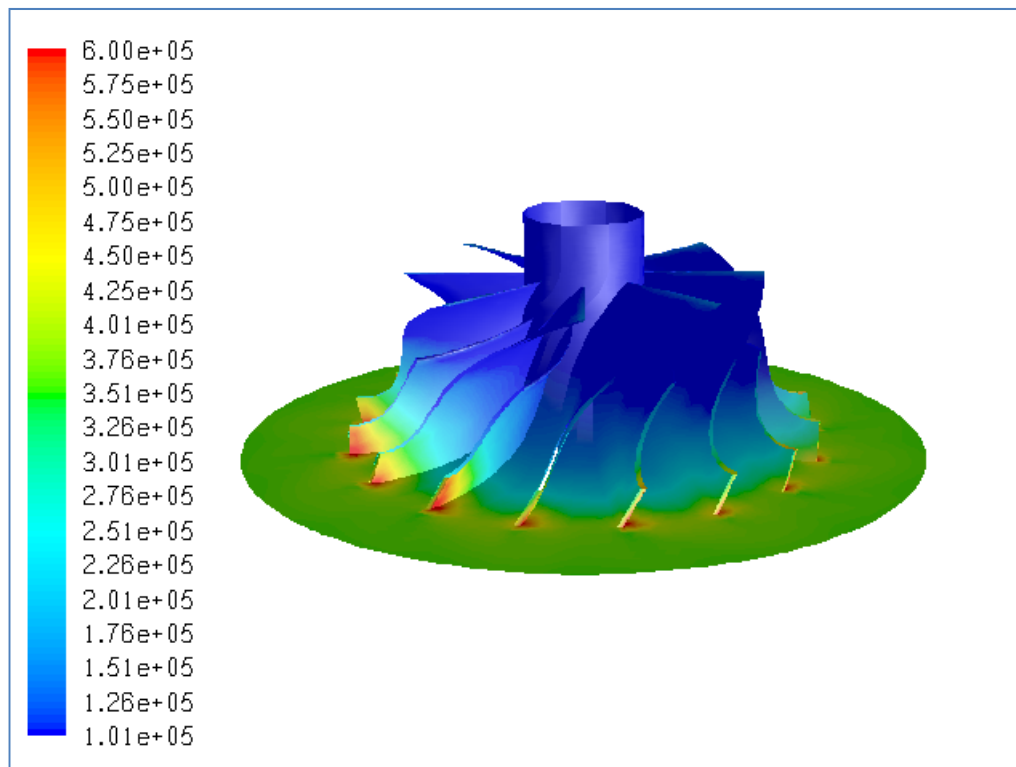


Figure B.11 Total Pressure Distribution (in Pa) for Case #10, PR=3.39

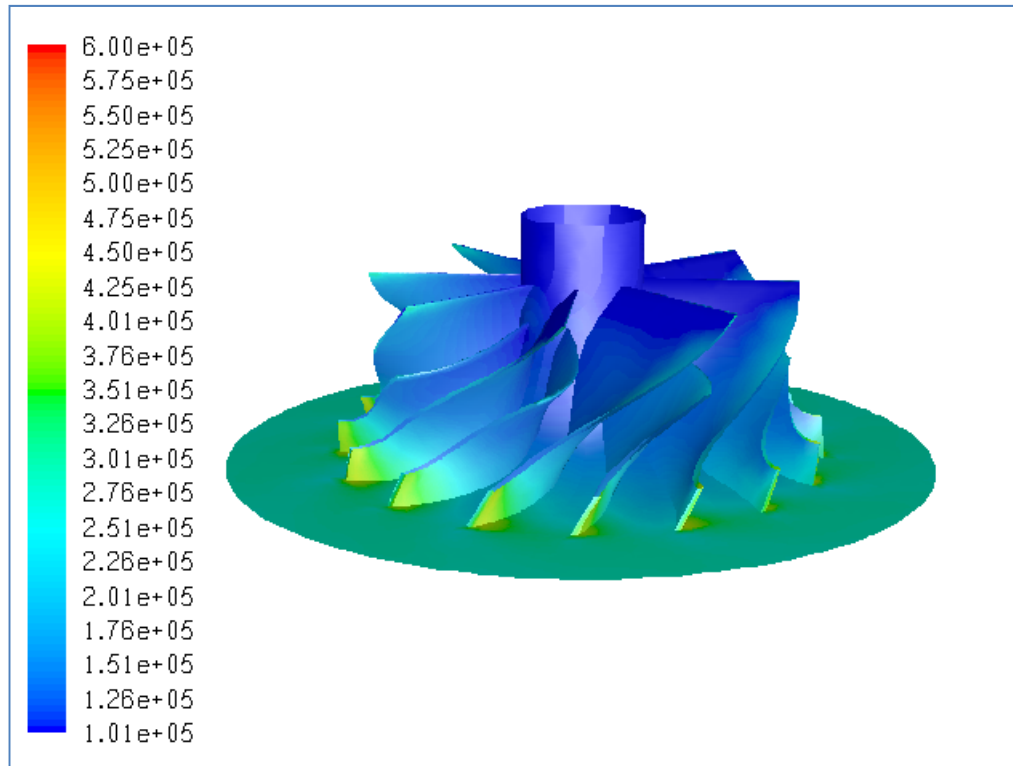


Figure B.12 Total Pressure Distribution (in Pa) for Case #11, PR=2.69

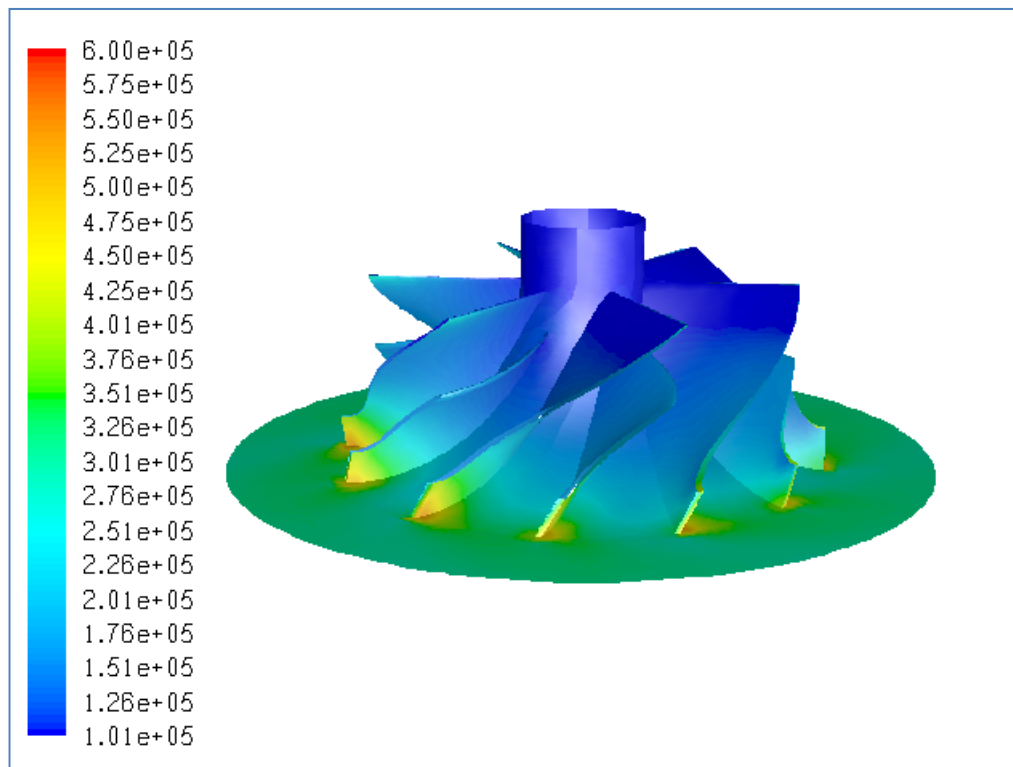


Figure B.13 Total Pressure Distribution (in Pa) for Case #12, PR=2.89

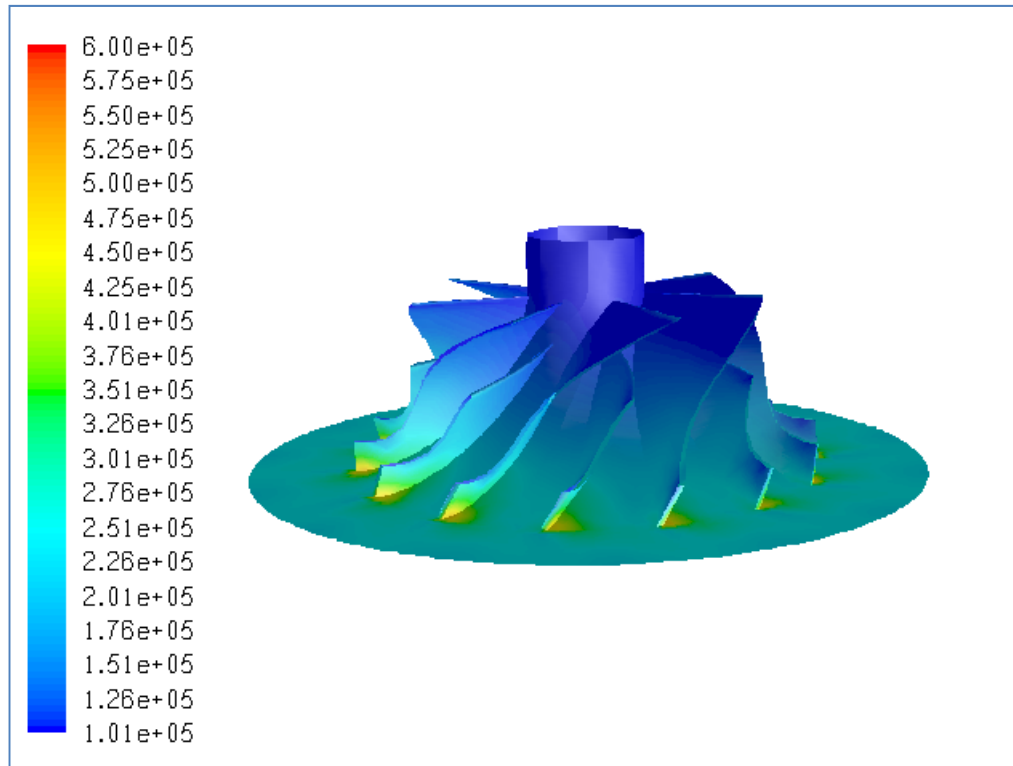


Figure B.14 Total Pressure Distribution (in Pa) for Case #13, PR=2.01

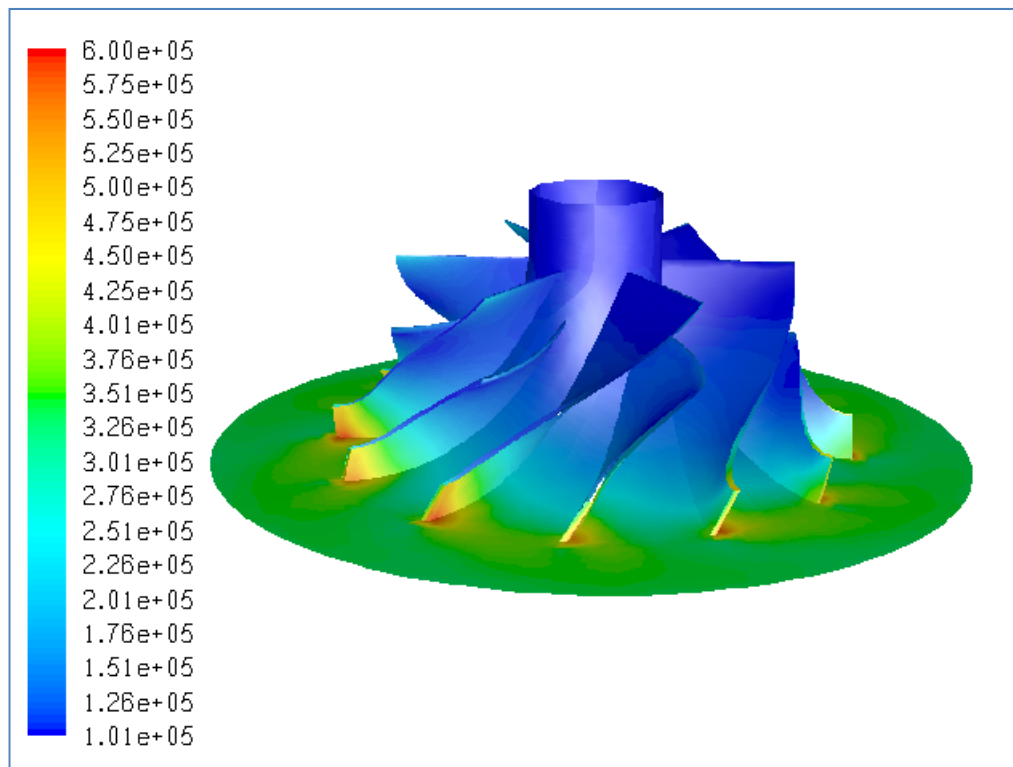


Figure B.15 Total Pressure Distribution (in Pa) for Case #14, PR=3.22

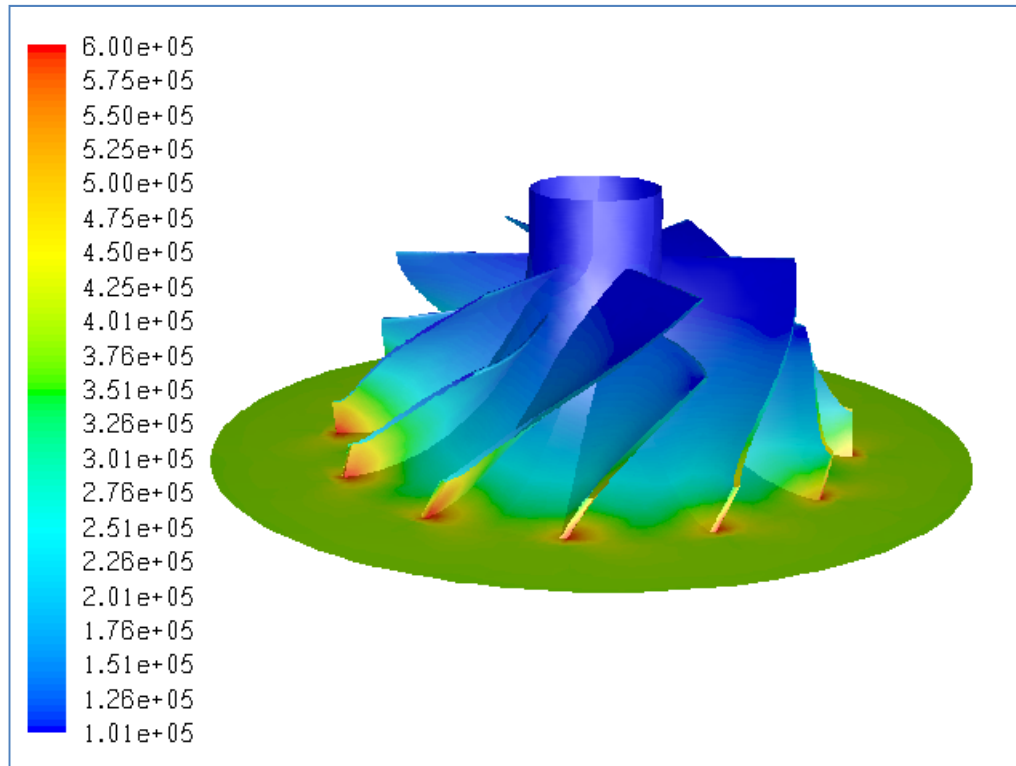


Figure B.16 Total Pressure Distribution (in Pa) for Case #15, PR=3.68

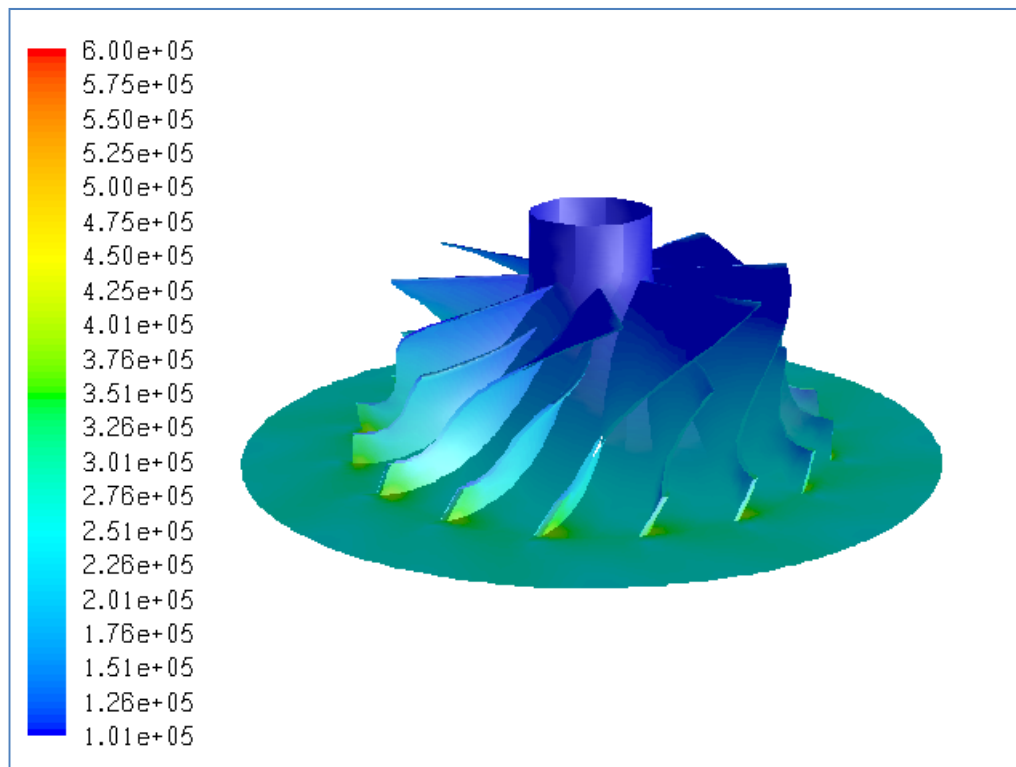


Figure B.17 Total Pressure Distribution (in Pa) for Case #16, PR=2.24

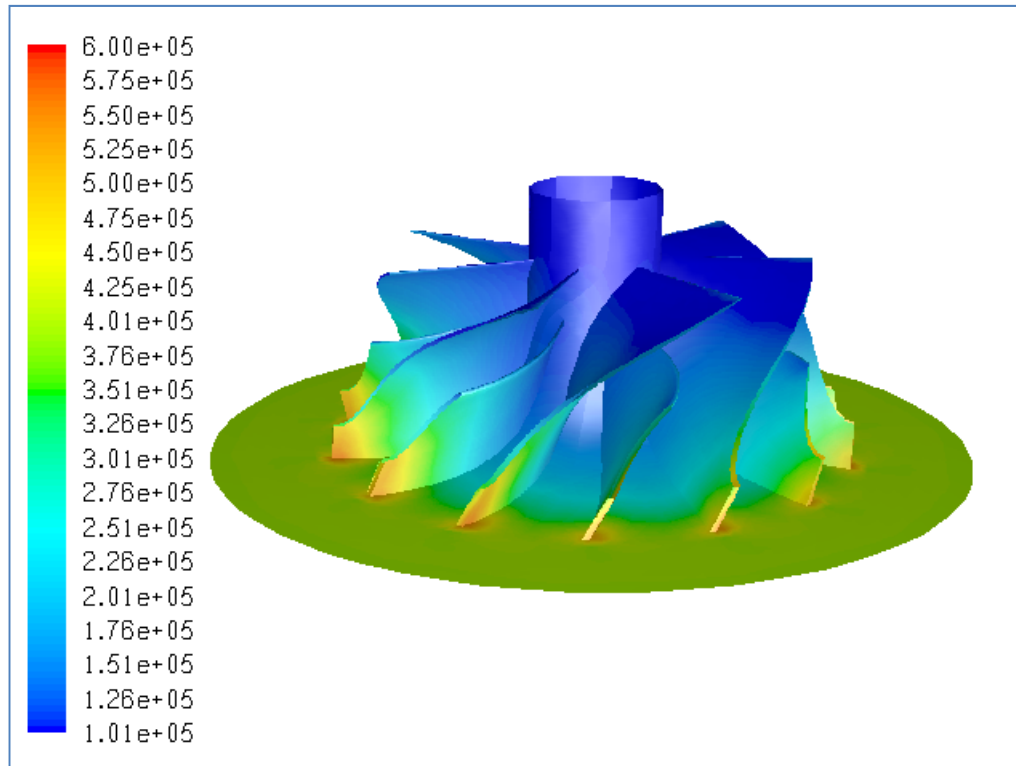


Figure B.18 Total Pressure Distribution (in Pa) for Case #17, PR=3.84

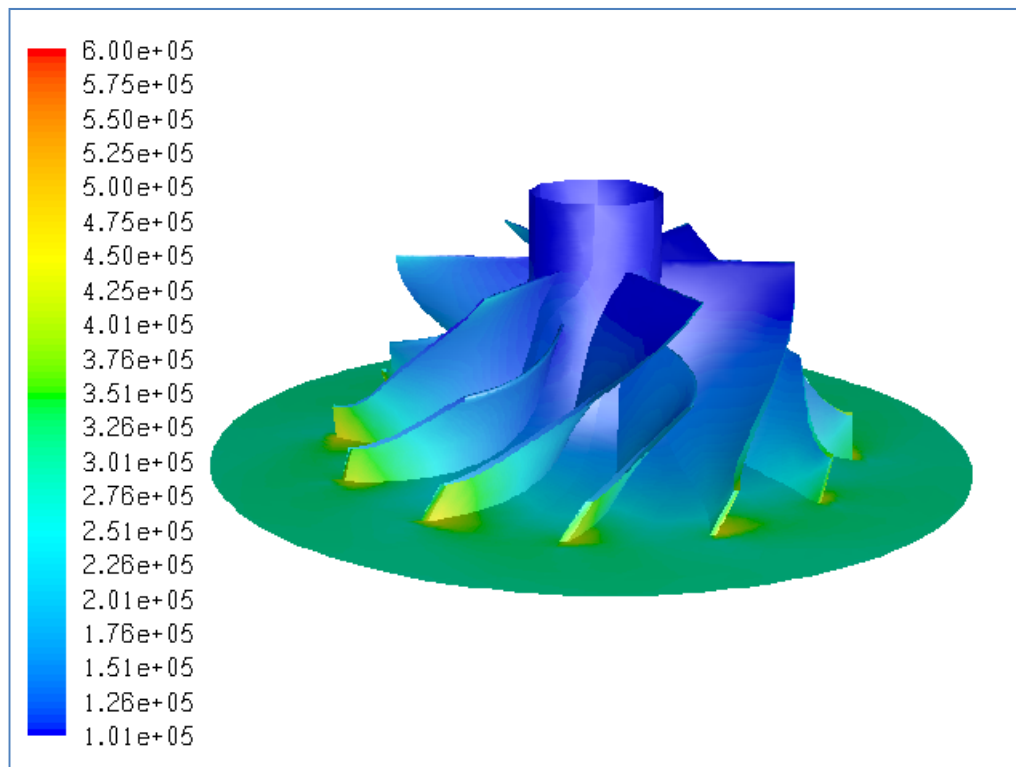


Figure B.19 Total Pressure Distribution (in Pa) for Case #18, PR=2.91

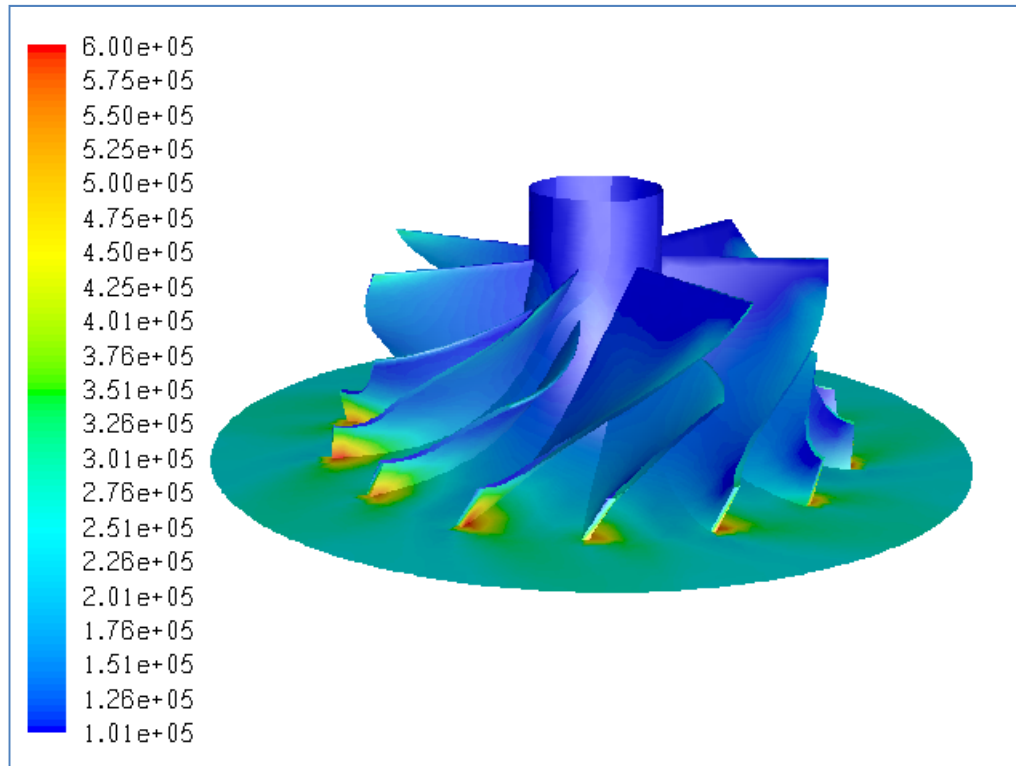


Figure B.20 Total Pressure Distribution (in Pa) for Case #19, PR=2.22

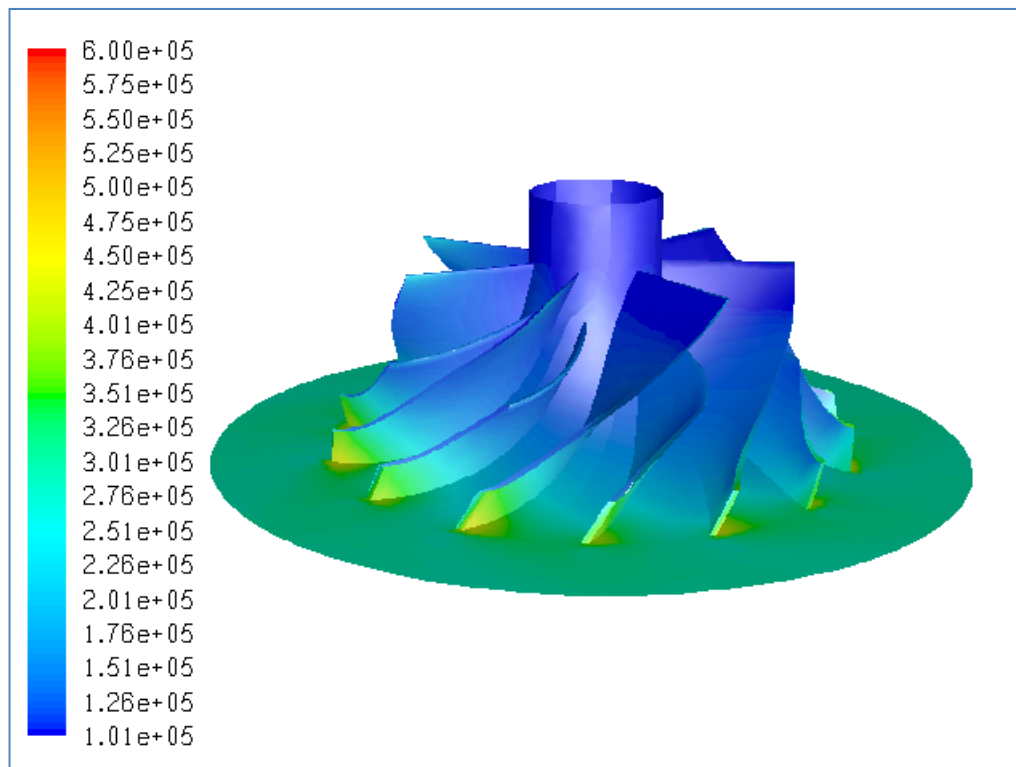


Figure B.21 Total Pressure Distribution (in Pa) for Case #20, PR=2.80

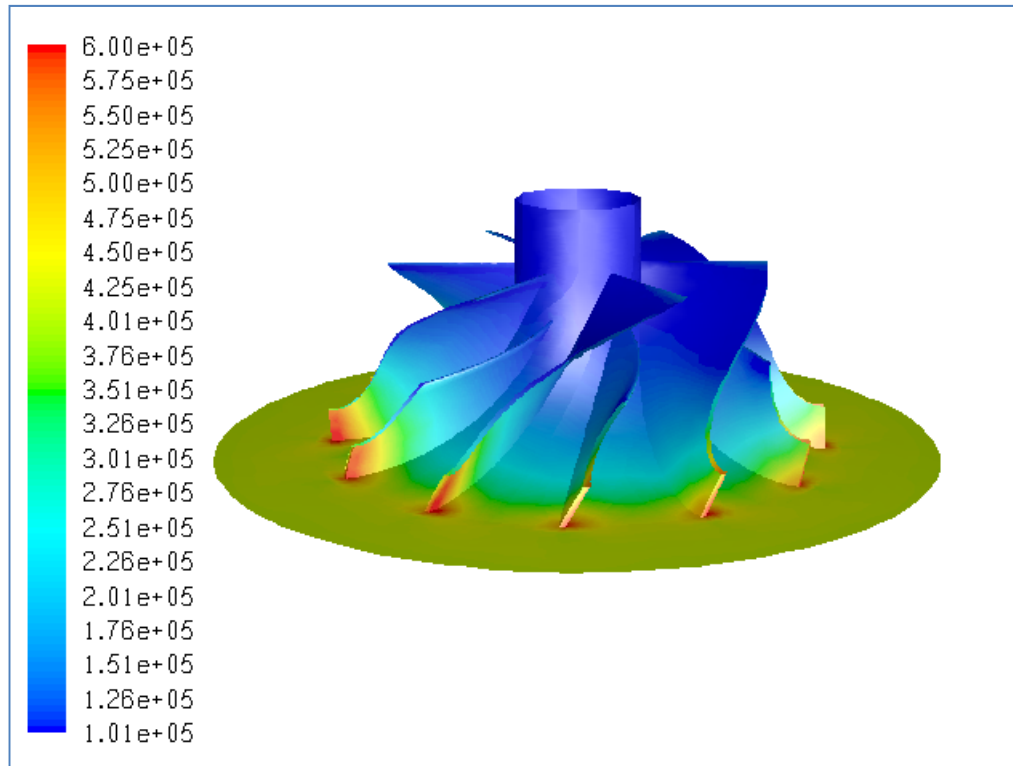


Figure B.22 Total Pressure Distribution (in Pa) for Case #21, PR=3.94

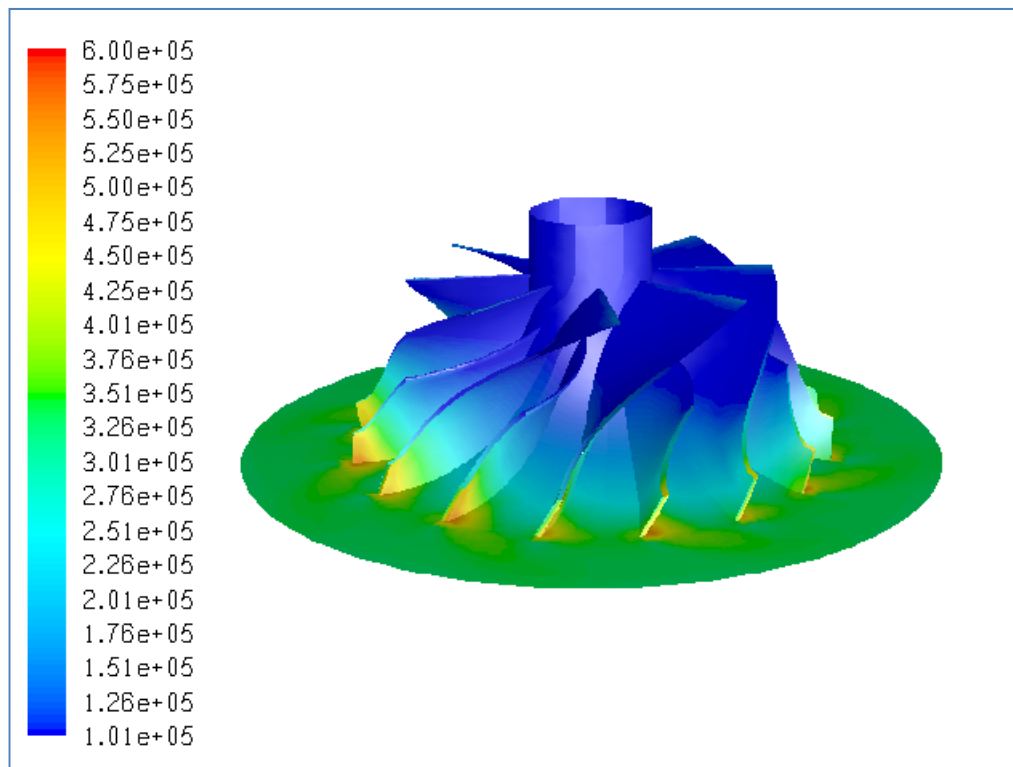


Figure B.23 Total Pressure Distribution (in Pa) for Case #22, PR=3.18

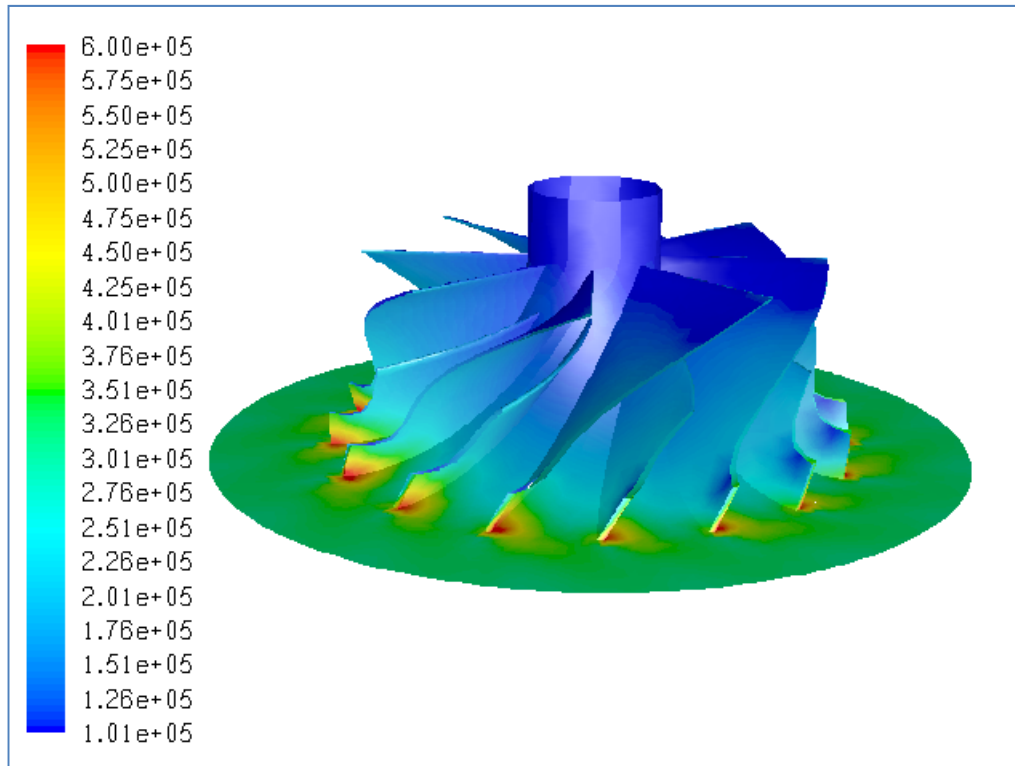


Figure B.24 Total Pressure Distribution (in Pa) for Case #23, PR=2.78

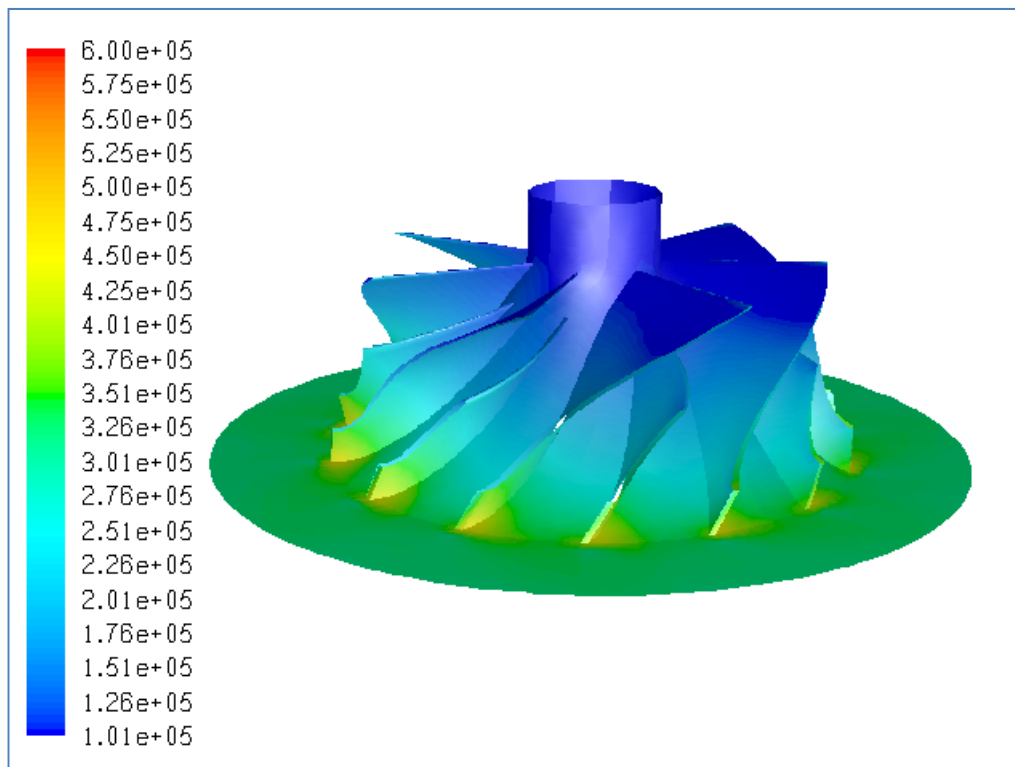


Figure B.25 Total Pressure Distribution (in Pa) for Case #24, PR=3.02

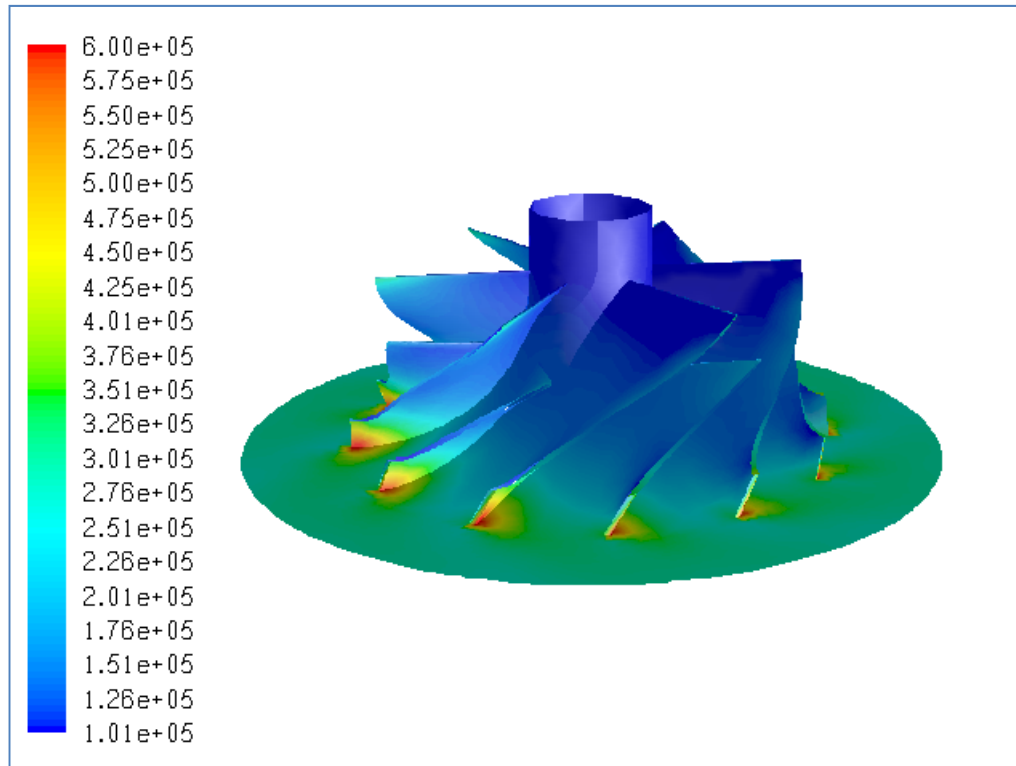


Figure B.26 Total Pressure Distribution (in Pa) for Case #25, PR=2.71

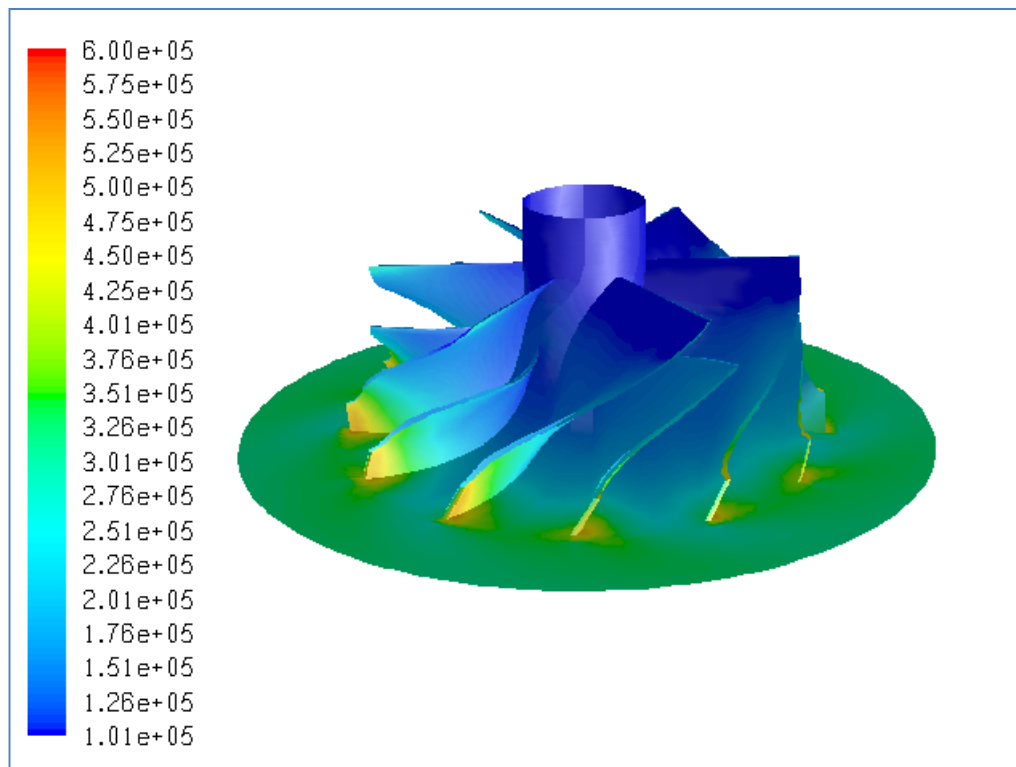


Figure B.27 Total Pressure Distribution (in Pa) for Case #26, PR=3.07

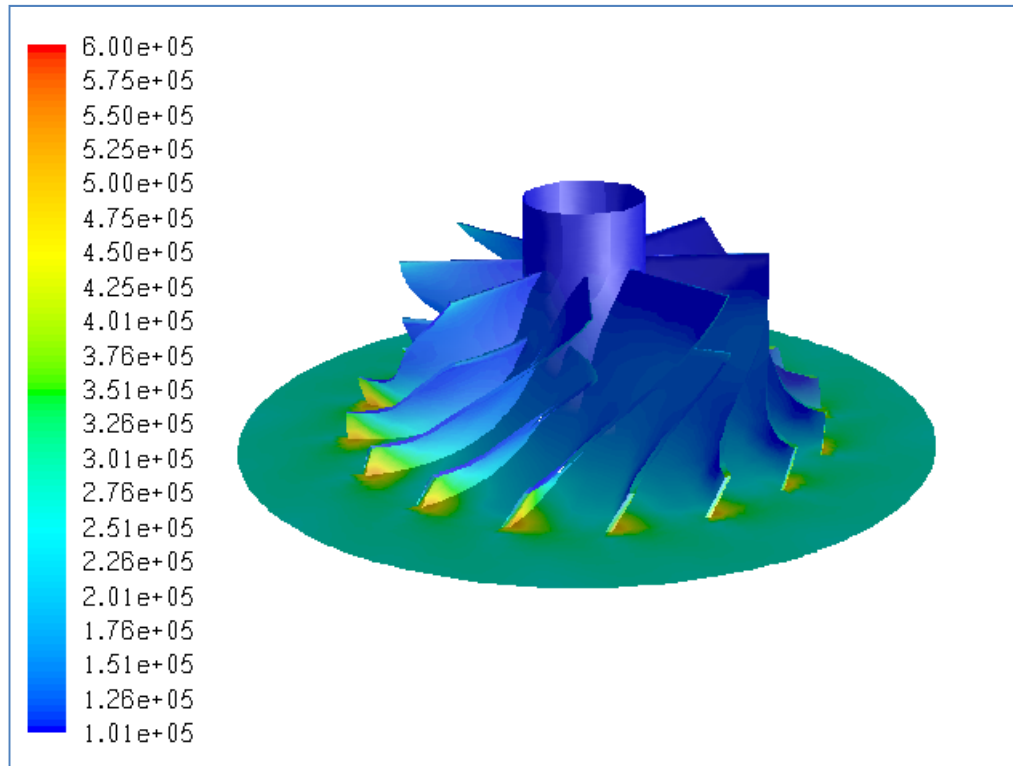


Figure B.28 Total Pressure Distribution (in Pa) for Case #27, PR=2.39

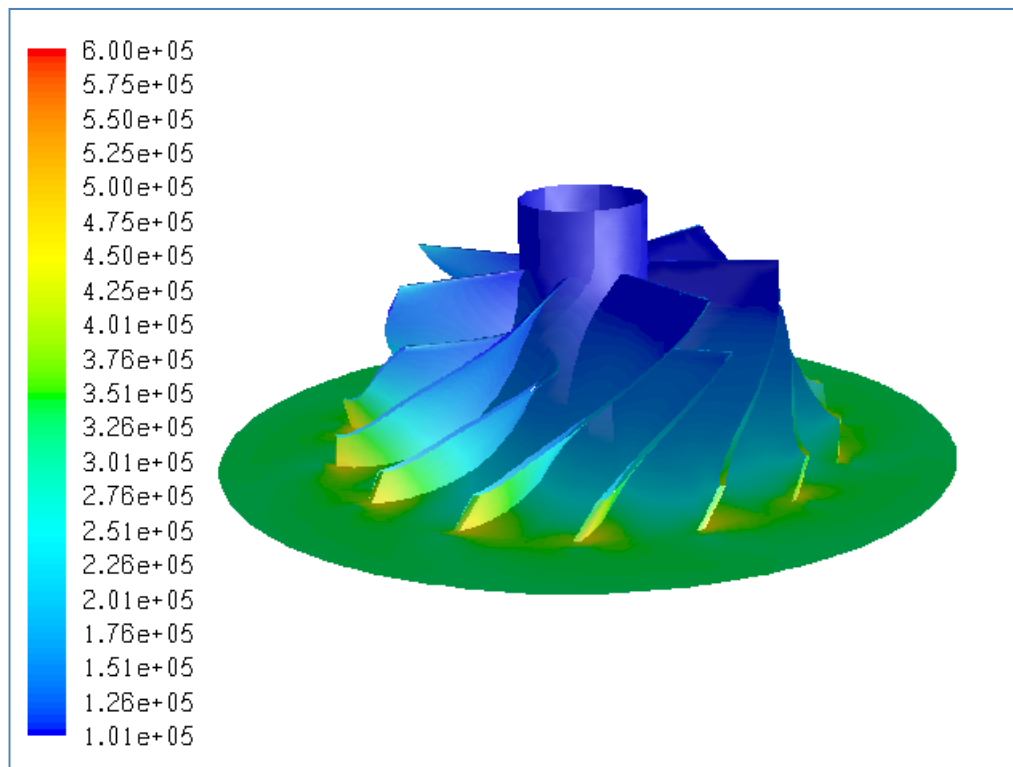


Figure B.29 Total Pressure Distribution (in Pa) for Case #28, PR=3.19

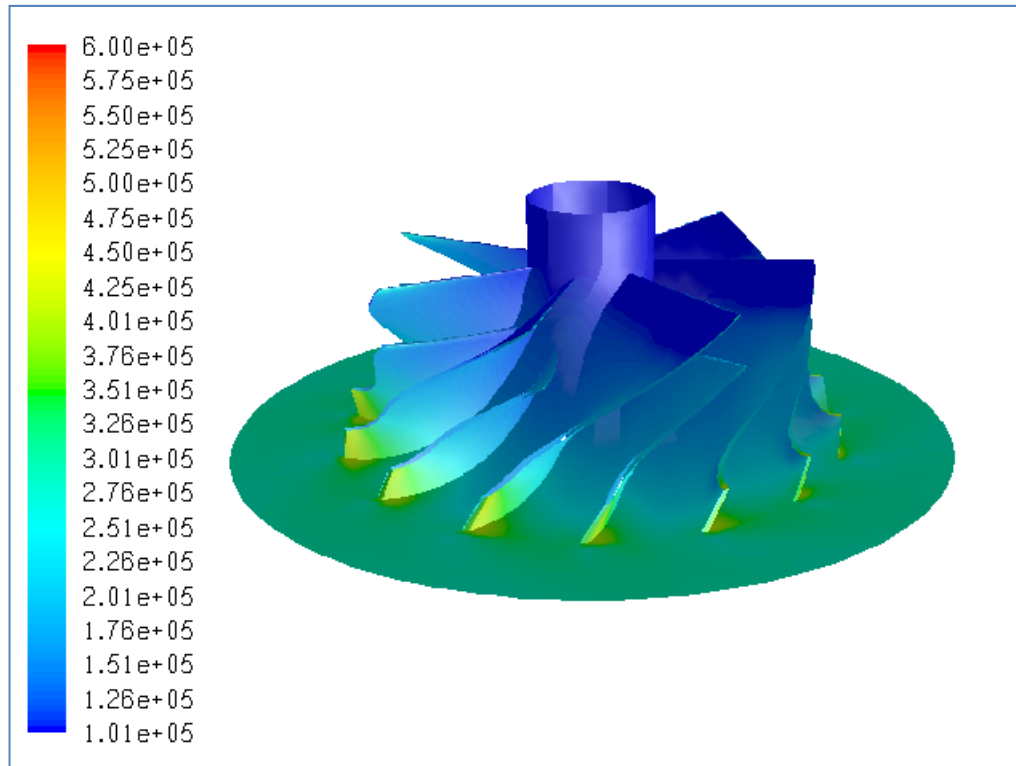


Figure B.30 Total Pressure Distribution (in Pa) for Case #29, PR=2.75

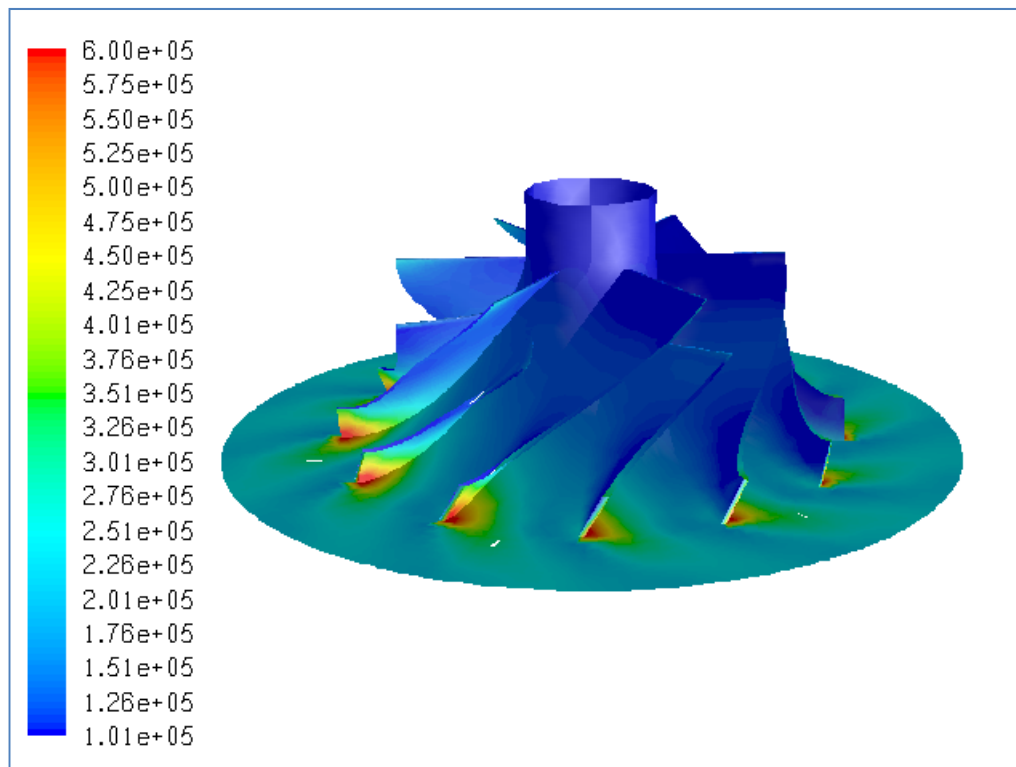


Figure B.31 Total Pressure Distribution (in Pa) for Case #30, PR=1.95

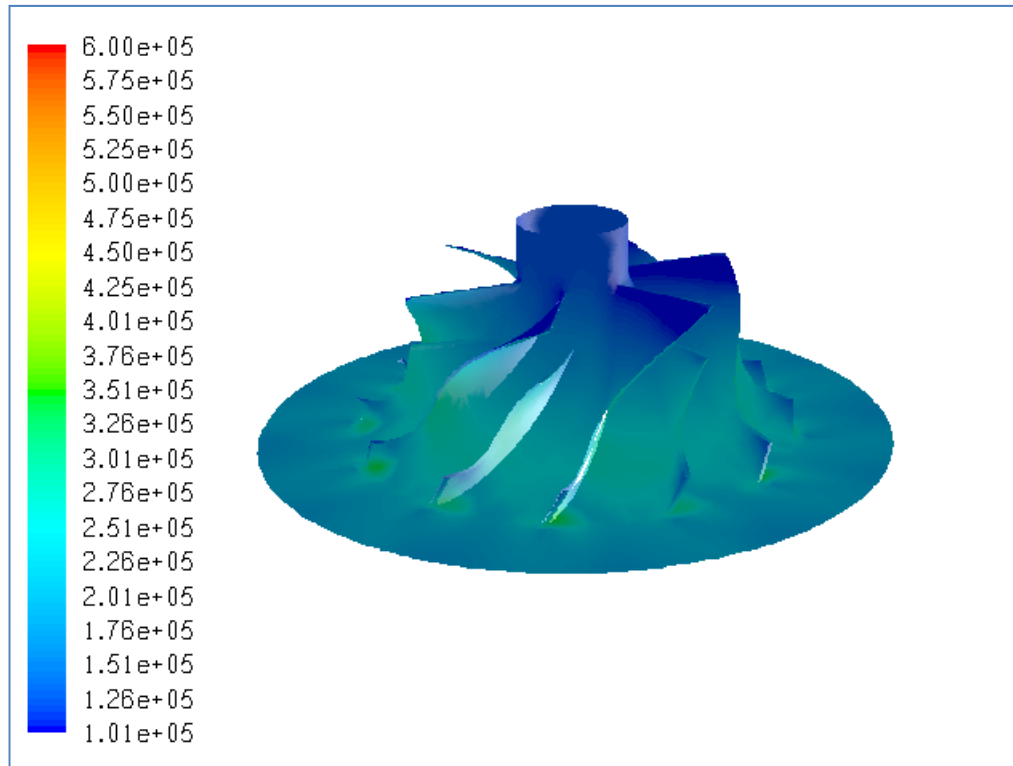


Figure B.32 Total Pressure Distribution (in Pa) for Case #31, Choked

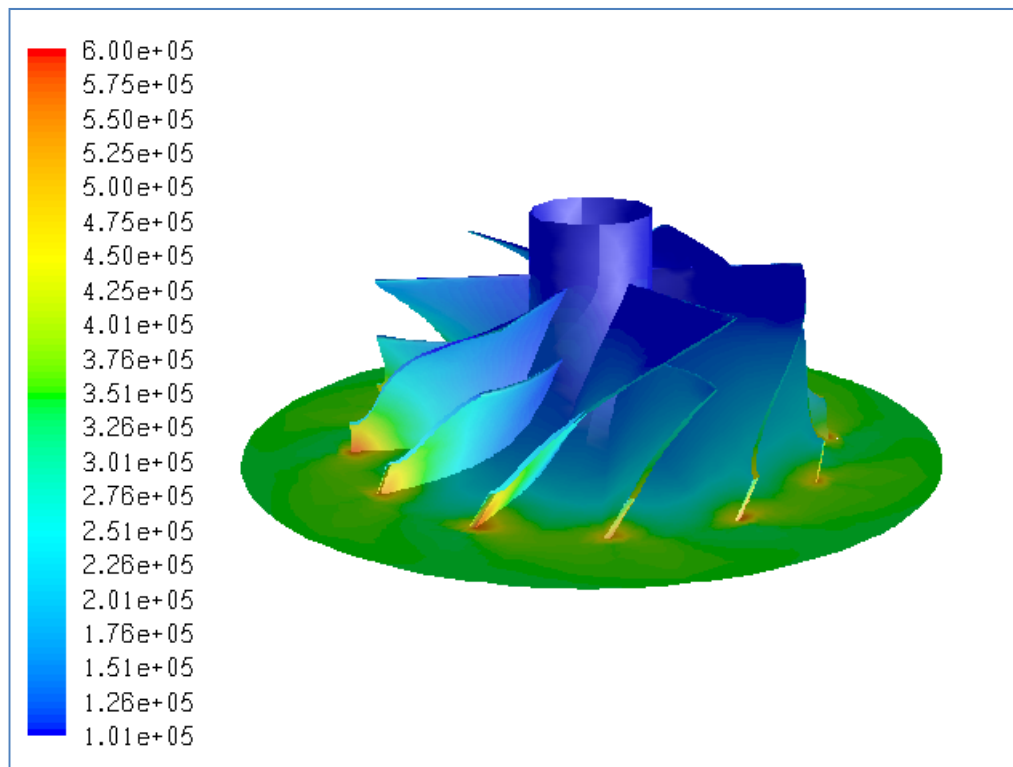


Figure B.33 Total Pressure Distribution (in Pa) for Case #32, PR=3.34

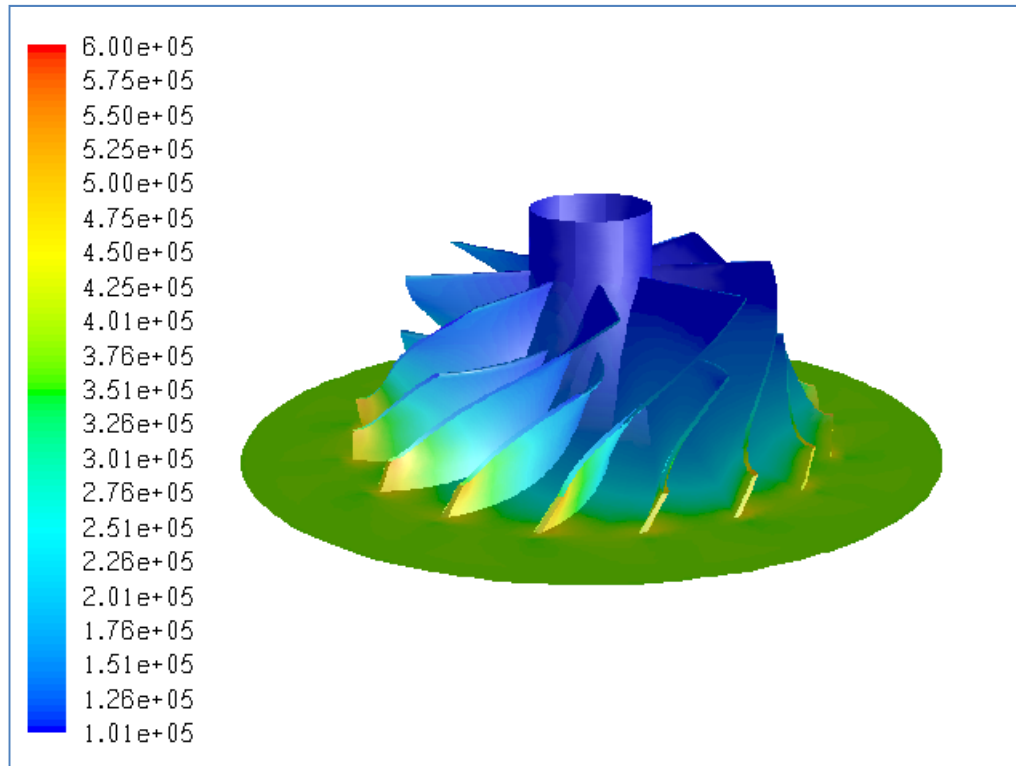


Figure B.34 Total Pressure Distribution (in Pa) for Case #33, PR=3.65

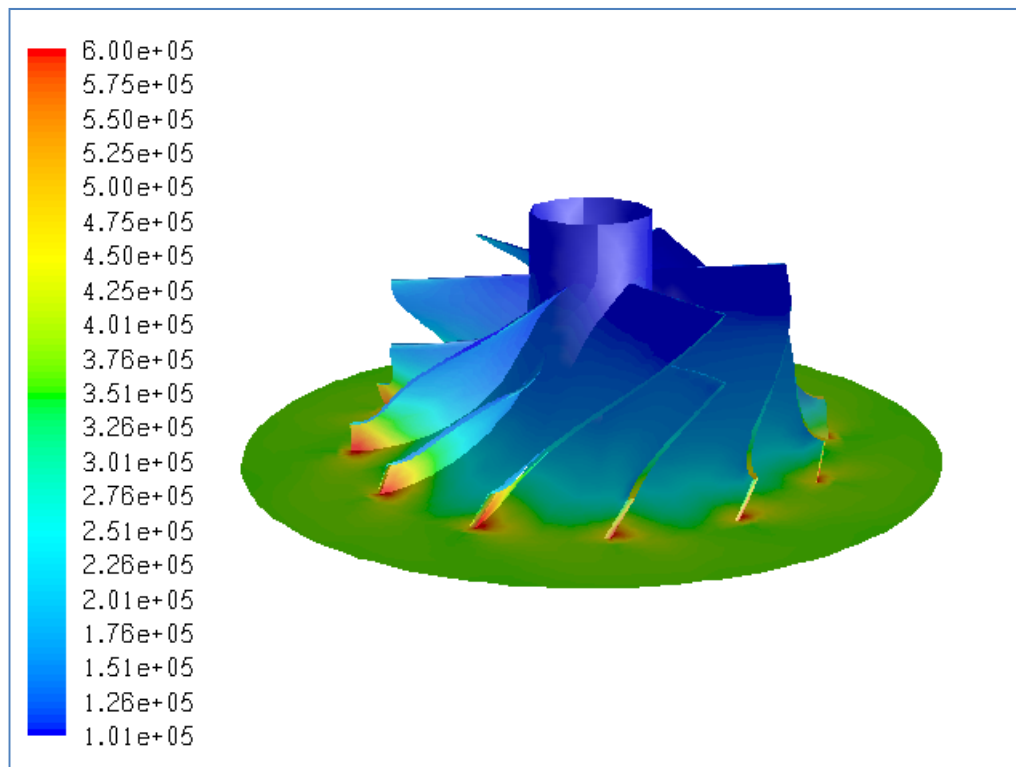


Figure B.35 Total Pressure Distribution (in Pa) for Case #34, PR=3.48

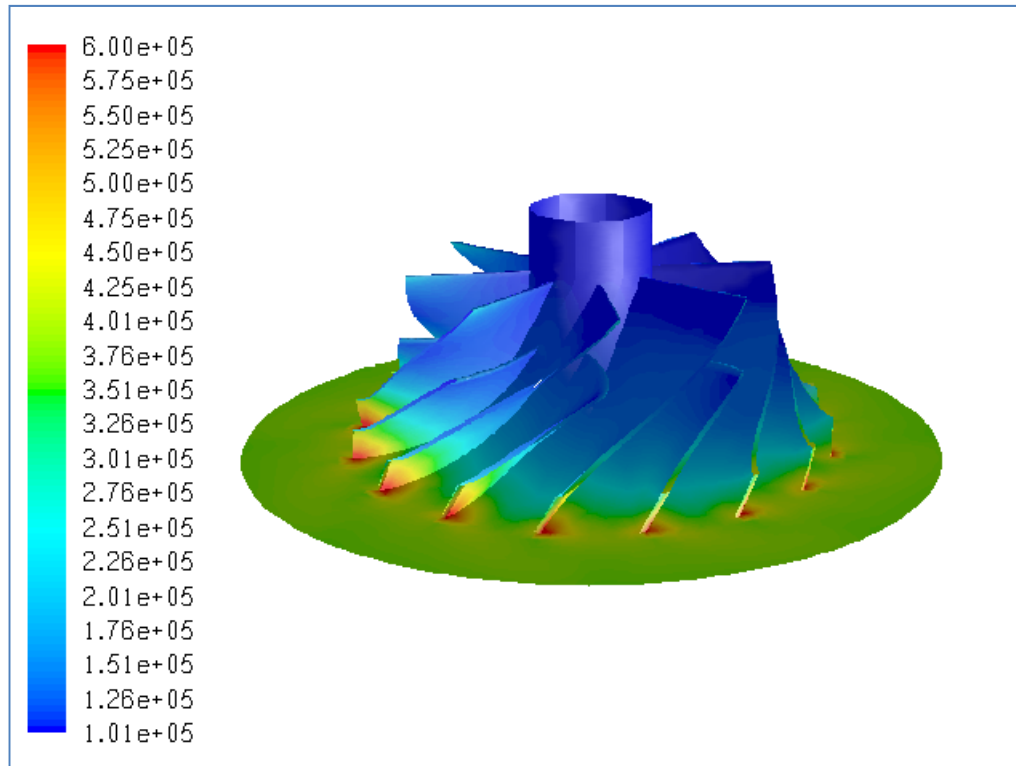


Figure B.36 Total Pressure Distribution (in Pa) for Case #35, PR=3.54

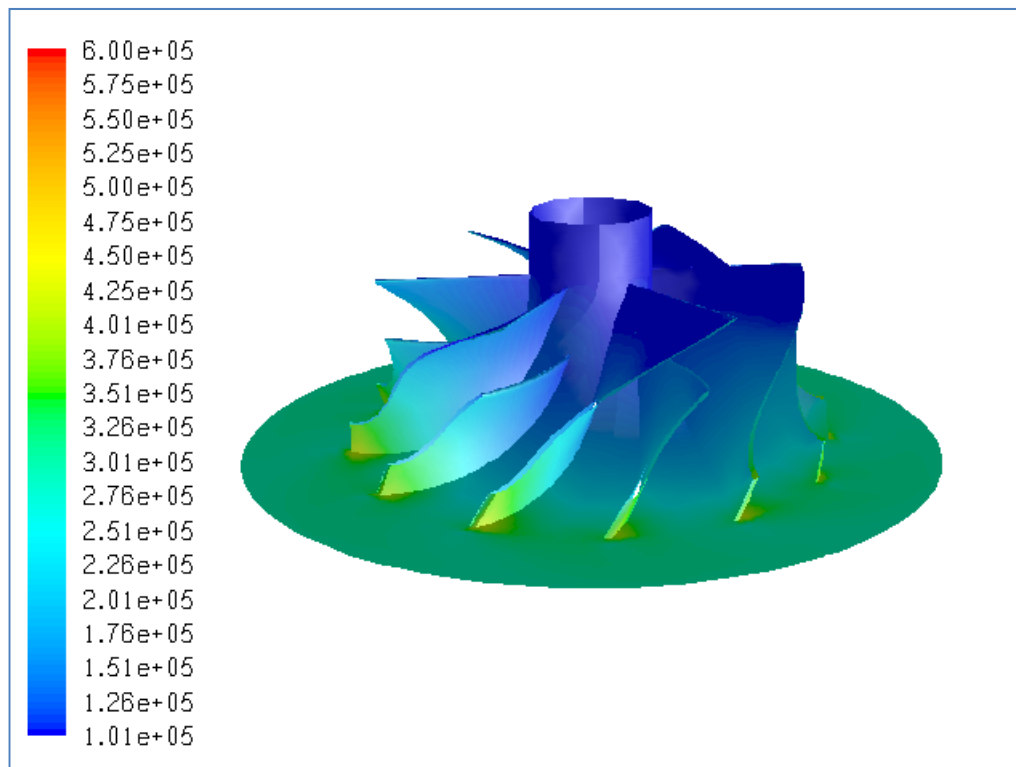


Figure B.37 Total Pressure Distribution (in Pa) for Case #36, PR=2.87

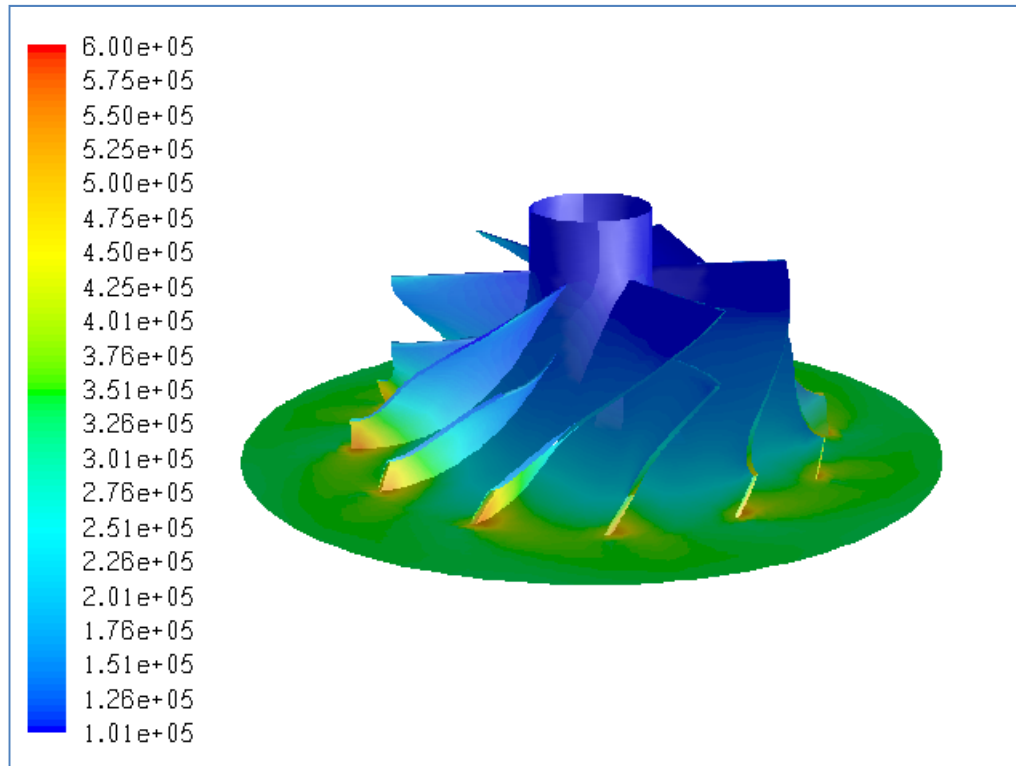


Figure B.38 Total Pressure Distribution (in Pa) for Case #37, PR=3.26

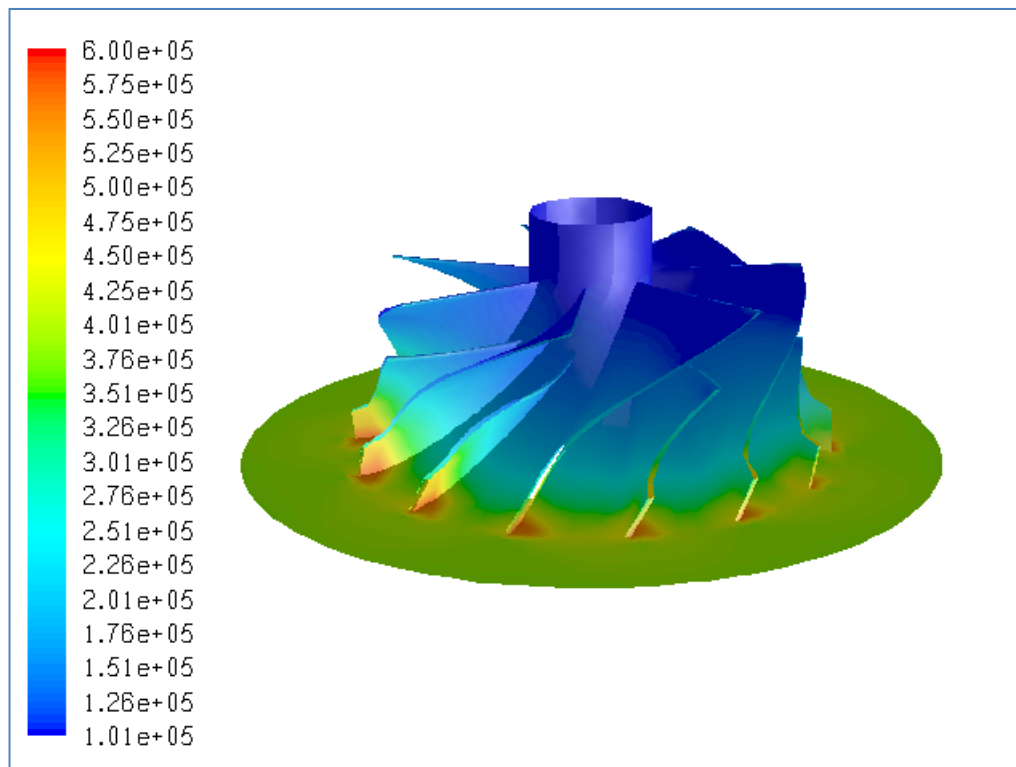


Figure B.39 Total Pressure Distribution (in Pa) for Case #38, PR=3.71

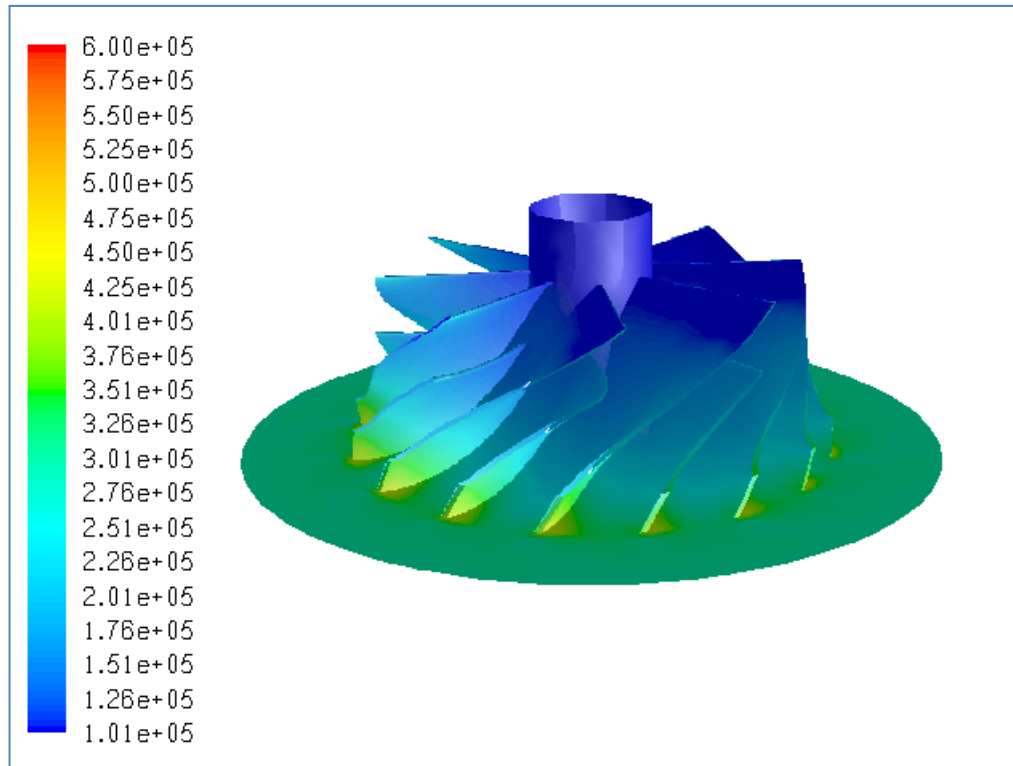


Figure B.40 Total Pressure Distribution (in Pa) for Case #39, PR=2.85

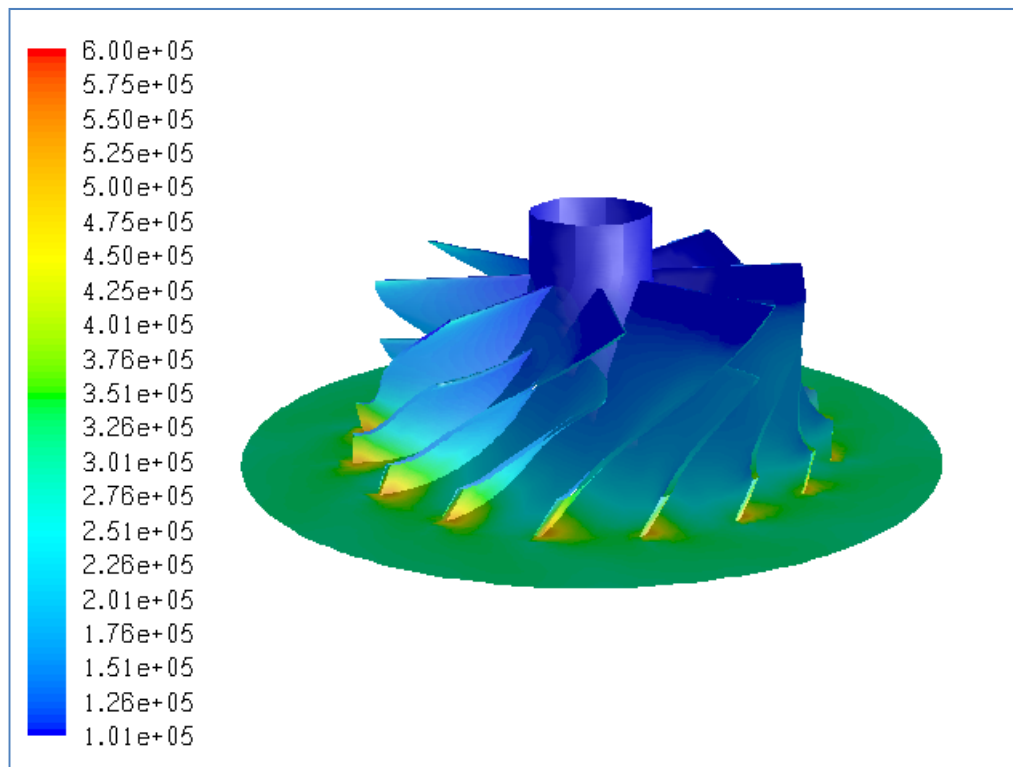


Figure B.41 Total Pressure Distribution (in Pa) for Case #40, PR=2.95

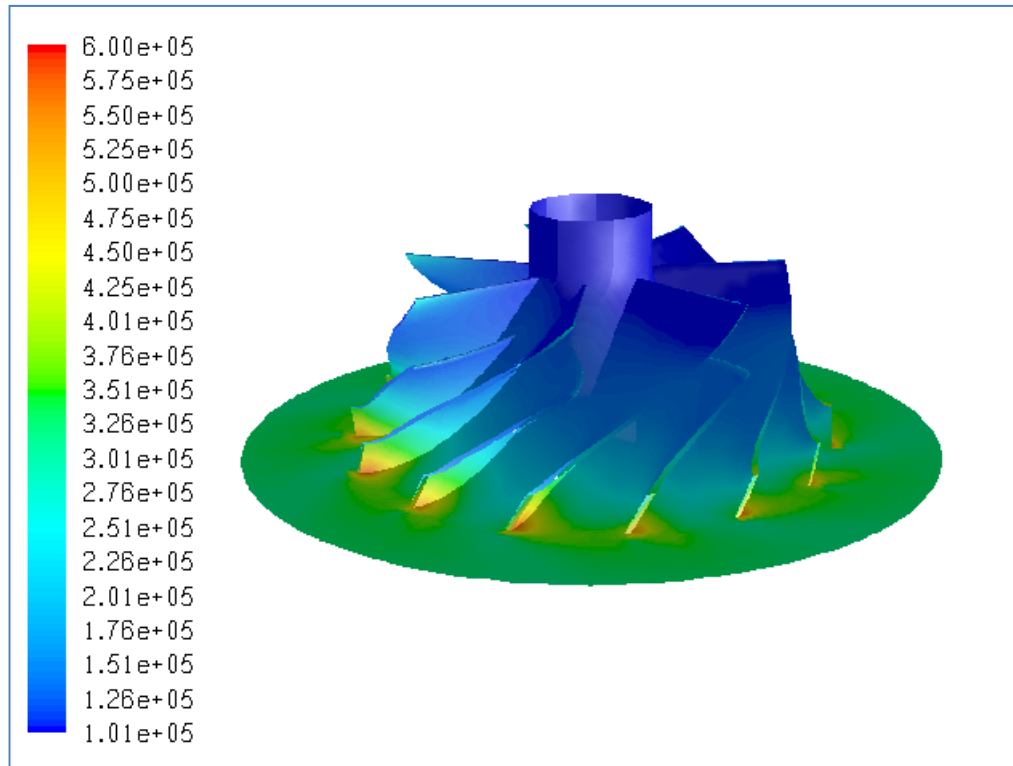


Figure B.42 Total Pressure Distribution (in Pa) for Case #41, PR=3.04

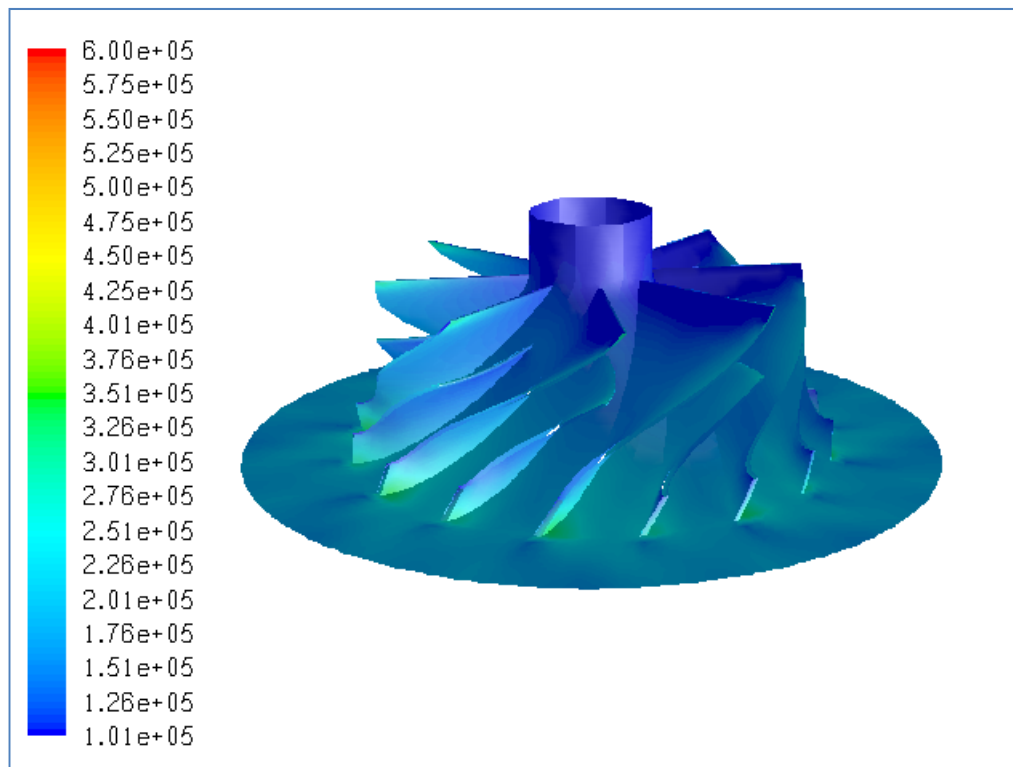


Figure B.43 Total Pressure Distribution (in Pa) for Case #42, Choked

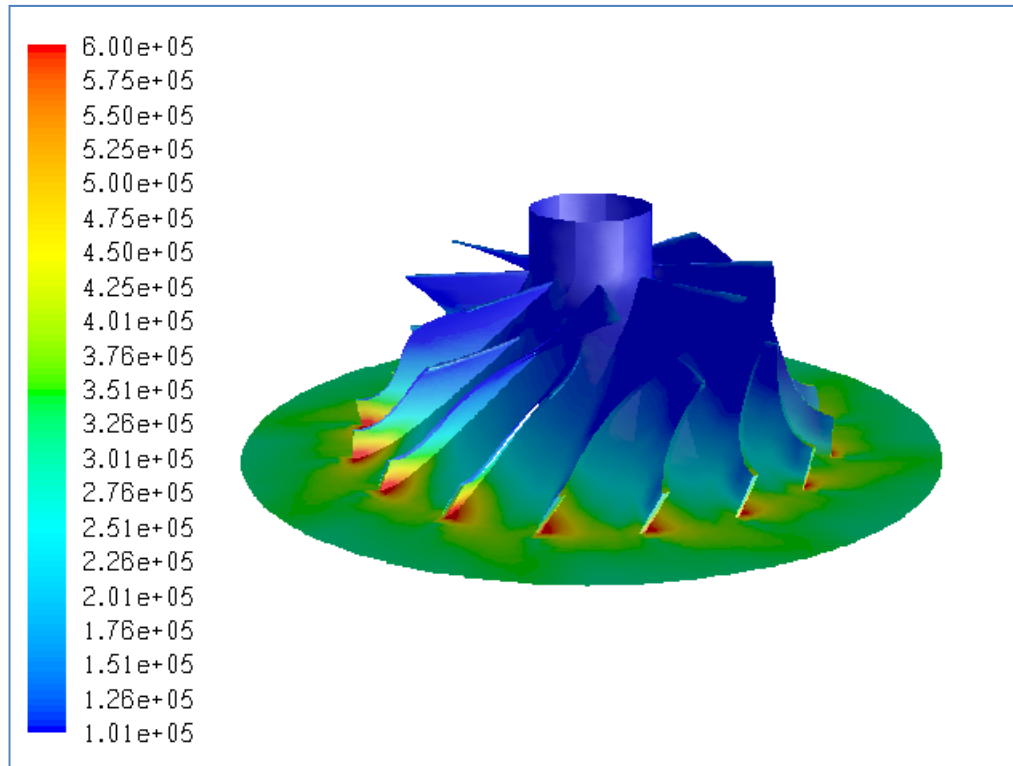


Figure B.44 Total Pressure Distribution (in Pa) for Case #43, Choked

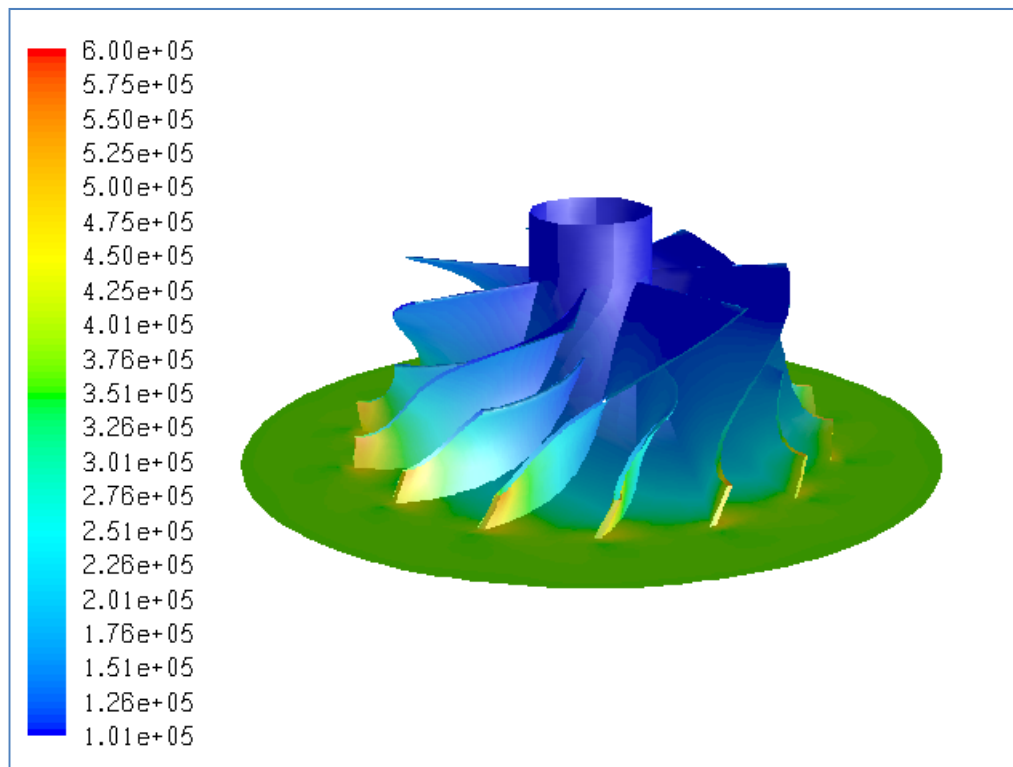


Figure B.45 Total Pressure Distribution (in Pa) for Case #44, PR=3.57

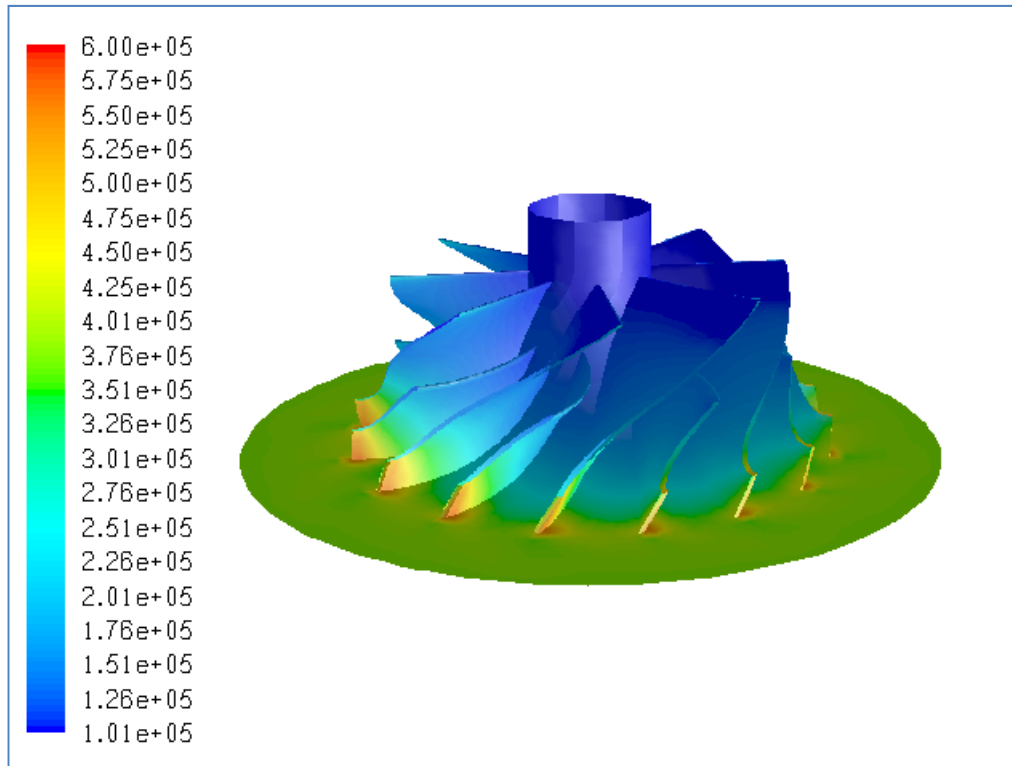


Figure B.46 Total Pressure Distribution (in Pa) for Case #45, PR=3.66

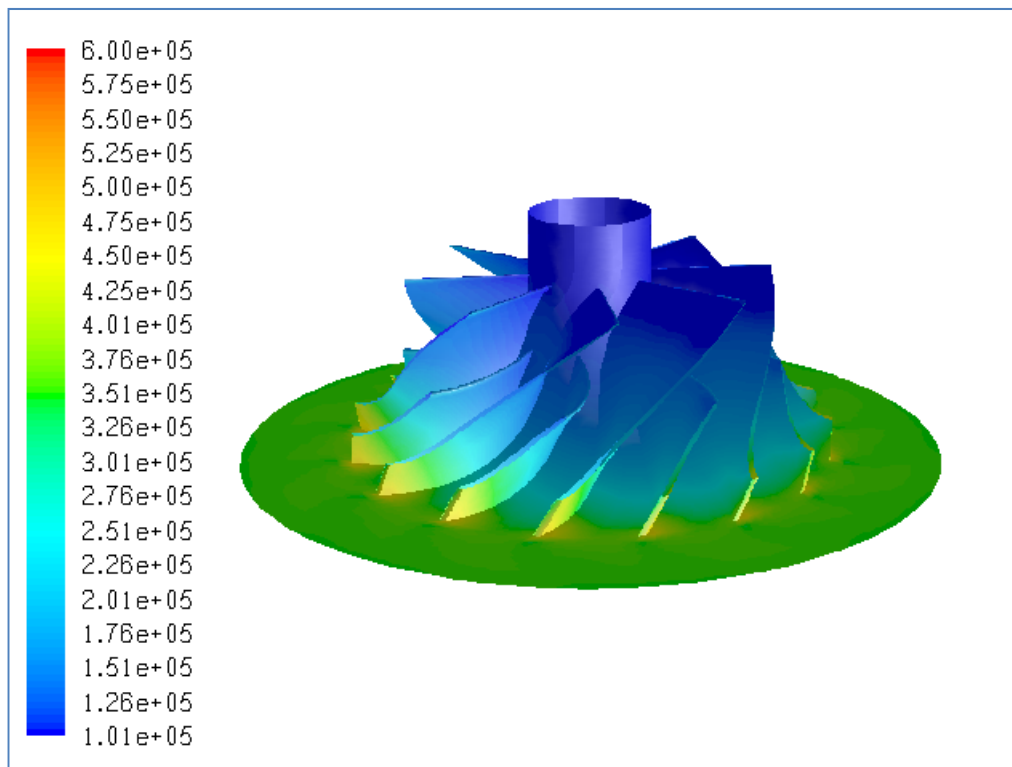


Figure B.47 Total Pressure Distribution (in Pa) for Case #46, PR=3.41

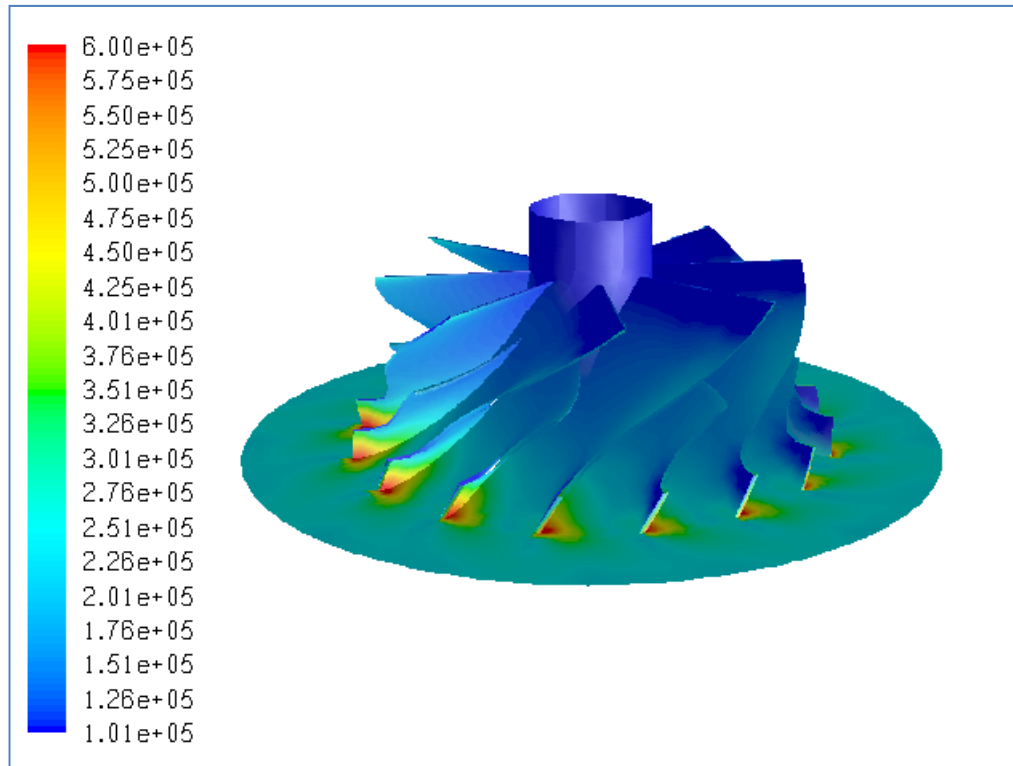


Figure B.48 Total Pressure Distribution (in Pa) for Case #47, PR=1.92

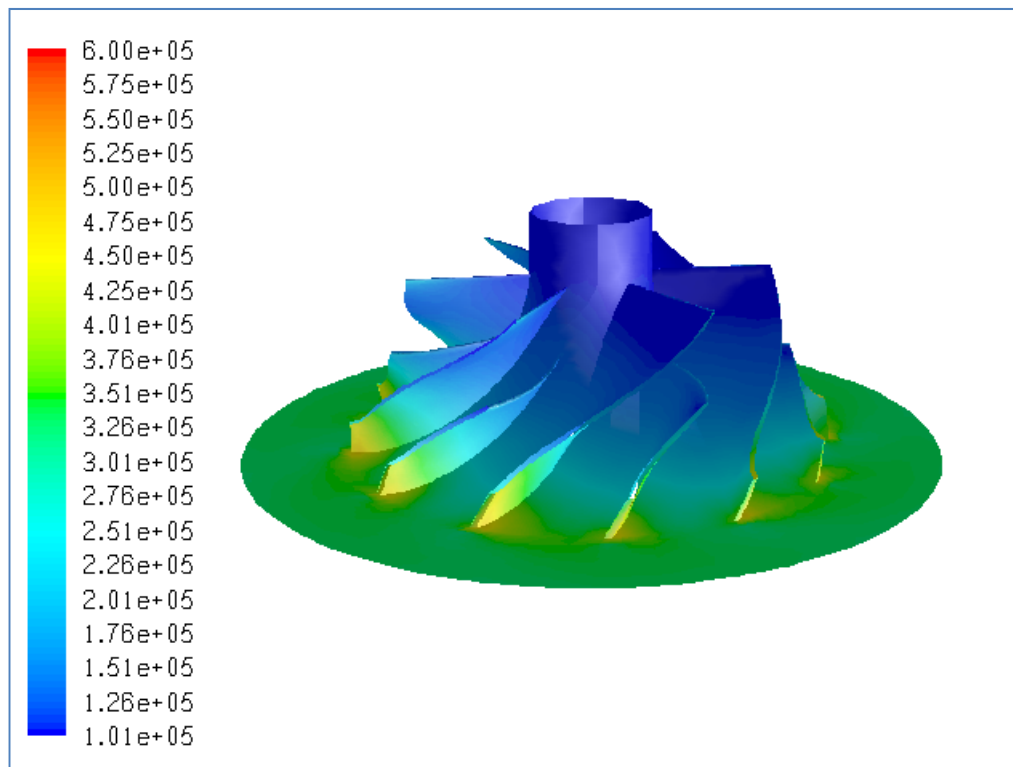


Figure B.49 Total Pressure Distribution (in Pa) for Case #48, PR=3.19

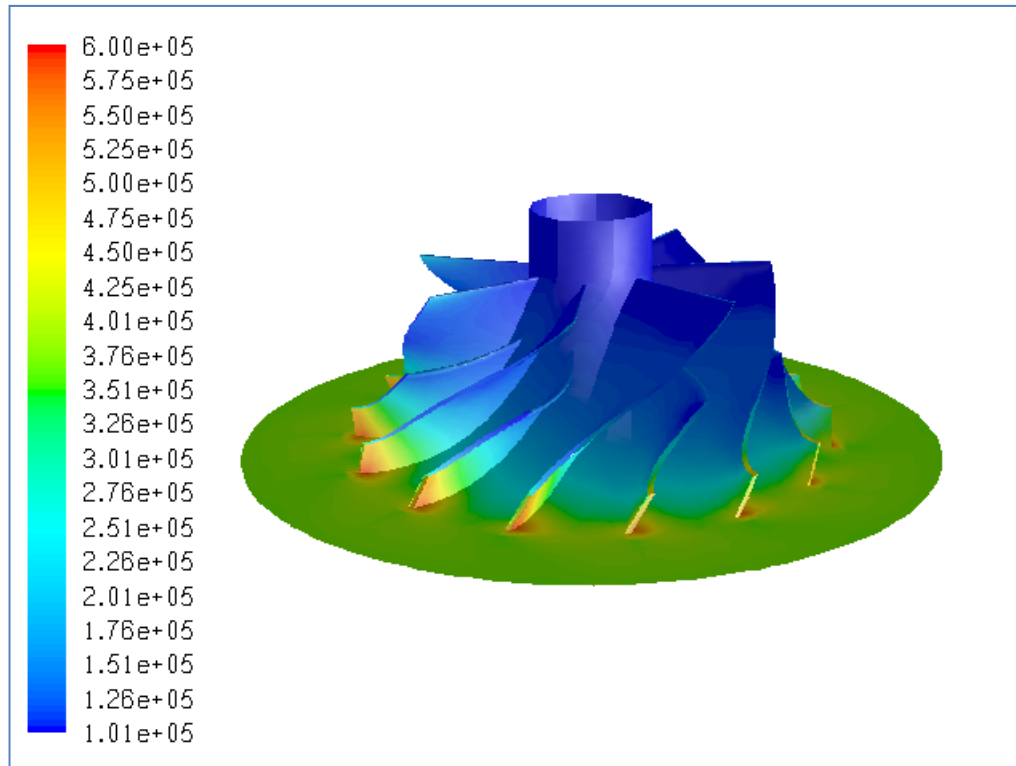


Figure B.50 Total Pressure Distribution (in Pa) for Case #49, PR=3.57

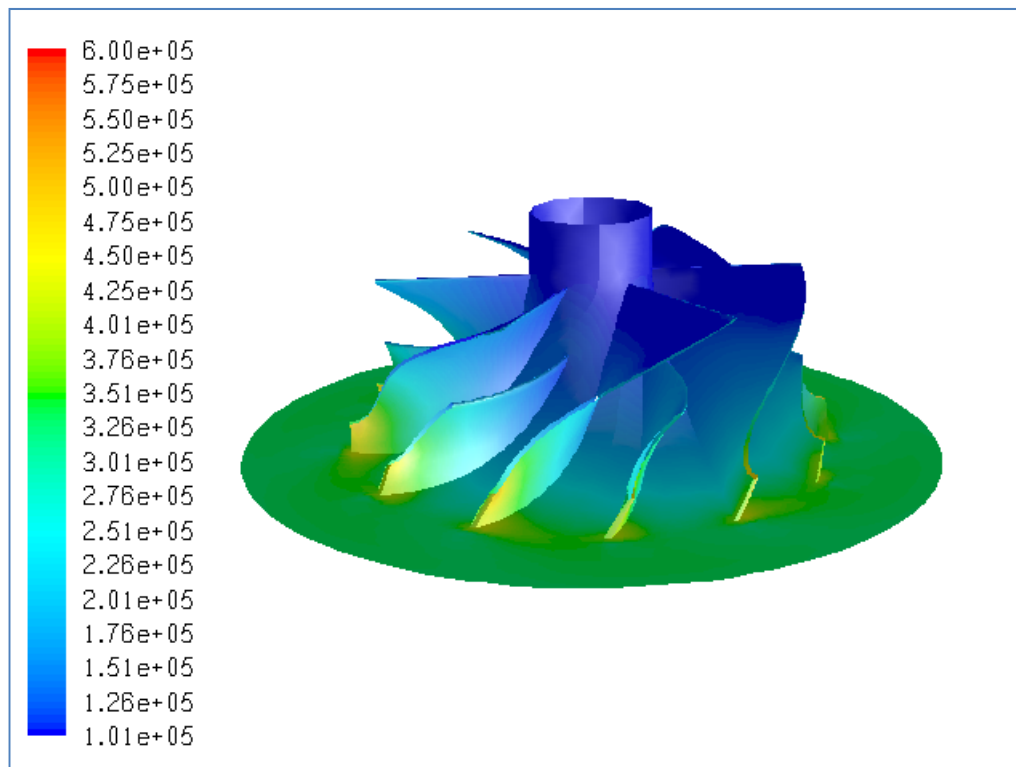


Figure B.51 Total Pressure Distribution (in Pa) for Case #50, PR=3.24

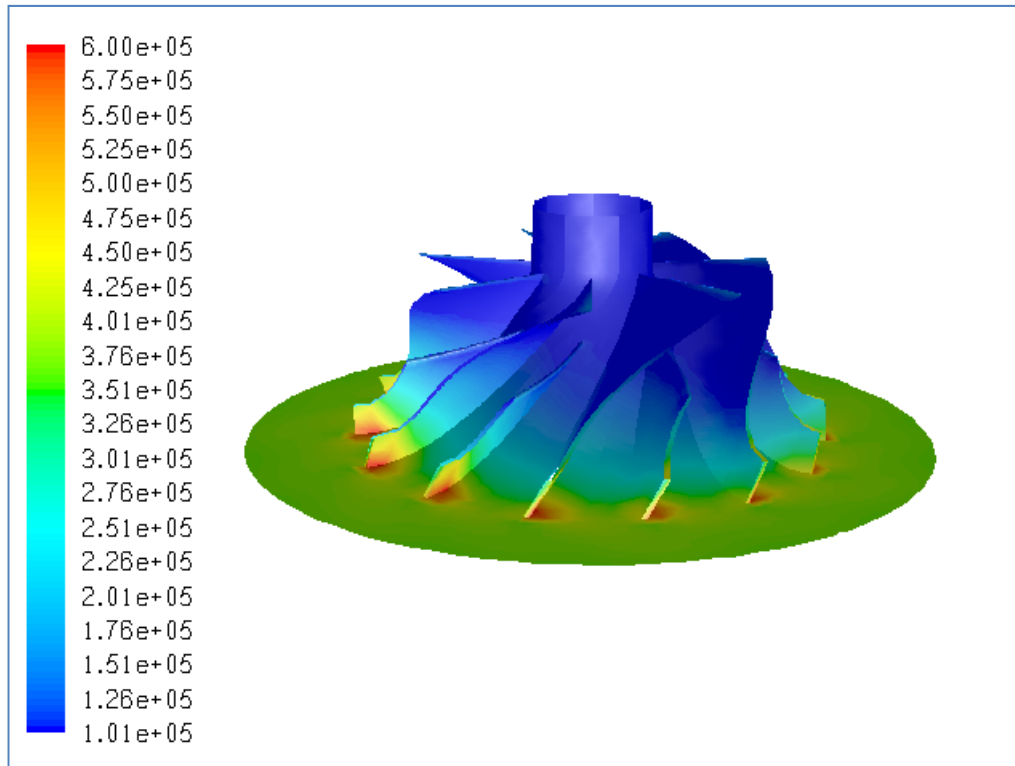


Figure B.52 Total Pressure Distribution (in Pa) for Case #51, PR=3.54

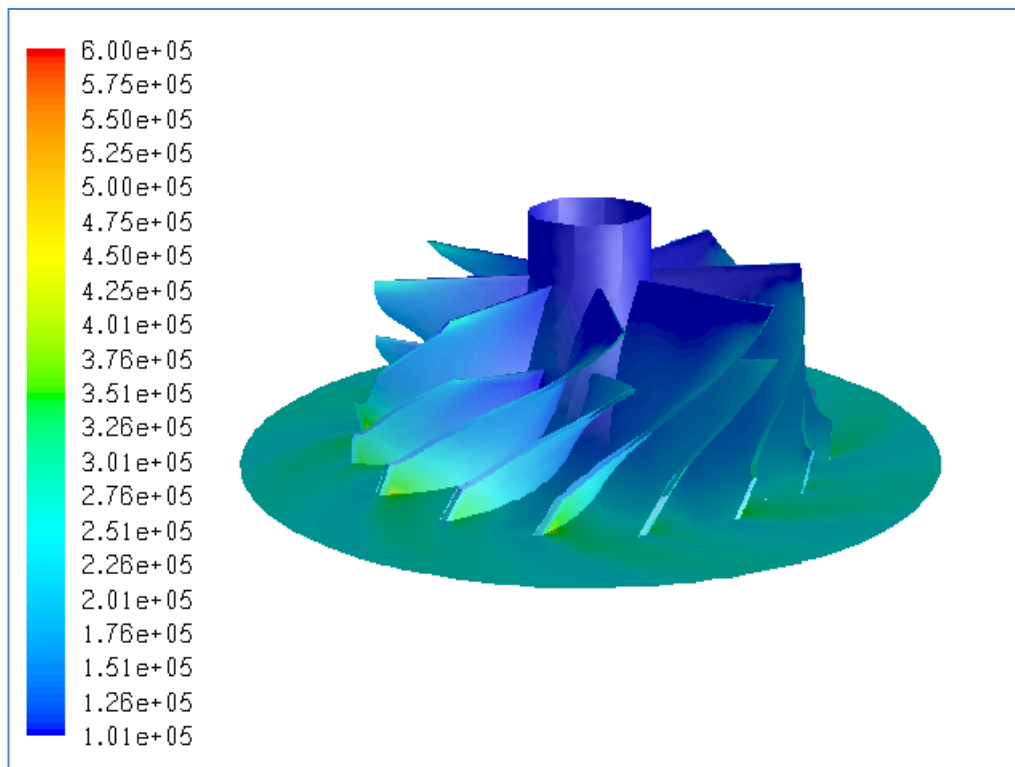


Figure B.53 Total Pressure Distribution (in Pa) for Case #52, PR=2.48

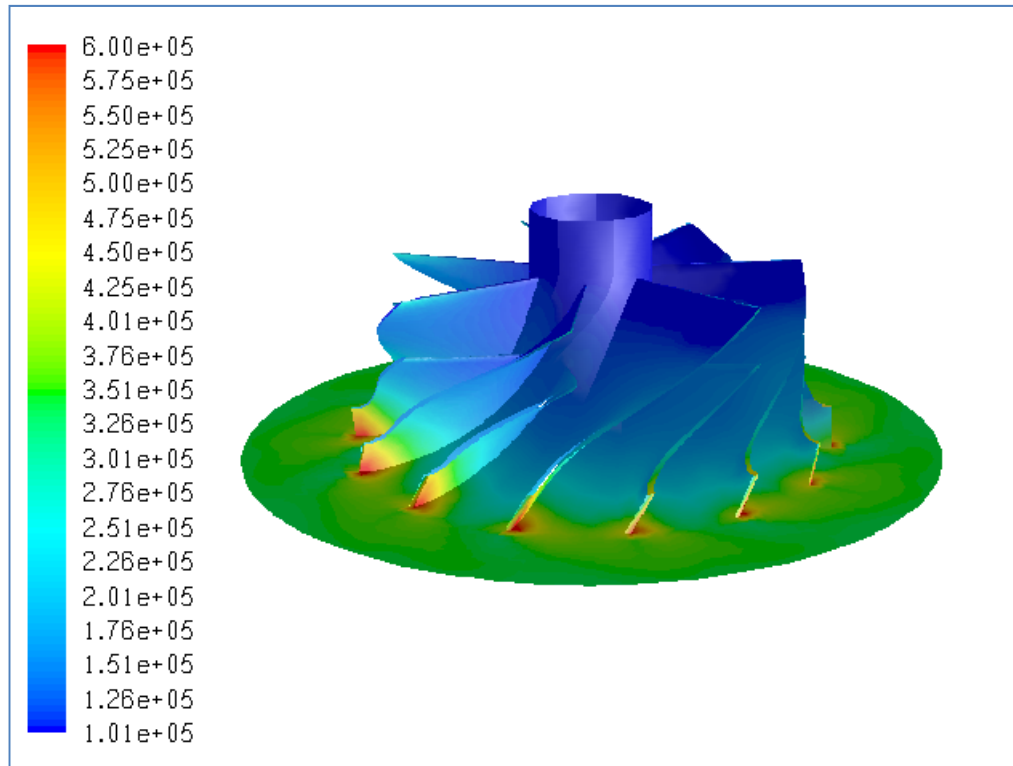


Figure B.54 Total Pressure Distribution (in Pa) for Case #53, PR=3.24

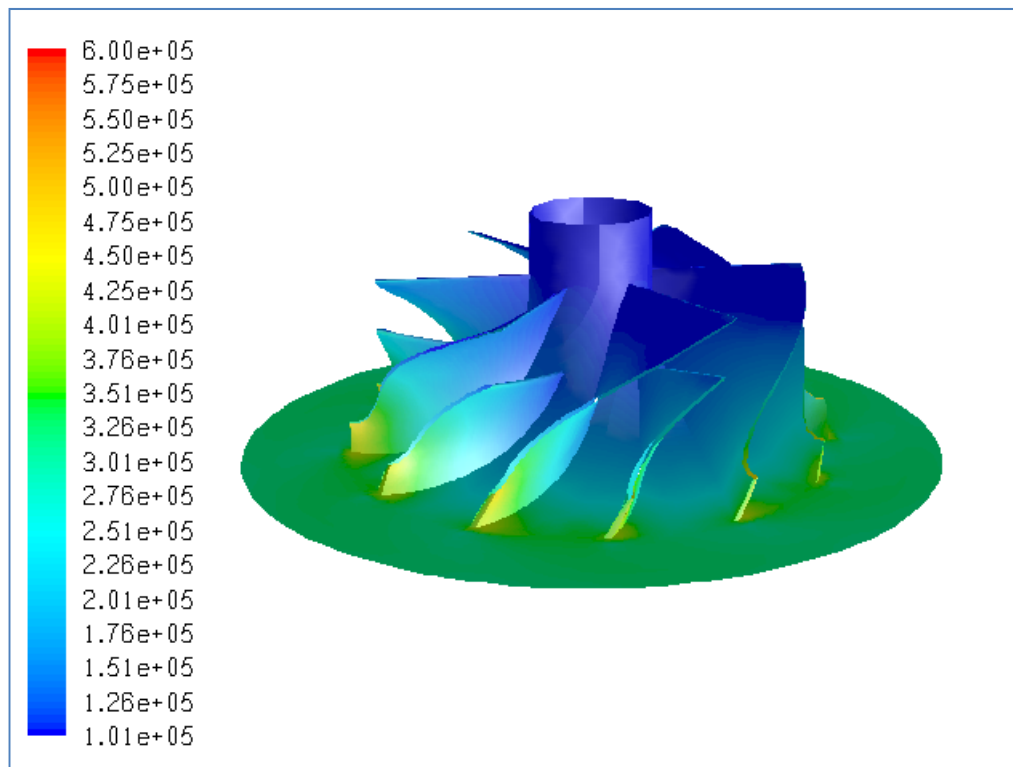


Figure B.55 Total Pressure Distribution (in Pa) for Case #54, PR=3.11

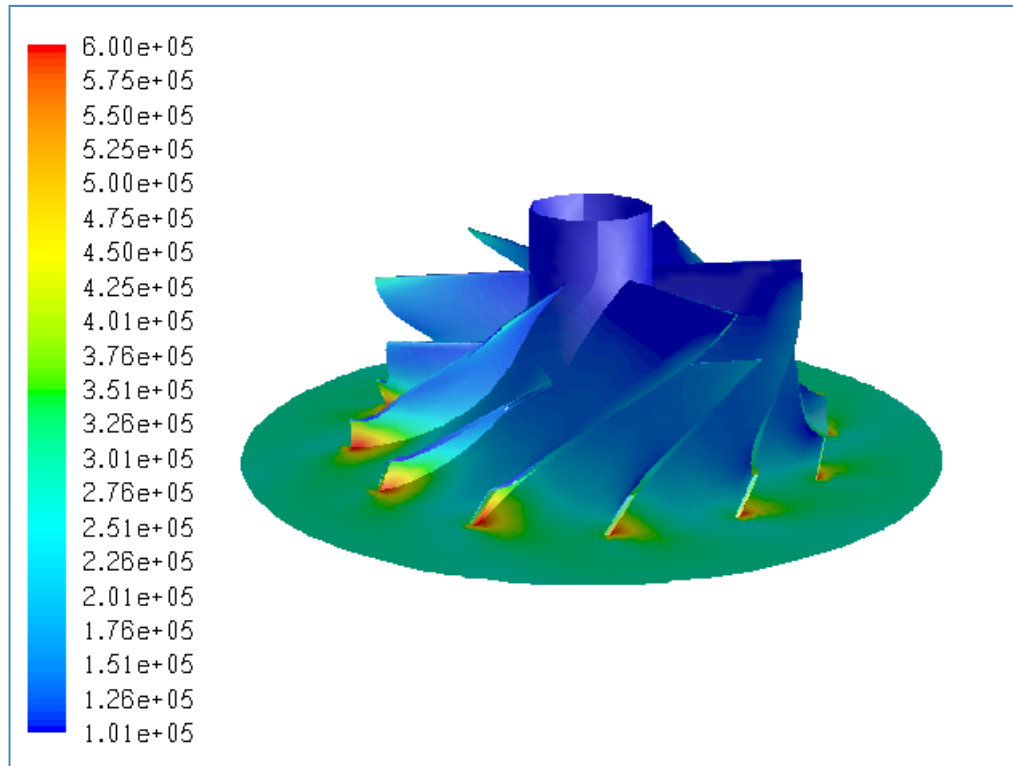


Figure B.56 Total Pressure Distribution (in Pa) for Case #55, PR=2.67

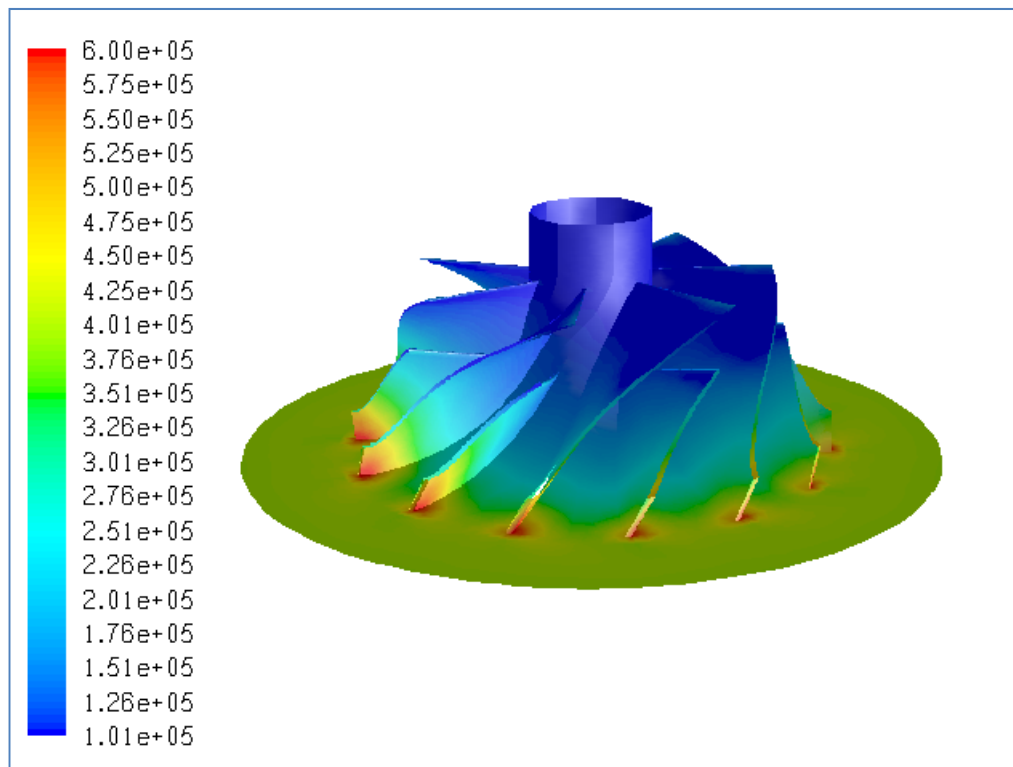


Figure B.57 Total Pressure Distribution (in Pa) for Case #56, PR=3.86

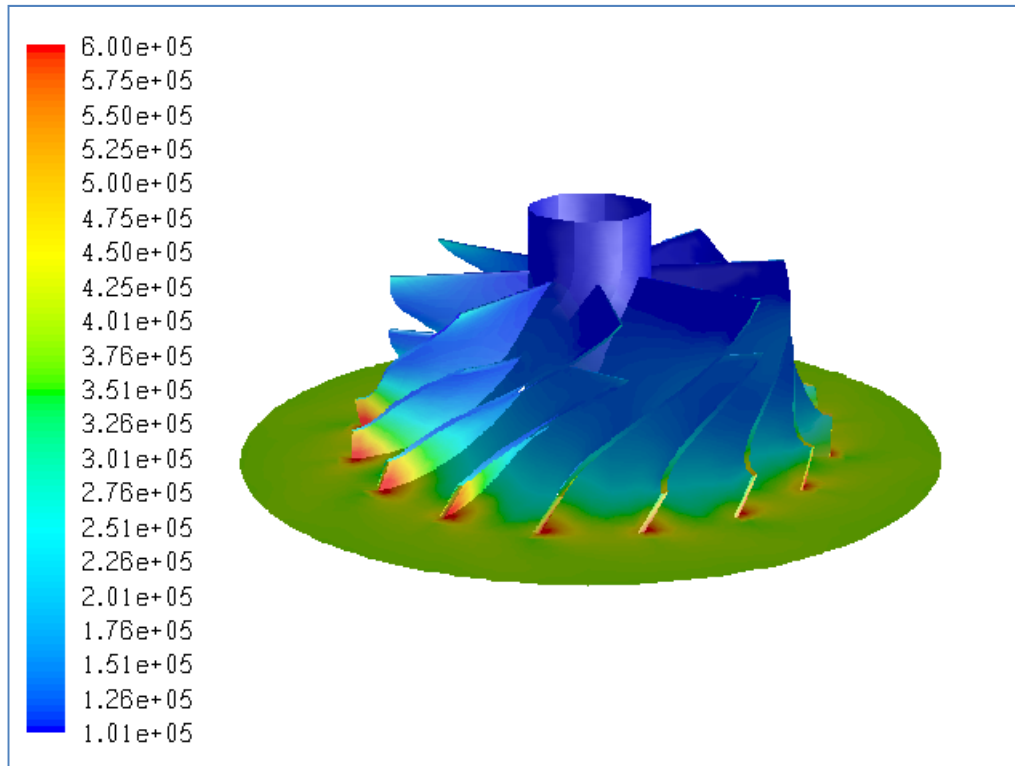


Figure B.58 Total Pressure Distribution (in Pa) for Case #57, PR=3.59

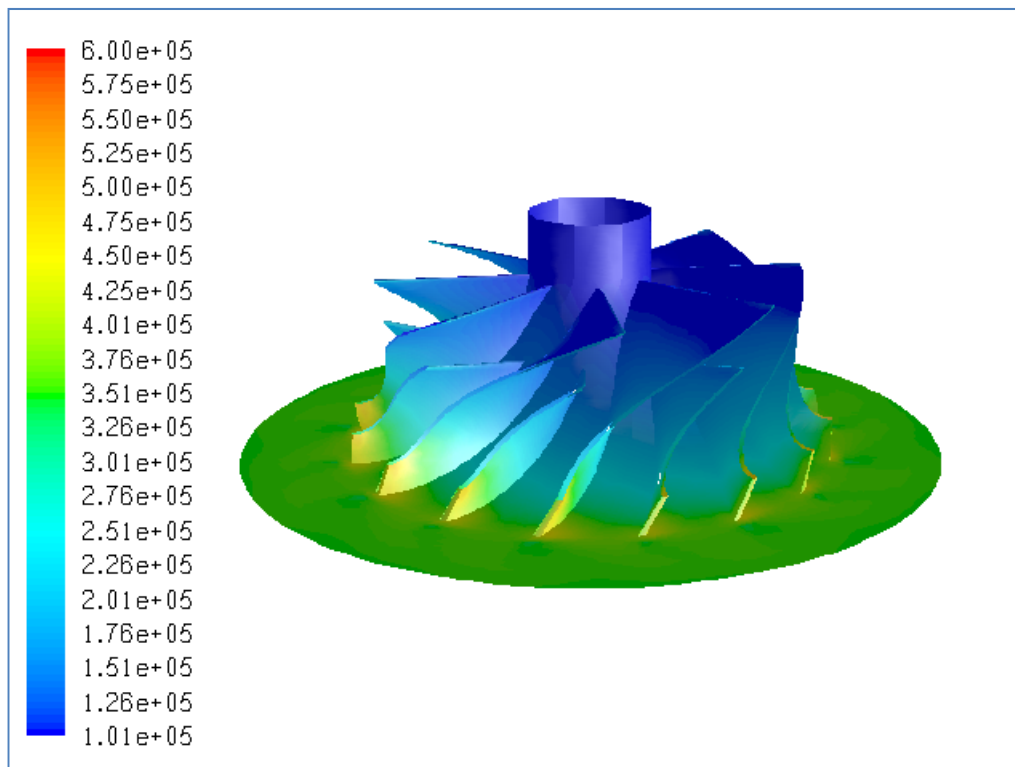


Figure B.59 Total Pressure Distribution (in Pa) for Case #58, PR=3.40

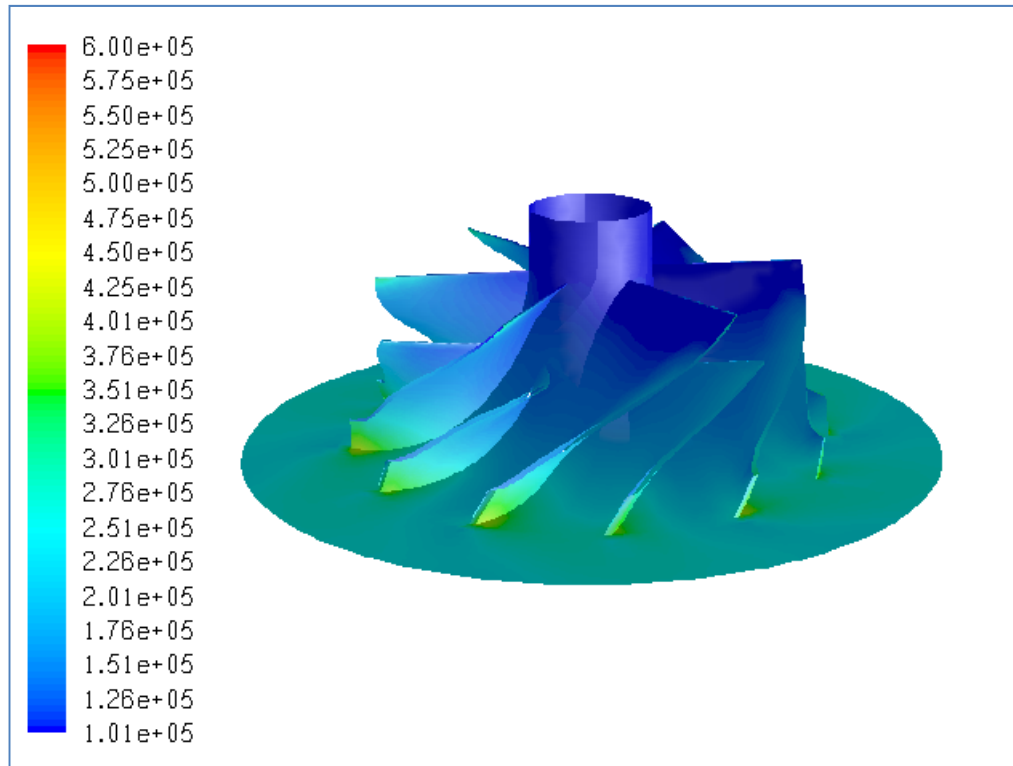


Figure B.60 Total Pressure Distribution (in Pa) for Case #59, PR=2.37

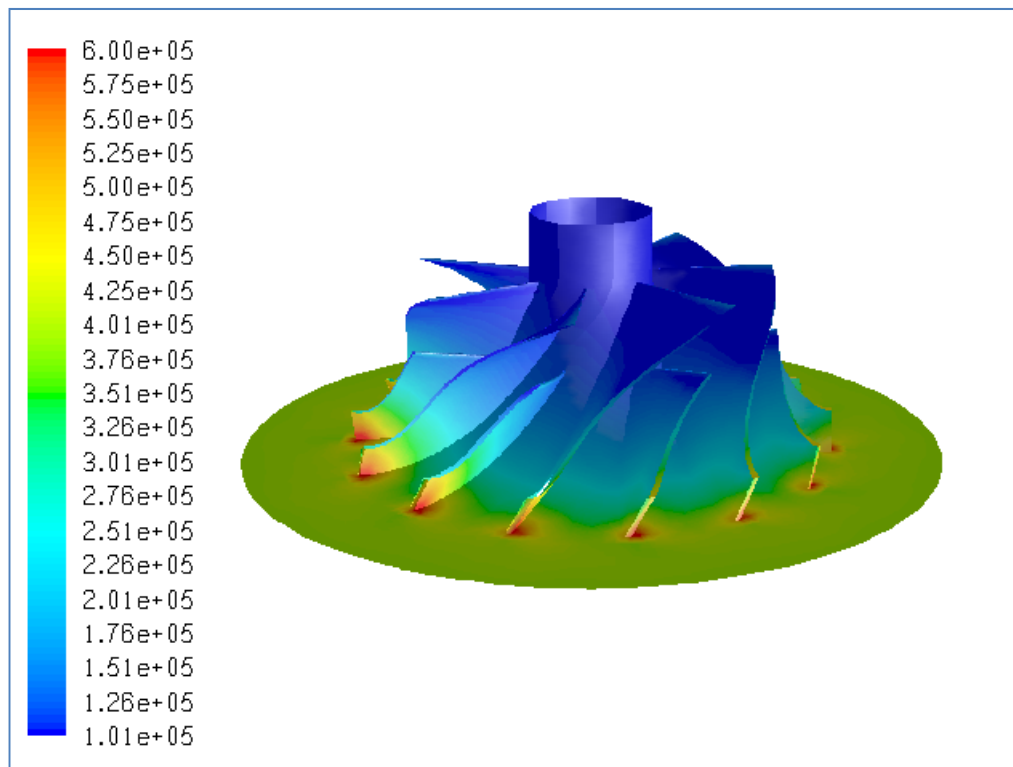


Figure B.61 Total Pressure Distribution (in Pa) for Case #60, PR=3.79

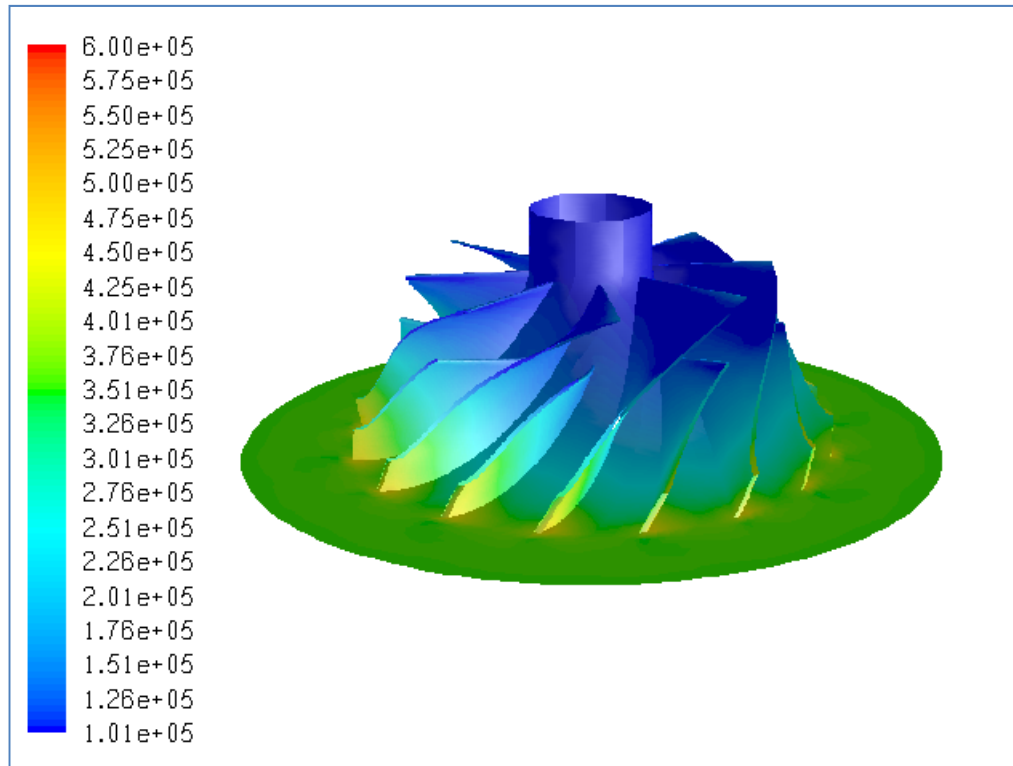


Figure B.62 Total Pressure Distribution (in Pa) for Case #61, PR=3.46

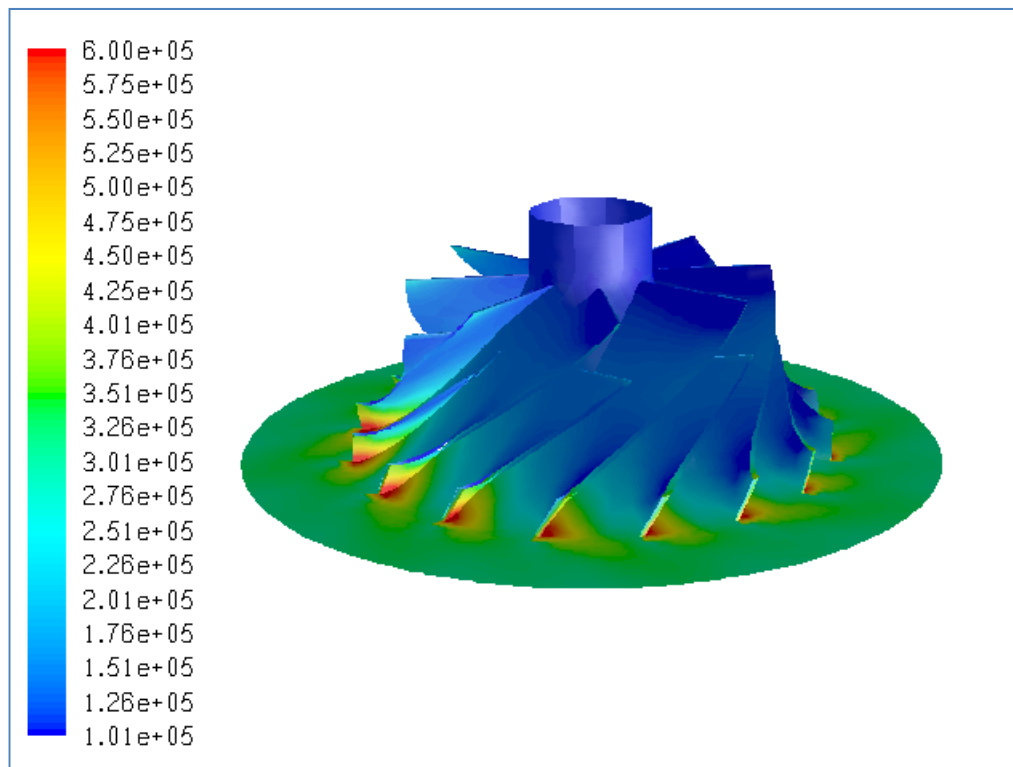


Figure B.63 Total Pressure Distribution (in Pa) for Case #62, Choked

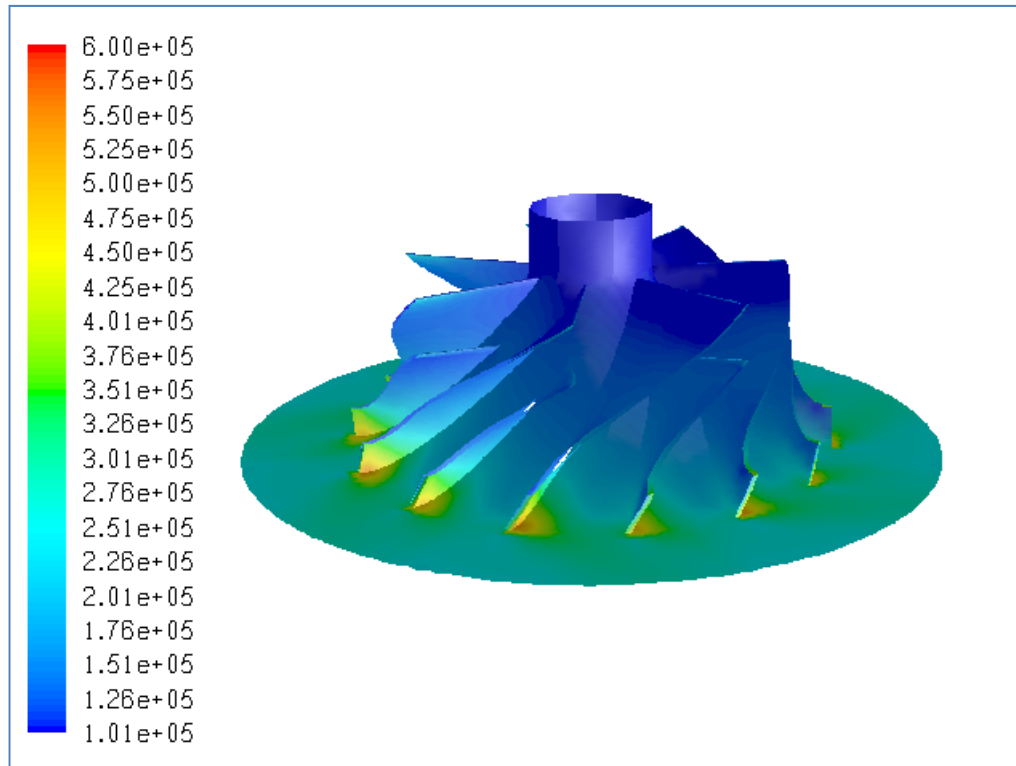


Figure B.64 Total Pressure Distribution (in Pa) for Case #63, PR=2.18

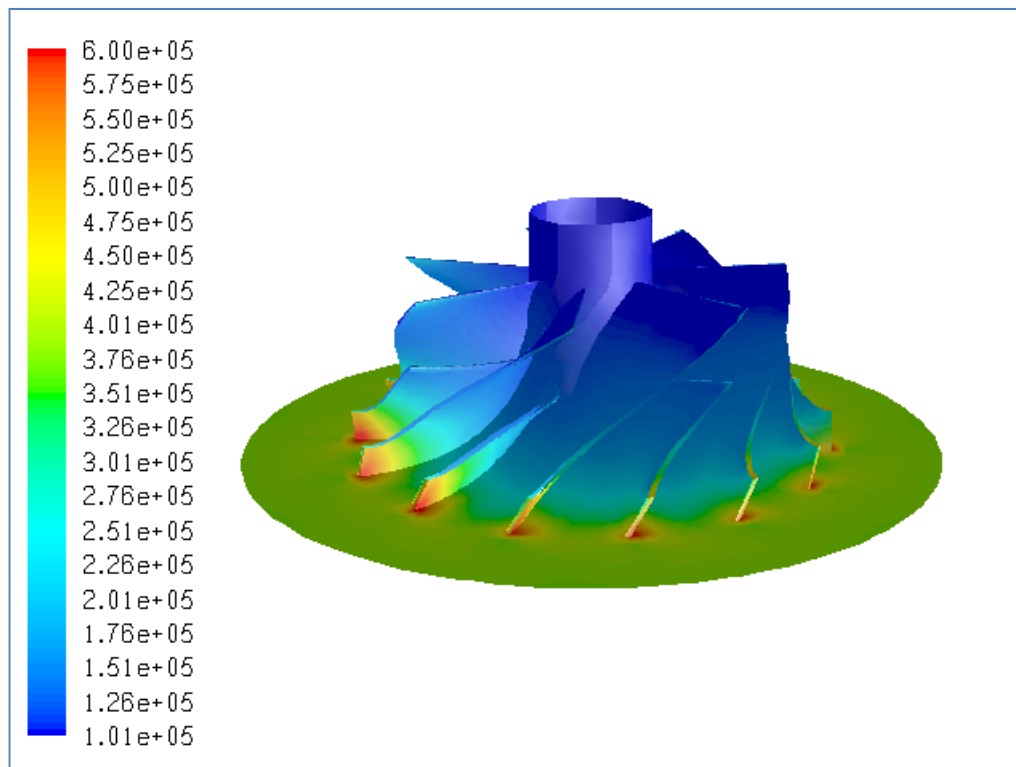


Figure B.65 Total Pressure Distribution (in Pa) for Case #64, PR=3.68

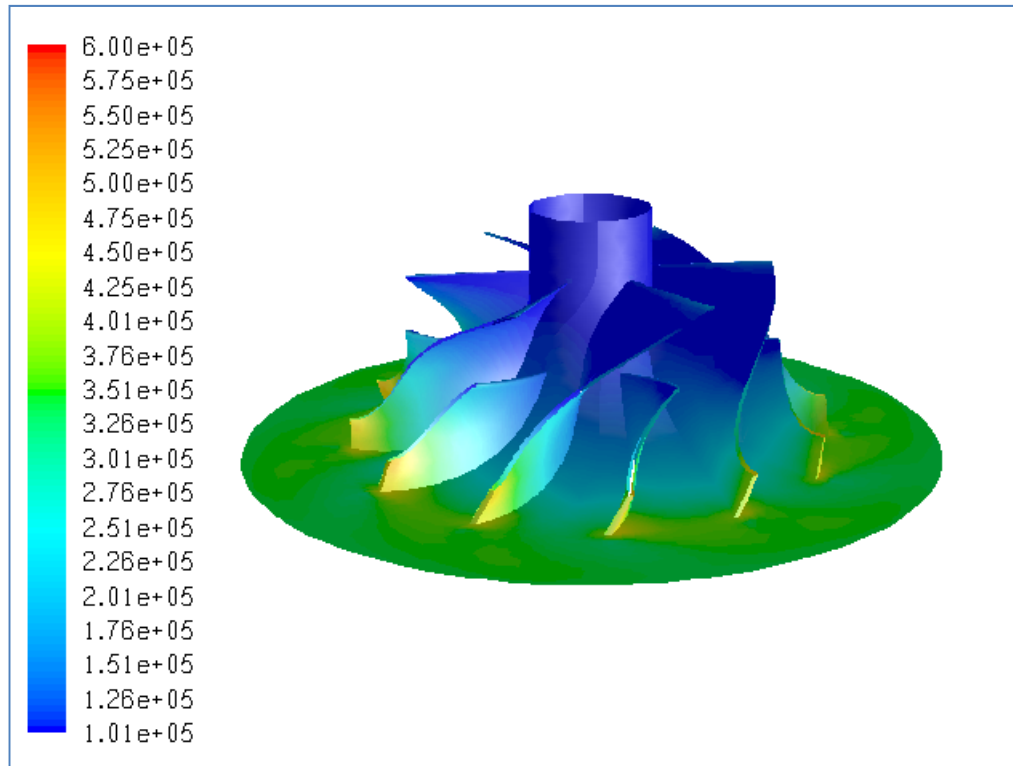


Figure B.66 Total Pressure Distribution (in Pa) for Case #65, PR=3.36

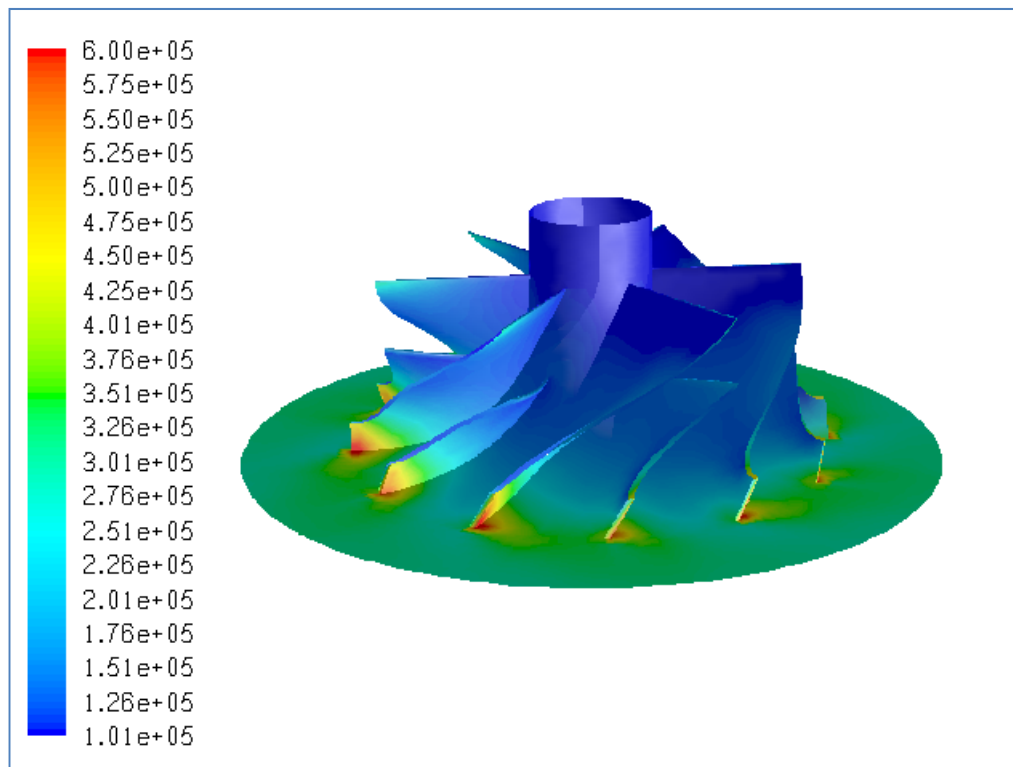


Figure B.67 Total Pressure Distribution (in Pa) for Case #66, PR=2.86

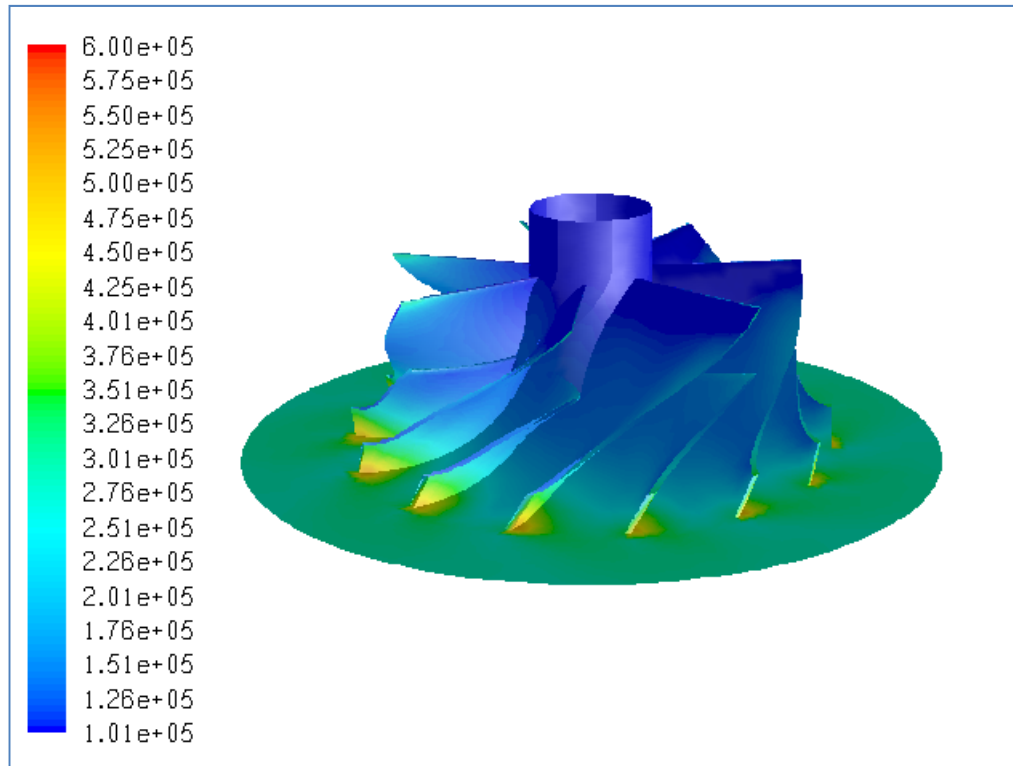


Figure B.68 Total Pressure Distribution (in Pa) for Case #67, PR=2.70

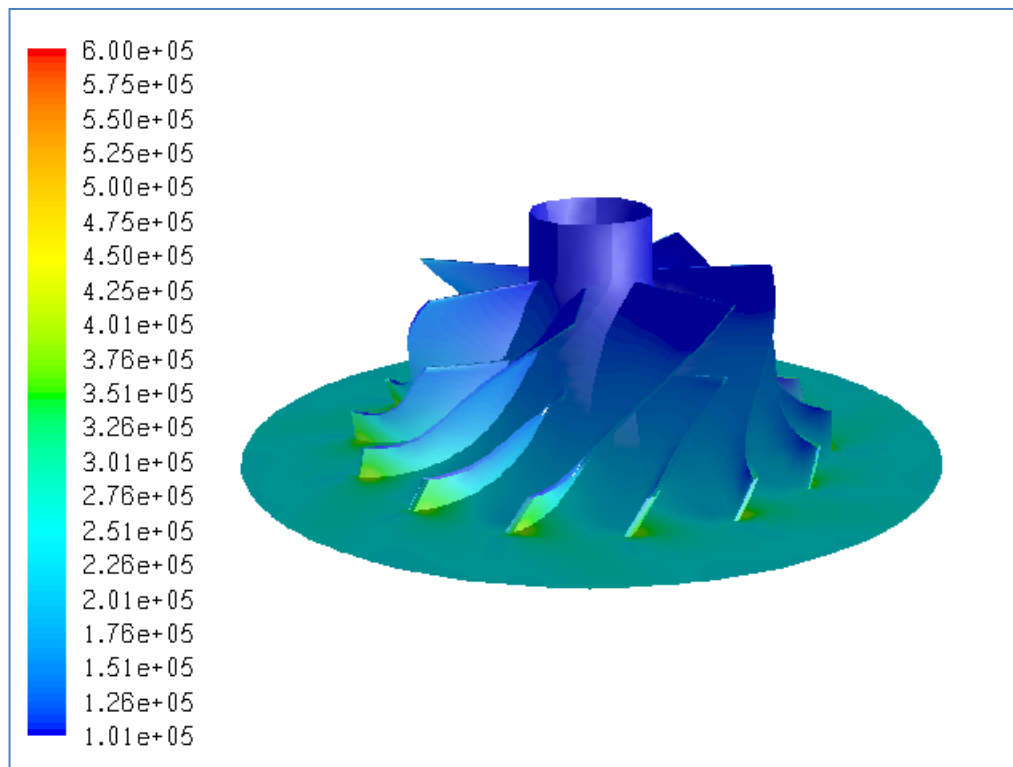


Figure B.69 Total Pressure Distribution (in Pa) for Case #68, PR=2.23

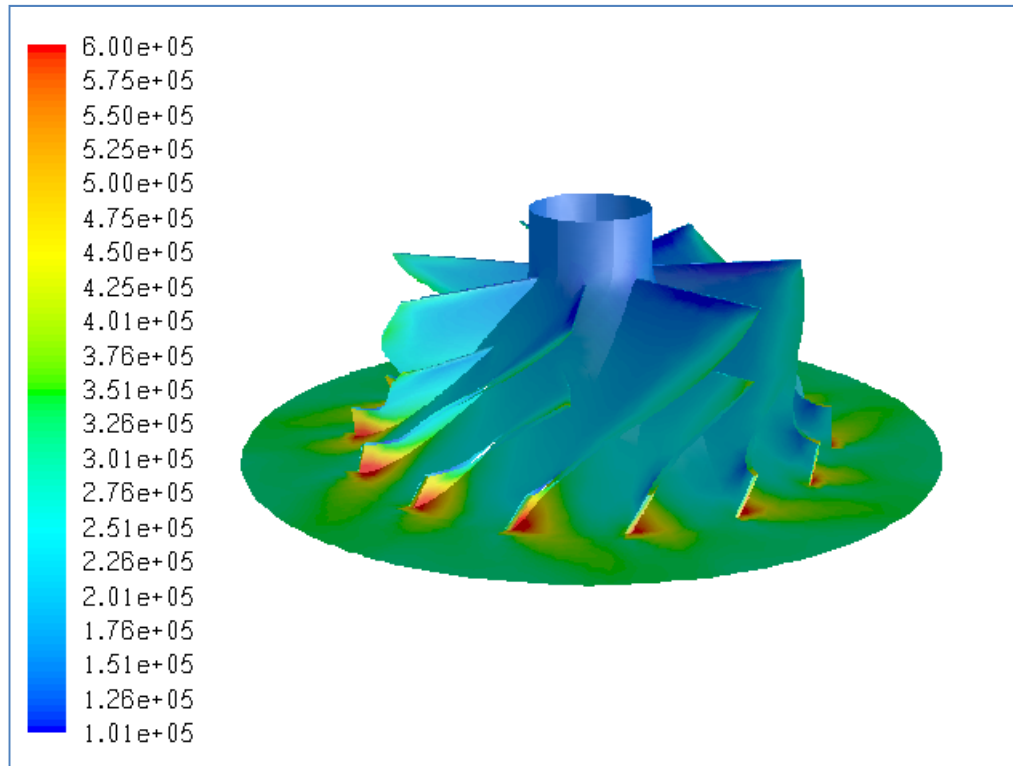


Figure B.70 Total Pressure Distribution (in Pa) for Case #69, Choked

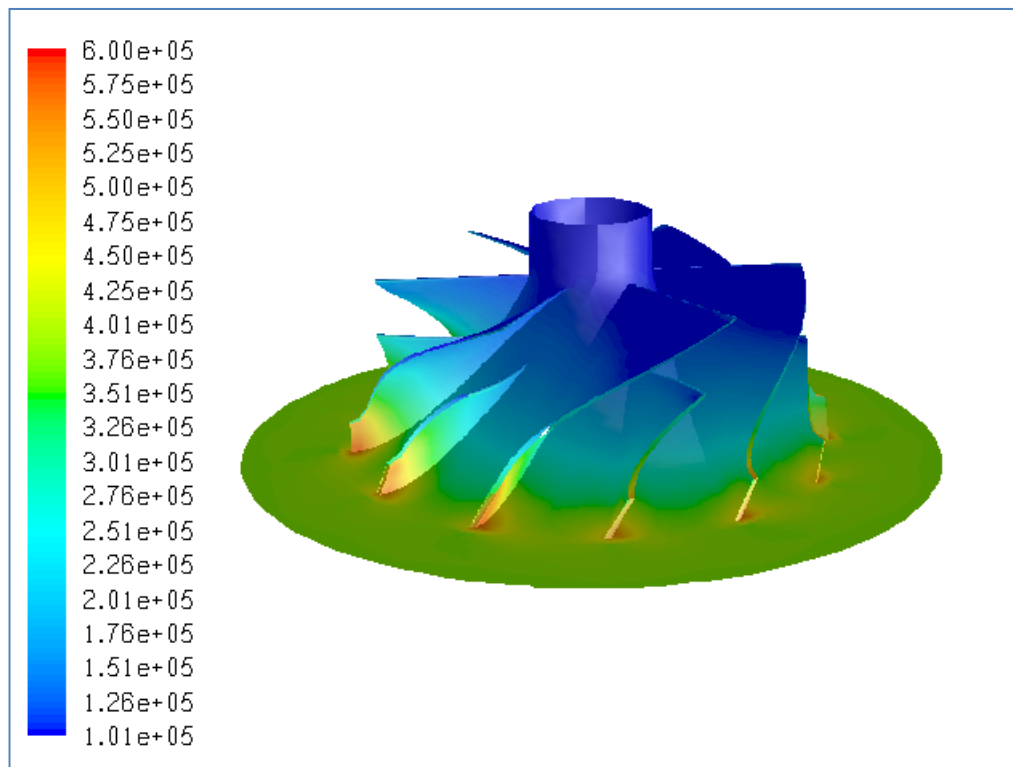


Figure B.71 Total Pressure Distribution (in Pa) for Case #70, PR=3.67

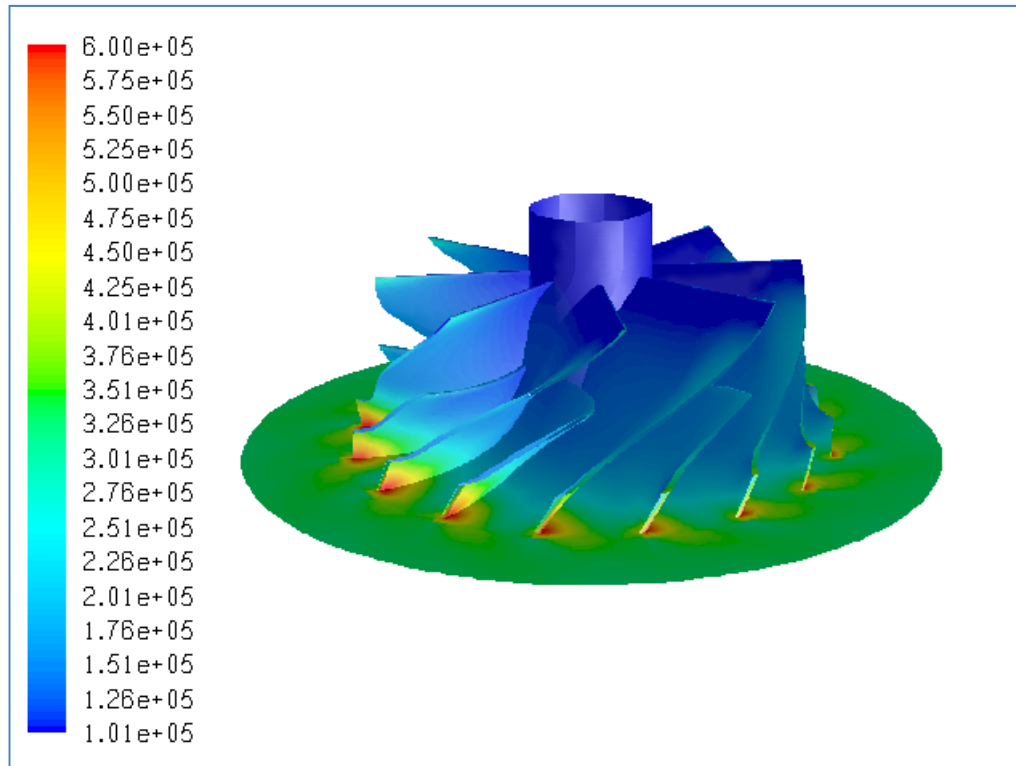


Figure B.72 Total Pressure Distribution (in Pa) for Case #71, PR=3.06

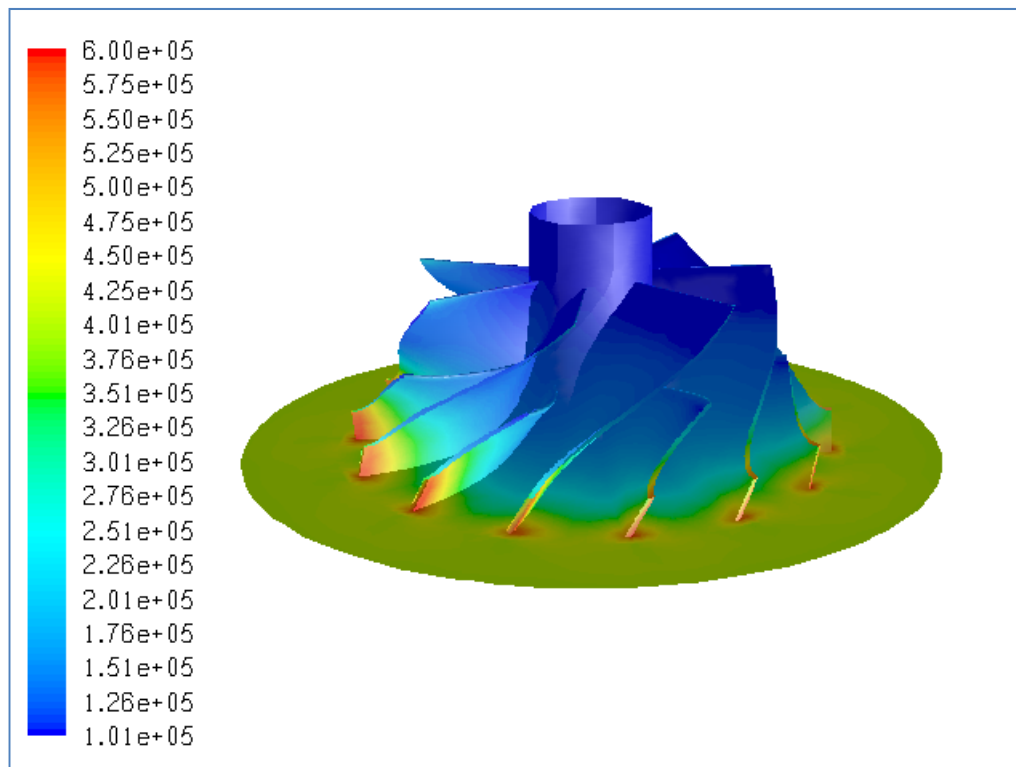


Figure B.73 Total Pressure Distribution (in Pa) for Case #72, PR=3.91

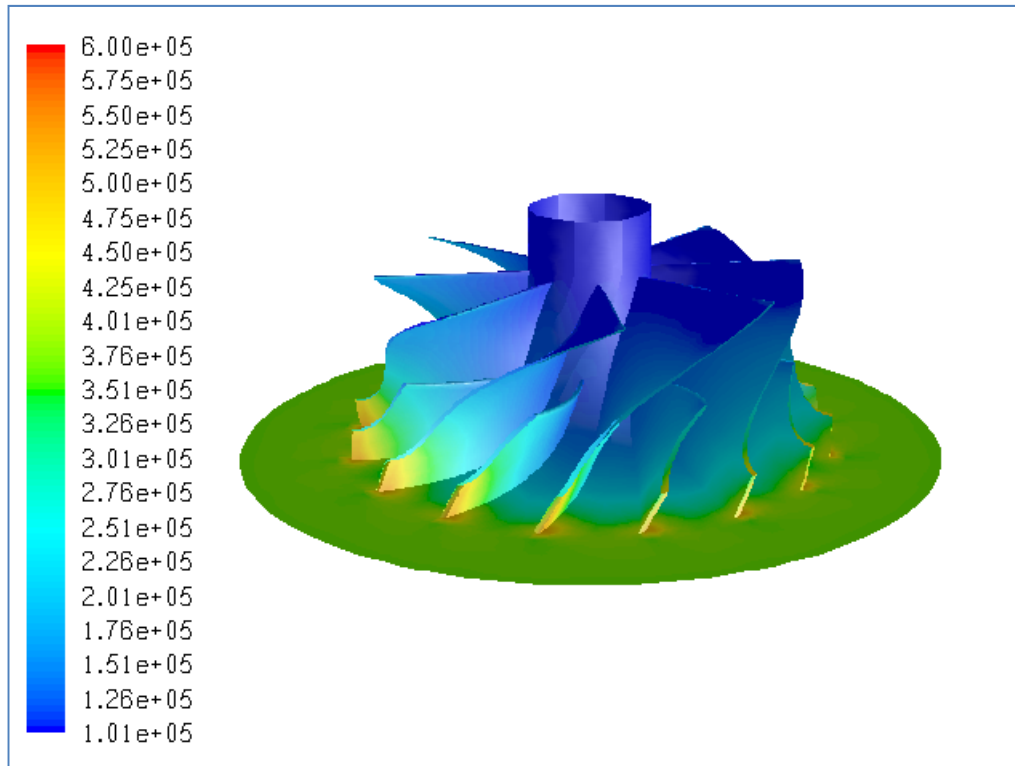


Figure B.74 Total Pressure Distribution (in Pa) for Case #73, PR=3.59

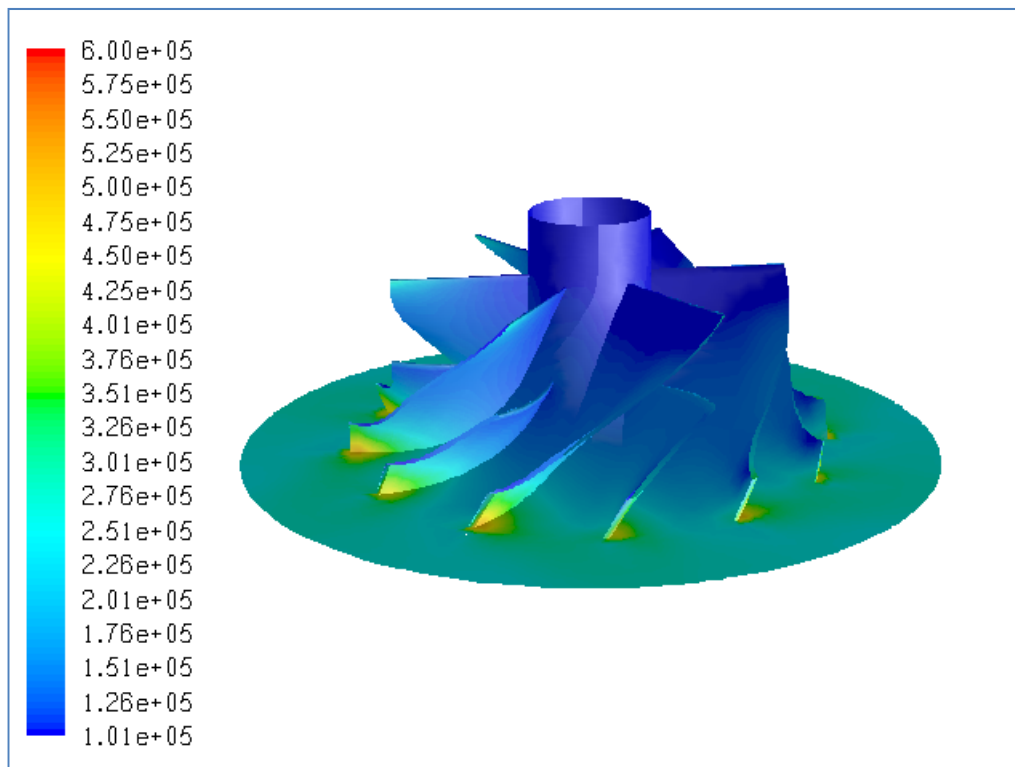


Figure B.75 Total Pressure Distribution (in Pa) for Case #74, PR=2.41

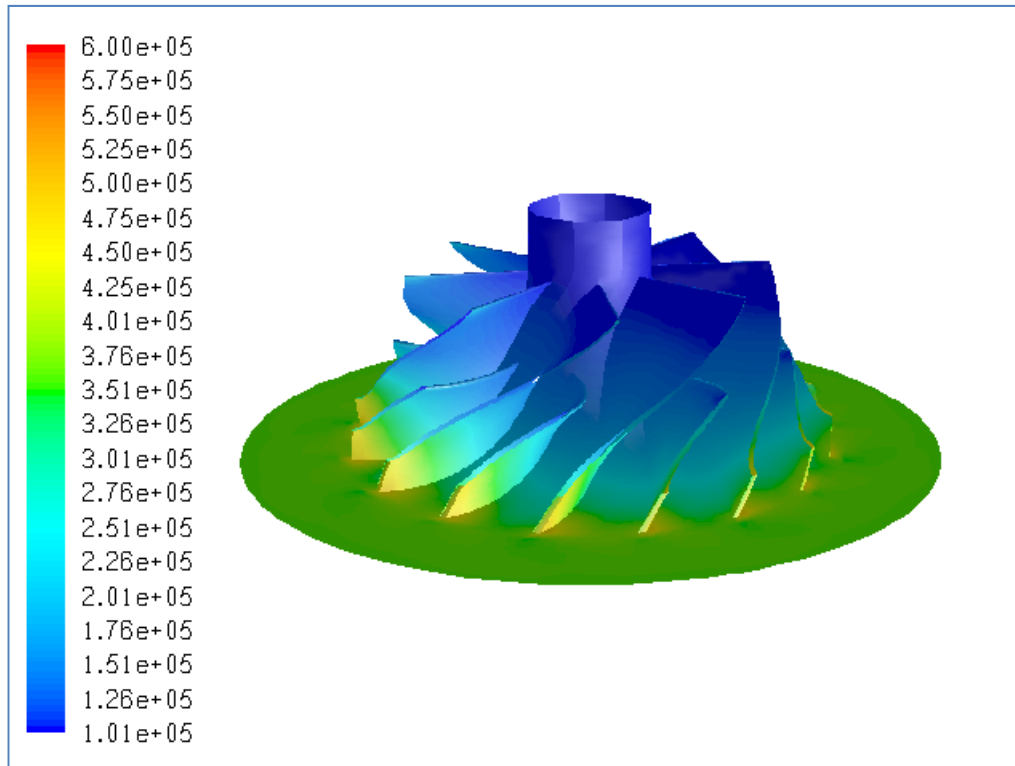


Figure B.76 Total Pressure Distribution (in Pa) for Case #75, PR=3.41

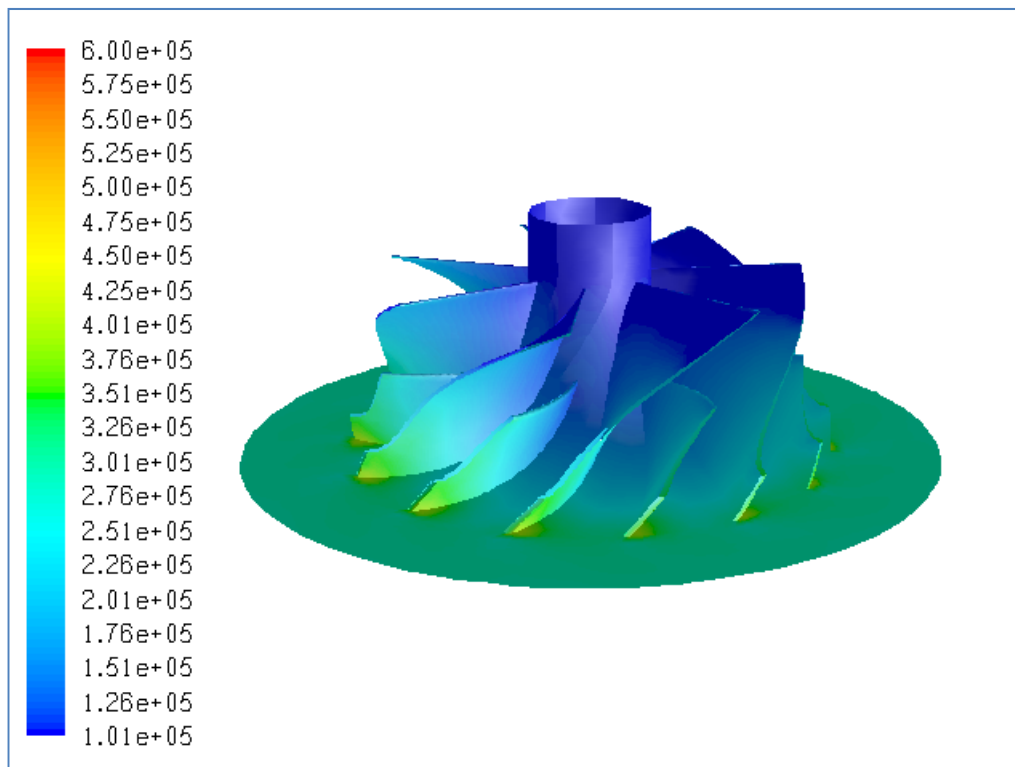


Figure B.77 Total Pressure Distribution (in Pa) for Case #76, PR=2.82

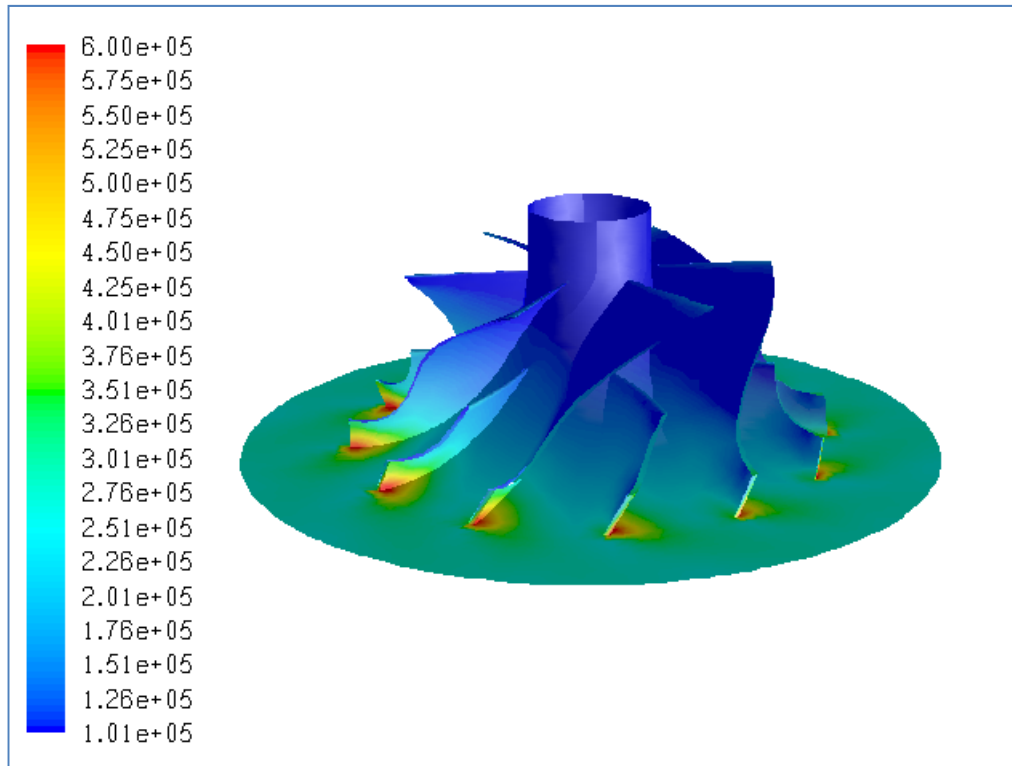


Figure B.78 Total Pressure Distribution (in Pa) for Case #77, PR=2.40

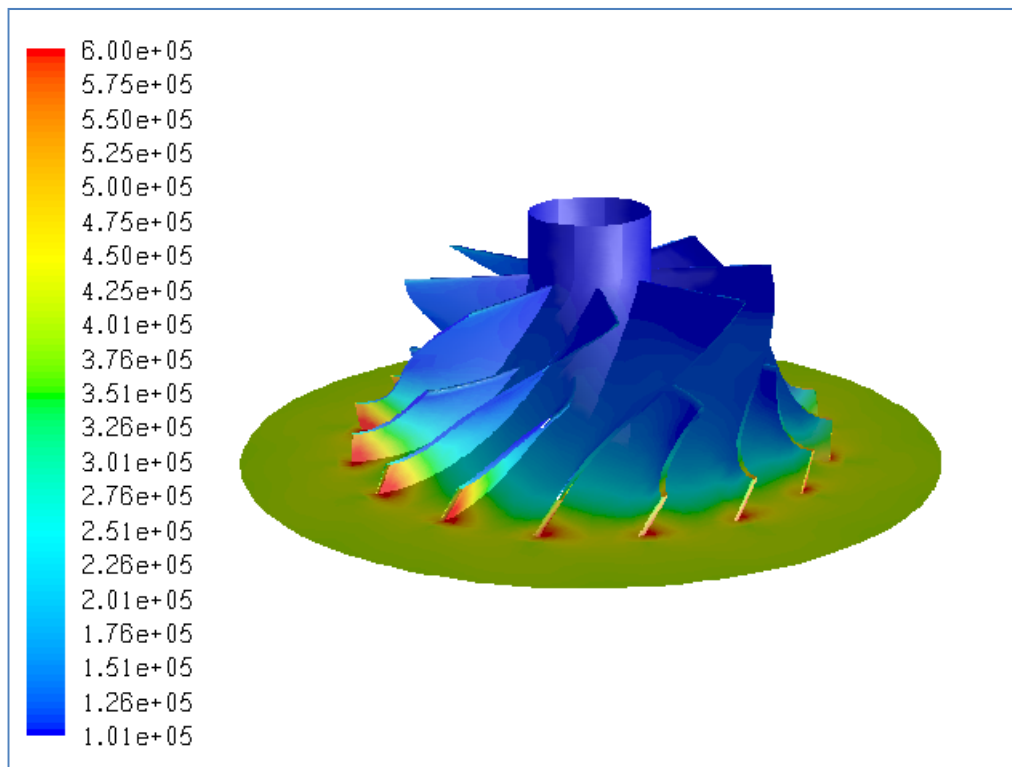


Figure B.79 Total Pressure Distribution (in Pa) for Case #78, PR=3.82

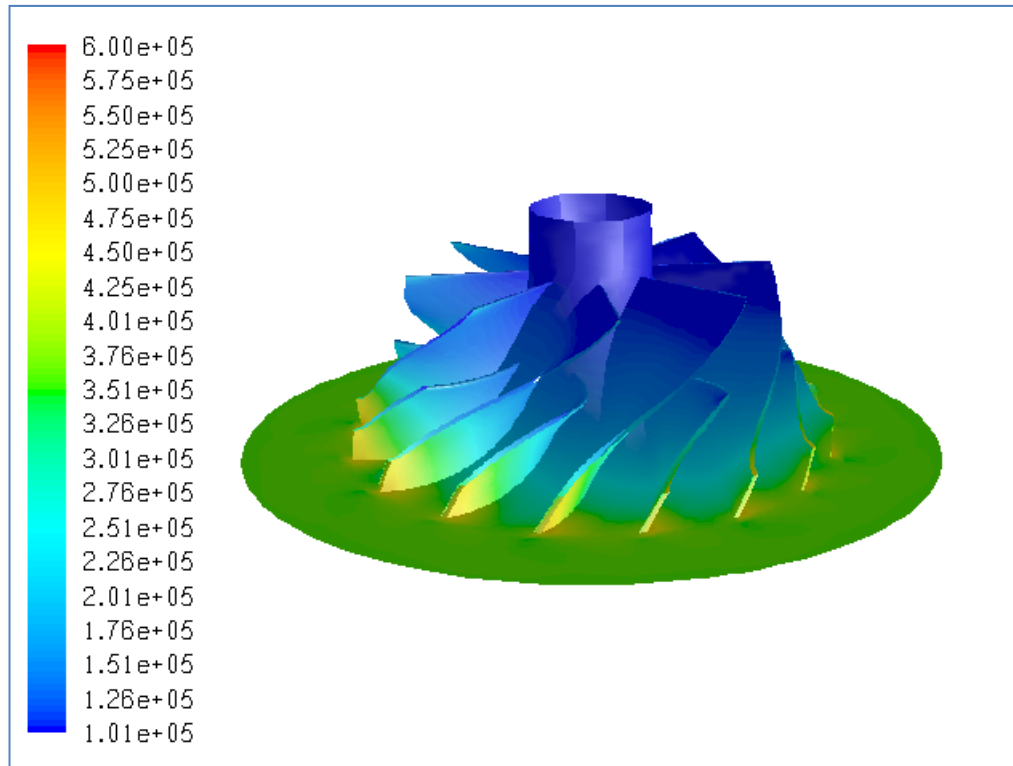


Figure B.80 Total Pressure Distribution (in Pa) for Case #79, PR=3.51

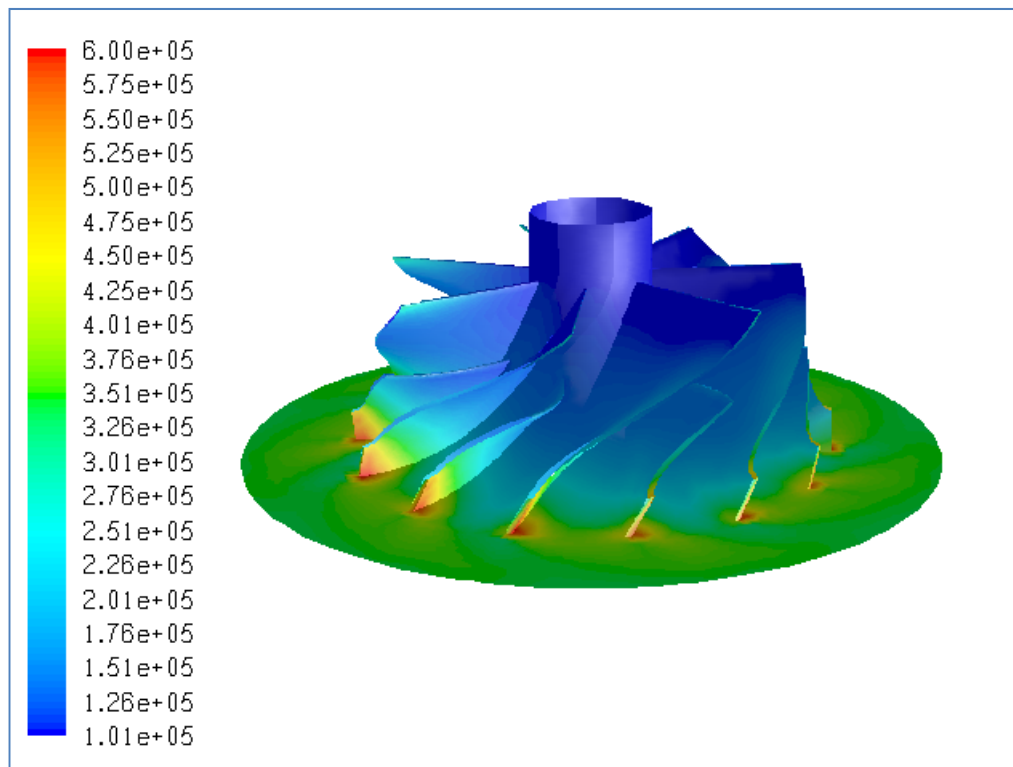


Figure B.81 Total Pressure Distribution (in Pa) for Case #80, PR=3.28

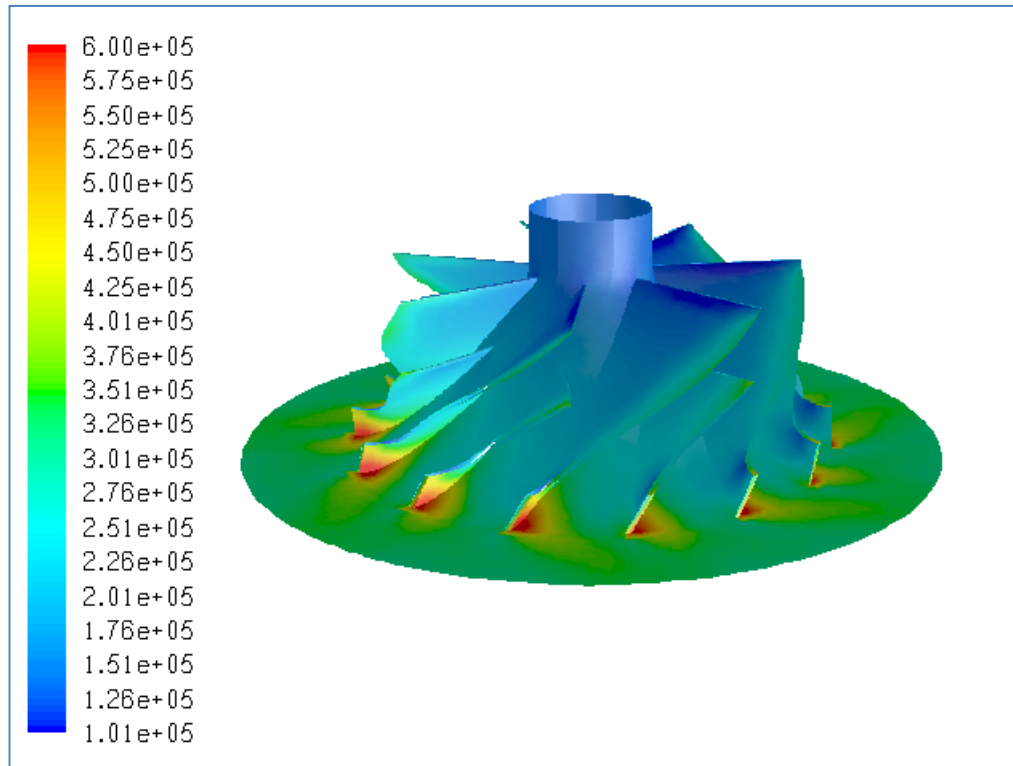


Figure B 82 Total Pressure Distribution (in Pa) for Case #81, Choked

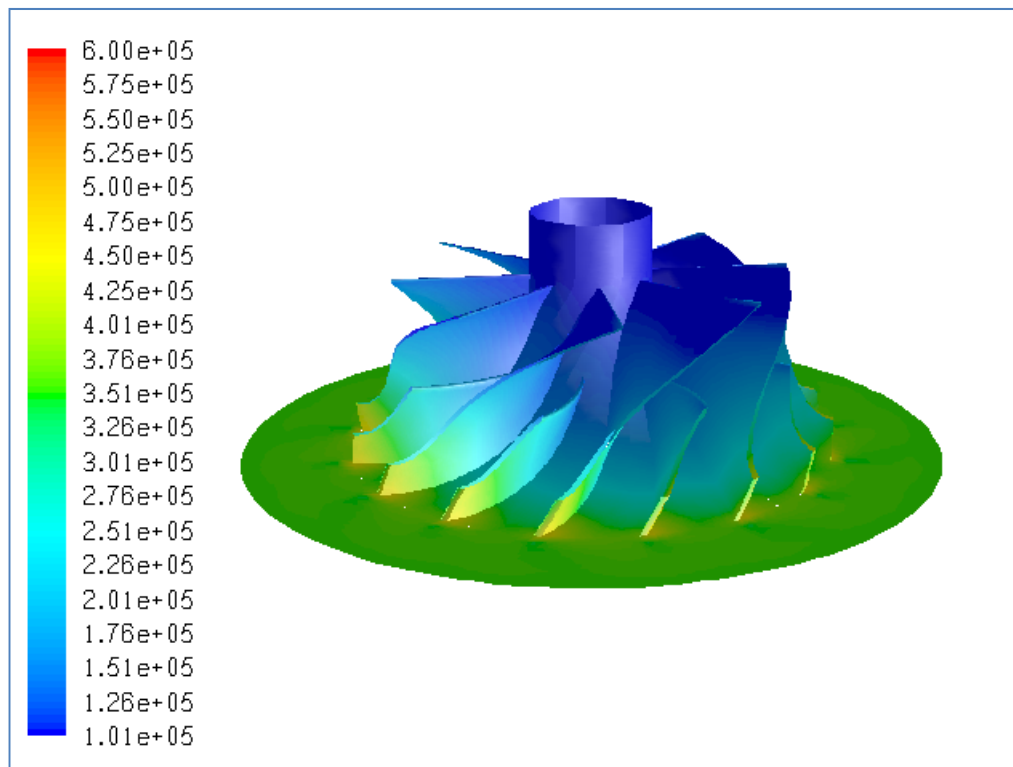


Figure B.83 Total Pressure Distribution (in Pa) for Iteration #1, PR=3.56

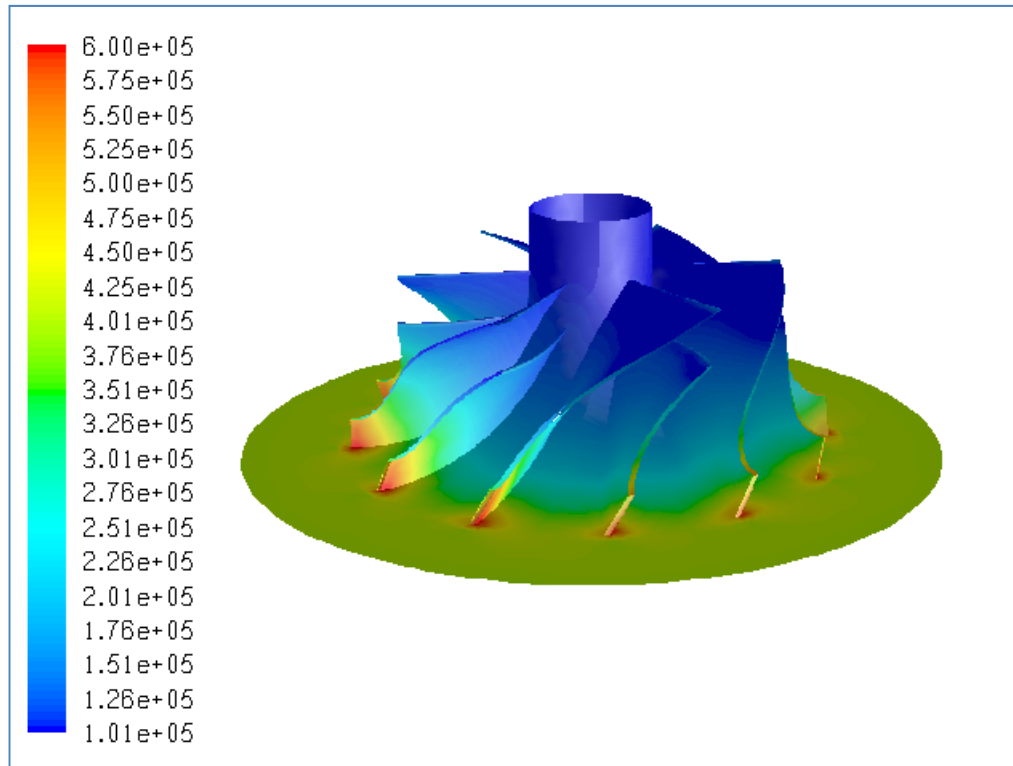


Figure B.84 Total Pressure Distribution (in Pa) for Iteration #2, PR=3.90

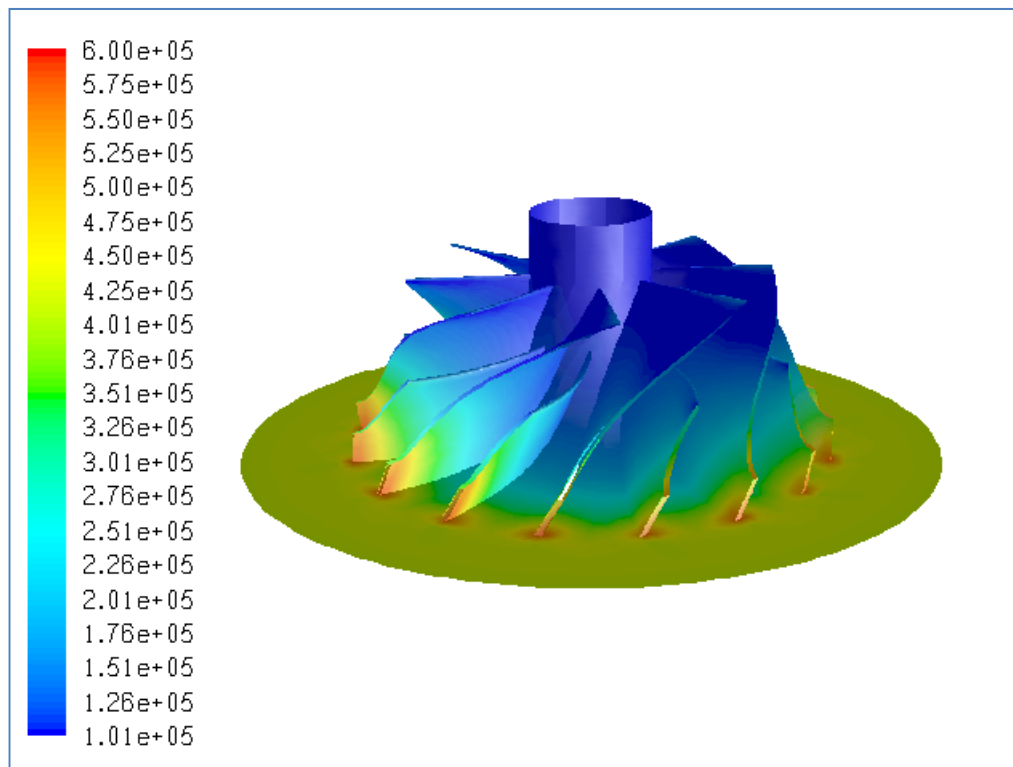


Figure B.85 Total Pressure Distribution (in Pa) for Iteration #3, PR=4.05

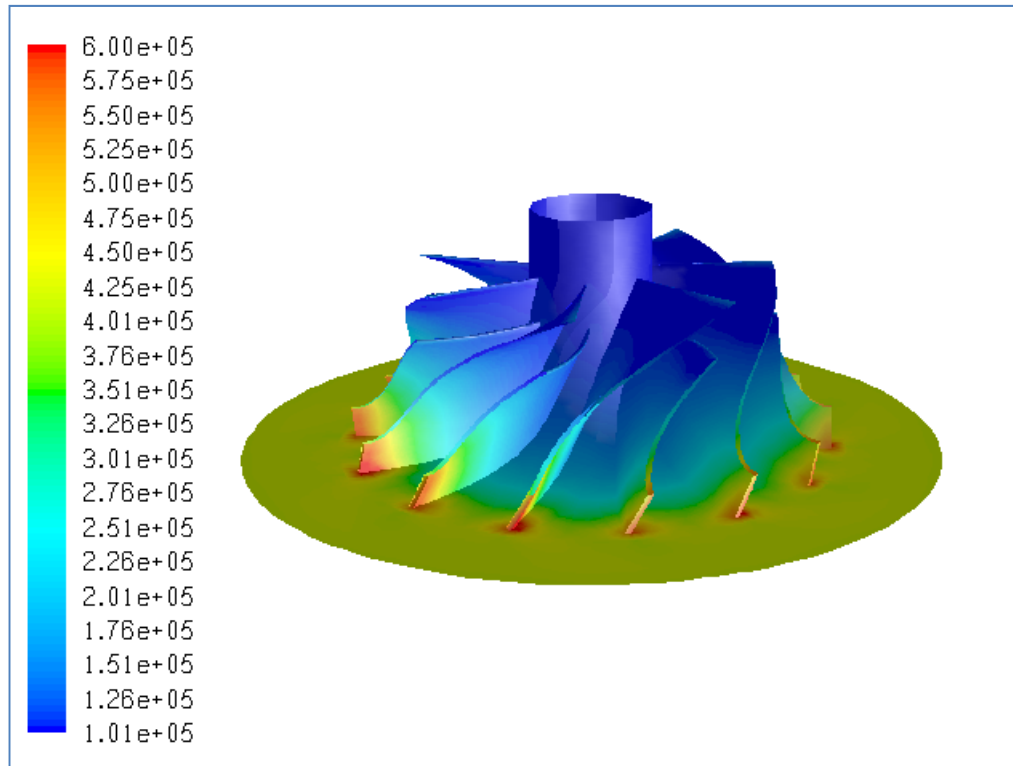


Figure B.86 Total Pressure Distribution (in Pa) for Iteration #4, PR=4.10

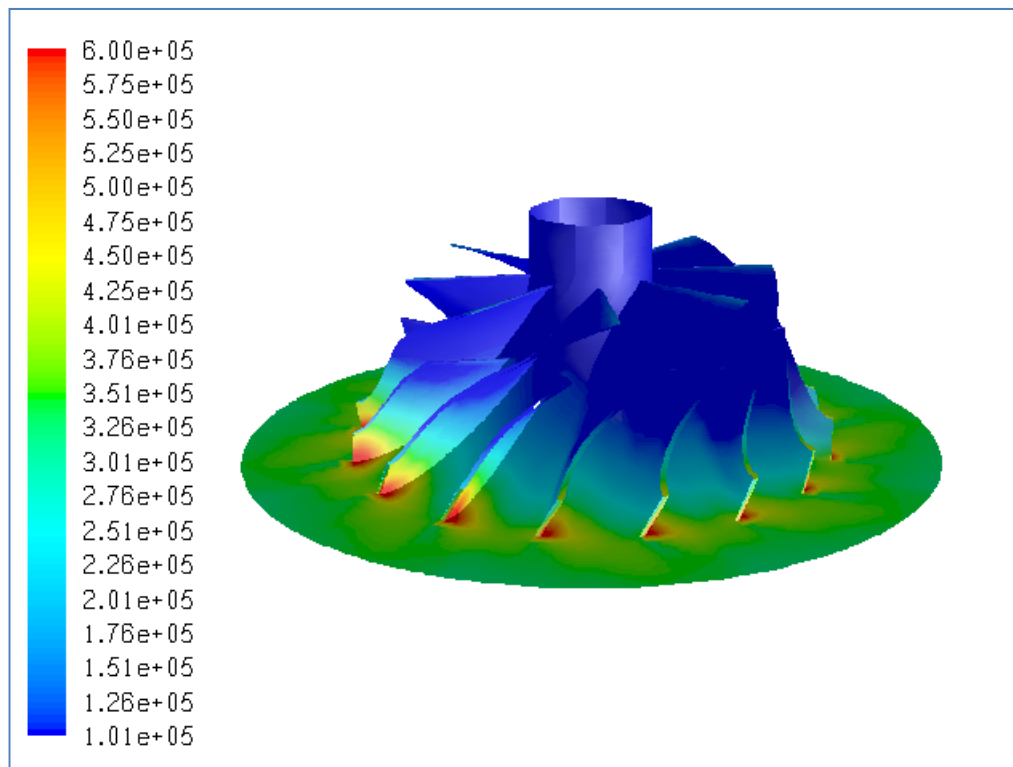


Figure B.87 Total Pressure Distribution (in Pa) for Iteration #5, PR=2.99

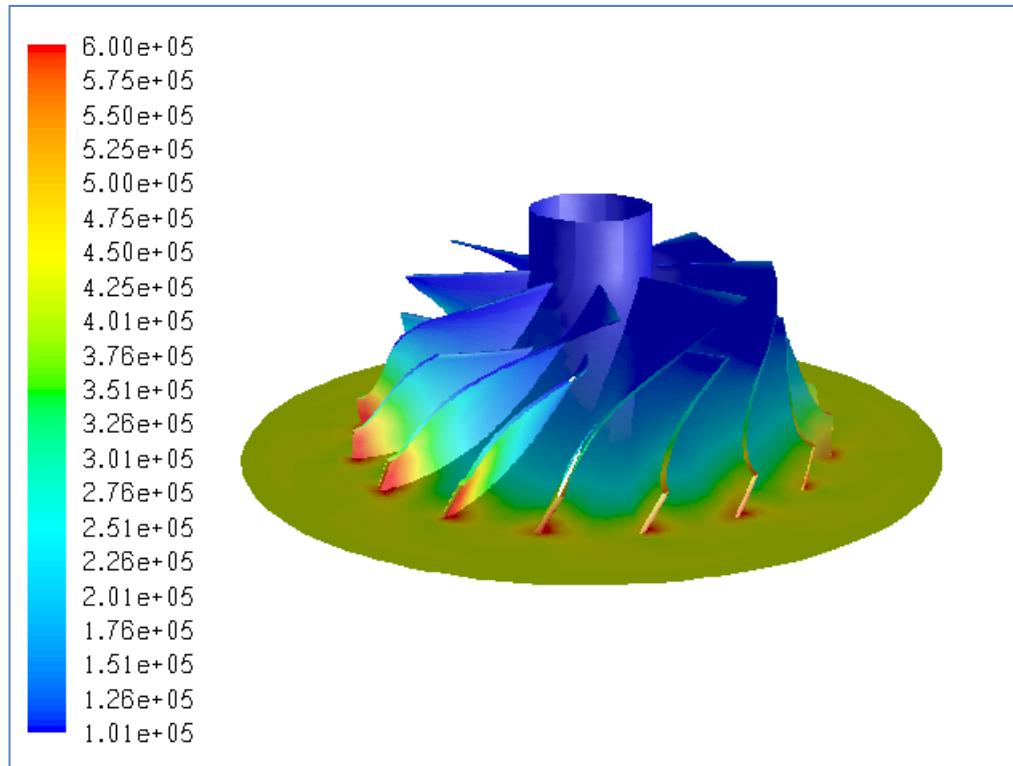


Figure B.88 Total Pressure Distribution (in Pa) for Iteration #6, PR=4.12

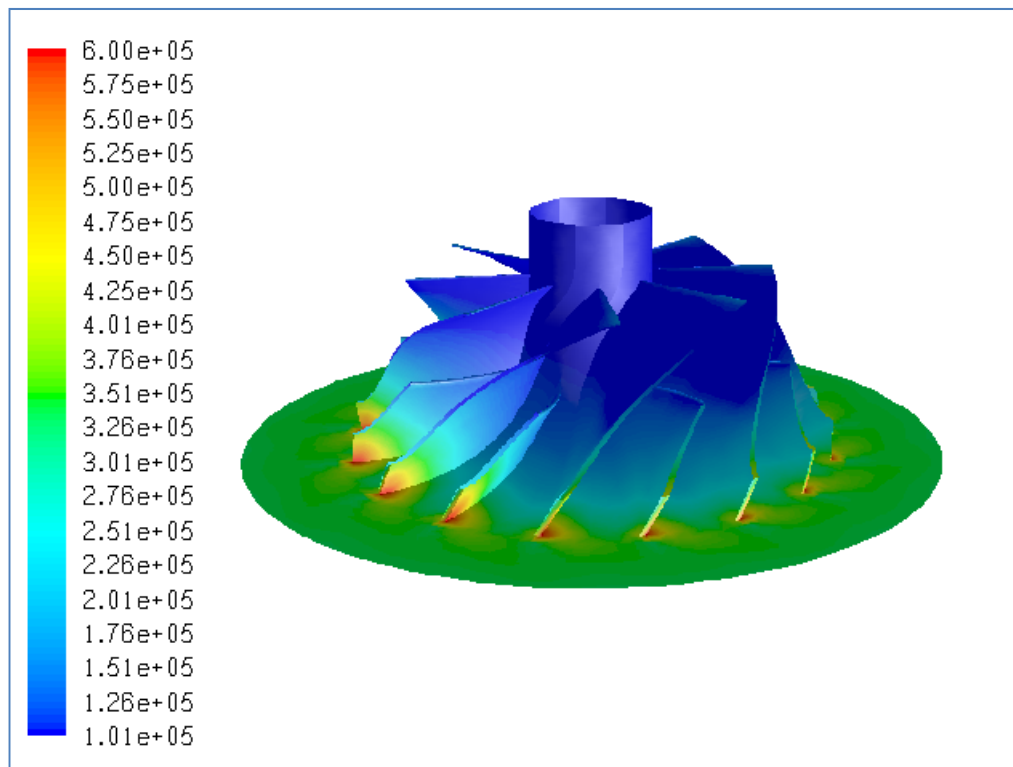


Figure B.89 Total Pressure Distribution (in Pa) for Iteration #7, PR=3.24

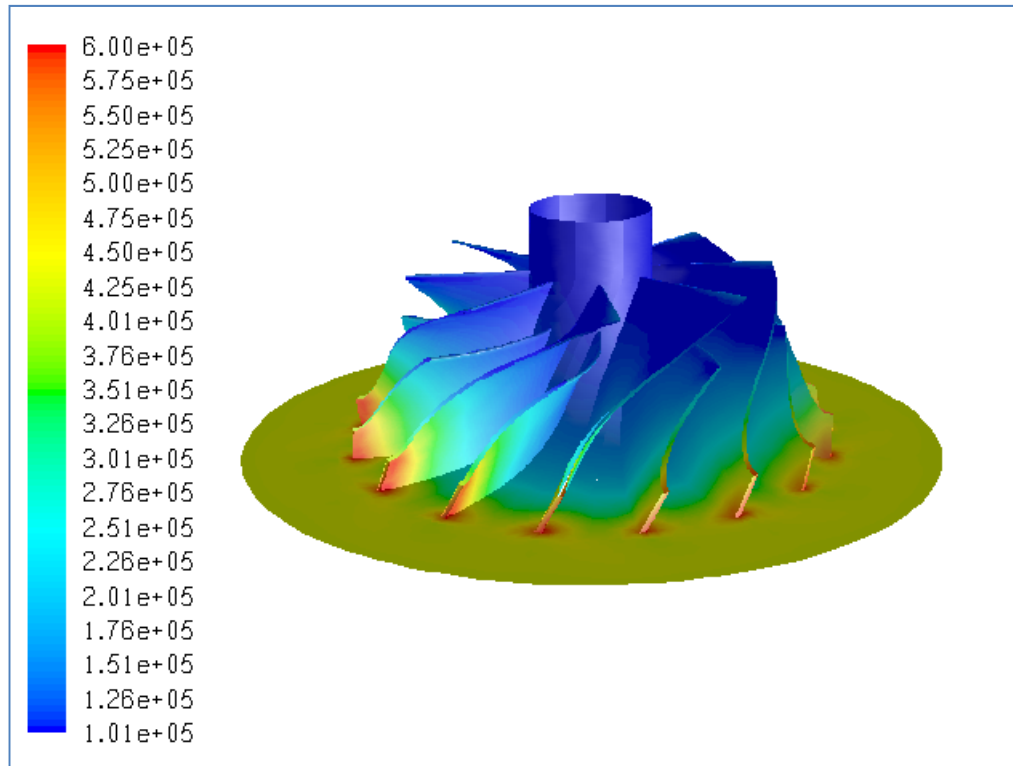


Figure B.90 Total Pressure Distribution (in Pa) for Iteration #8, PR=4.20

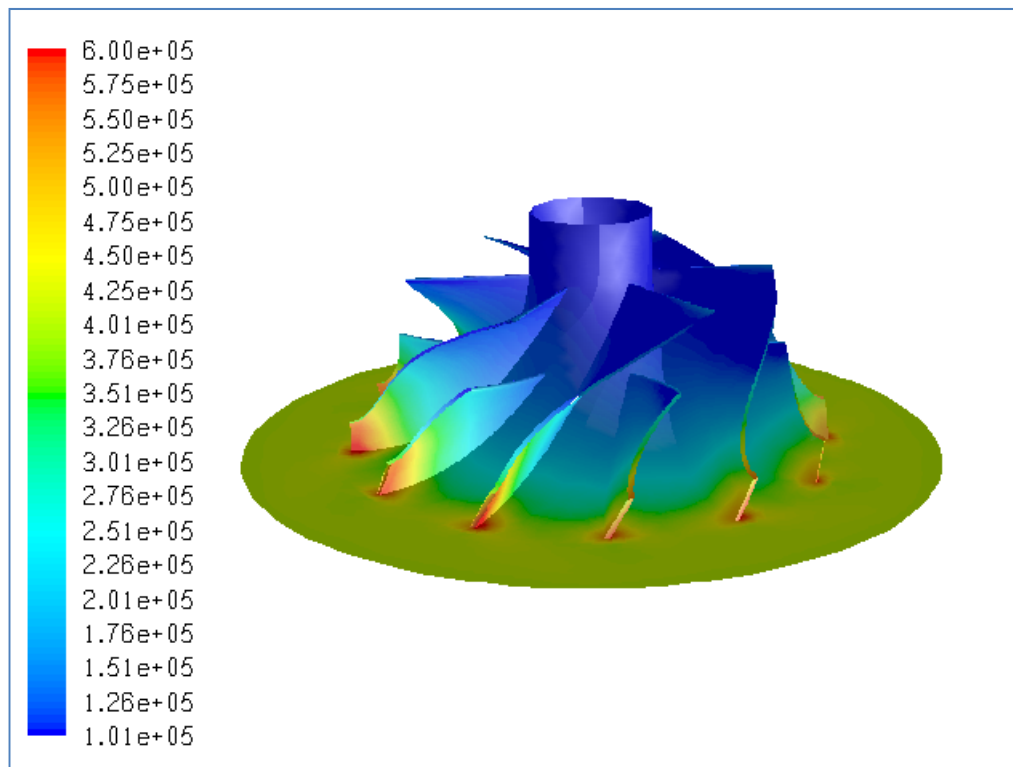


Figure B.91 Total Pressure Distribution (in Pa) for Iteration #9, PR=3.99

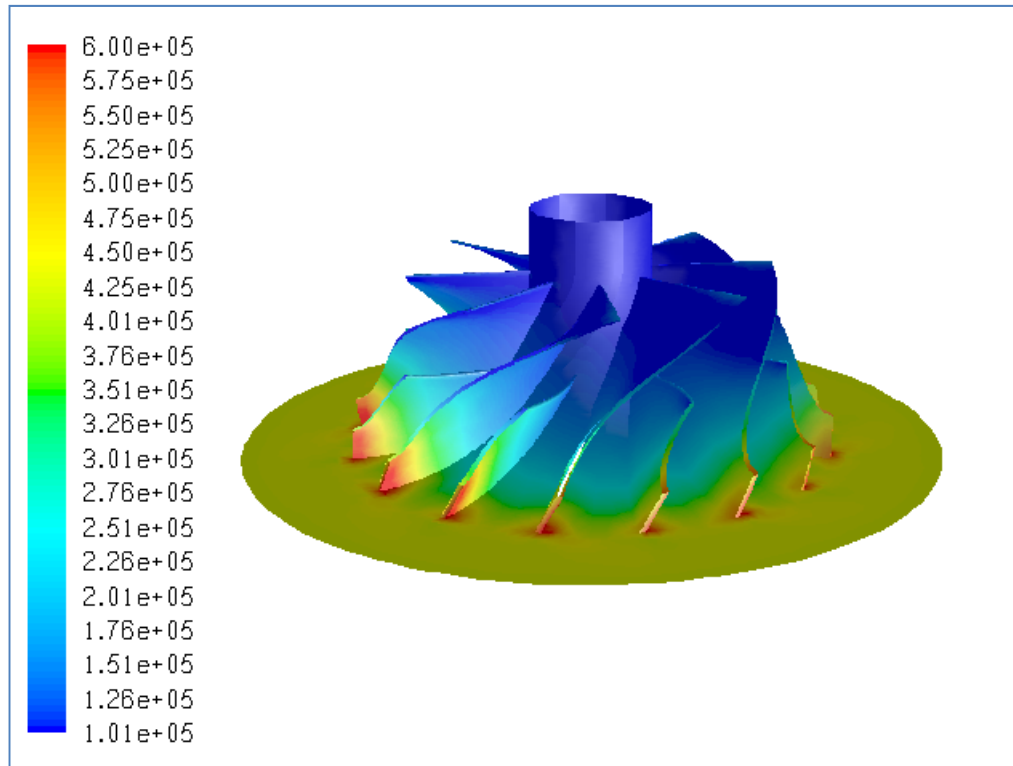


Figure B.92 Total Pressure Distribution (in Pa) for Iteration #10, PR=4.18

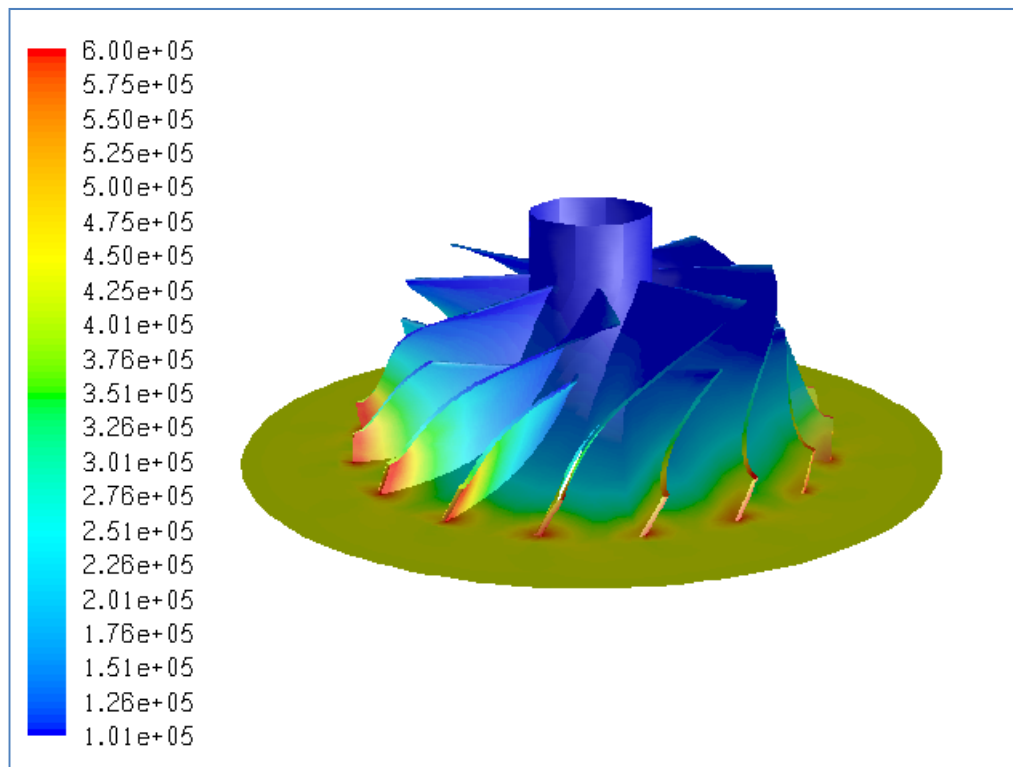


Figure B.93 Total Pressure Distribution (in Pa) for Iteration #11, PR=4.18

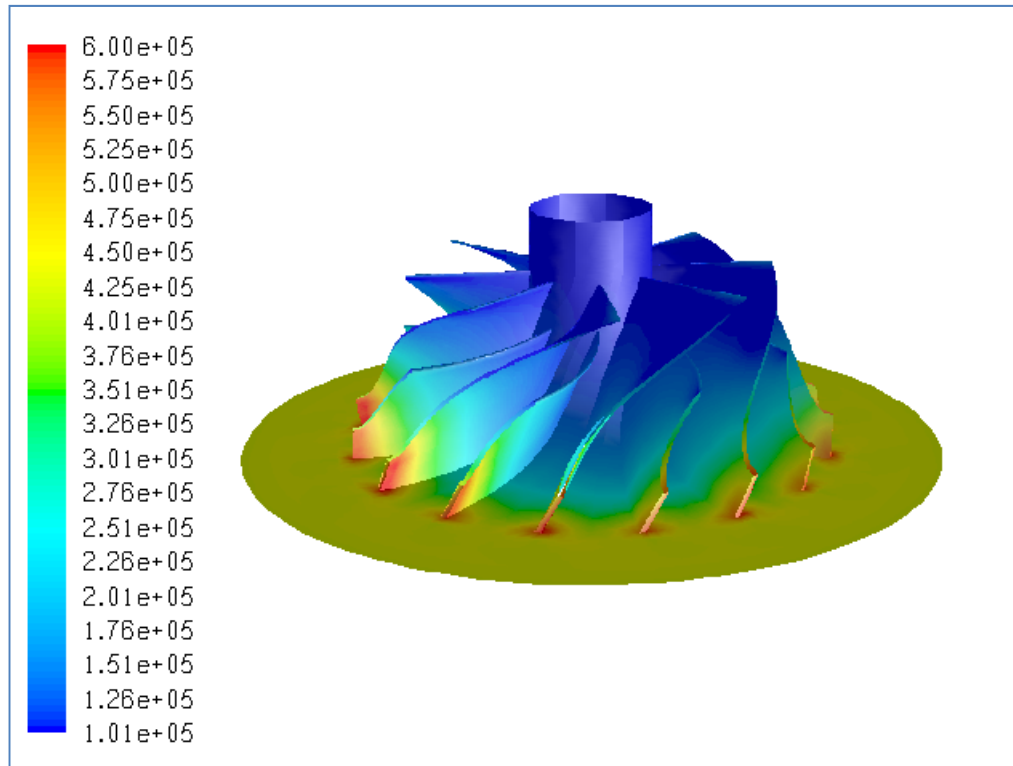


Figure B.94 Total Pressure Distribution (in Pa) for Optimum Case, PR=4.21